A Fluid-Solid Coupled Heat Transfer Methodology as Applied to Rotating Cavities

Tom Hickling

Supervisor: Prof. Li He

Department of Engineering Science

University of Oxford

This dissertation is submitted for the degree of

Doctor of Philosophy

Somerville College October 2022

Abstract

Conjugate heat transfer (CHT), which captures the thermal interaction between the fluid and solid domains, is important for an accurate computational aerothermal analysis when there are temperature dependent fluid domain physics. In the rotating cavities in compressor internal air systems, there is a need to understand the unsteady buoyancy-driven flow and heat transfer so that the disk radial expansion (and hence change in blade tip clearance) throughout the flight cycle can be predicted. Despite the inherently conjugate nature of rotating cavity flows, coupled analyses are rare due to the challenges of using CHT with unsteady methods.

In this thesis, it is shown that it is necessary to use wall-resolved large eddy simulation (LES) to accurately capture the fluid domain flow structures, and to use CHT to capture the interaction of the wall heating conditions and the cavity aerodynamics. The main challenge in LES-CHT is that the timescale in the solid is significantly larger than in the fluid. Many current state-of-the-art methods try to address this by accelerating the solid domain timescale to achieve a temporally converged solution, before switching to a non-accelerated solid solution that is assumed to be correct. However, this is not the case - it is demonstrated in a simplified conduction analysis that these current time domain CHT methods still introduce a long-lasting error in the solid domain temperature.

As a result, a new multiscale framework for LES-CHT has been developed, building on an existing closely coupled methodology. Non-local interactions from coherent low frequency temperature fluctuations are calculated with a time-spectral solid domain solution and turbulent higher frequency fluctuations are accounted for using a wall transfer function approach, reformulated to simplify its application. This is the only framework that can consistently deal with the fluid-solid timescale disparity and capture all timescales of wall temperature fluctuation.

The novel framework is used in first-of-their-kind LES-CHT computations on rotating cavities, evidencing framework efficacy and providing further evidence of the previously observed issues with other LES-CHT methods. An examination of the effect of CHT on the flow structures within the rotating cavity found that thermally induced near-disk vortical instabilities are seen to only form when there is strong local heating. This effect has not been previously observed and illustrates the value of the multiscale framework for deriving new insights into heat transfer in gas turbines.

Acknowledgements

First, I'd like to thank Prof. Li He for being a fantastic supervisor and mentor. Thank you for the initial vote for confidence in securing funding for my DPhil, and for keeping me as on track as possible throughout. Our research discussions were always enjoyable and usually the highlight of my work week, and I'm sure that they will continue to shape the way I think about engineering, fluid dynamics, and research into the future.

Thanks are due to Prof. Budimir Rosic and Dr Nick Atkins for the valuable feedback during my viva, and also to Dr John Coull for support through transfer and confirmation of status and for organising the lab seminars. I'm extremely grateful to Craig Parsons - without all the support with clusters, workstations, and software licensing, a DPhil on CFD would have been impossible to do. I would also like to acknowledge the funding from the EPSRC and use of the University of Oxford Advanced Research Computing facility (http://dx.doi.org/10.5281/zenodo.22558).

There are lots of people outside the lab who have helped me during these last four years. Thanks to my friends from Somerville for sharing the DPhil experience with me and keeping me sane. Maddie - meeting you was the best thing that happened during my DPhil and I don't think I could have got it done without your constant love and support, thank you. To my sister Bethany, thank you for keeping me grounded and laughing – I can see the daft cactus that sings the wrong song as I write this...

Finally, and most importantly, to Mum and Dad - thank you for making me feel that doing a DPhil was even possible in the first place.

“Airplanes are not tools for war. They are not for making money. Airplanes are beautiful dreams. Engineers turn dreams into reality.” - Hayao Miyazaki

Table of Contents

List of Figures

List of Tables

Nomenclature

Roman Symbols

a	Disk inner radius [m]
A_n, B_n	n^{th} cosine and sine temperature harmonic coefficients [K]
A_p	Residue of the p^{th} pole
b	Shroud radius [m]
Bi_m	Mesh Biot number [1]
c	Specific heat capacity [J/kgK]
$\widehat{C}_{Tq}$	T-q transfer function
d_H	Hydraulic diameter [m]
f	Frequency [Hz]
f_0	Base/dominant frequency [Hz]
Gr	Grashof number = $(1 - a/b)^3 Re_\phi^2 \beta \Delta T_{max}$ [1]
h	Interface heat transfer coefficient [W/m^{2}K]
k	Thermal conductivity [W/mK]
L	Solid domain characteristic length scale [m]
M	Time step number [1]
N_{RA}	Number of radial arms [1]
Nu	Nusselt number = $qr/k_{in}\Delta T_w$ [1]
P	Number of poles
q	Heat flux [W/m^2]

r, ϕ, z	Cylindrical coordinates [m, rad, m]
r_s	Shaft radius [m]
Re_ϕ	Rotational Reynolds number = $\rho_{in}\Omega b^2/\mu_{in}$ [1]
Re_z	Axial Reynolds number = $\rho_{in}V_z d_H/\mu_{in}$ [1]
Ro	Rossby number = $V_z/\Omega a$ [1]
s	Cavity width [m]
$\mathcal{S}$	Laplace variable
T	Temperature [K]
t	Time [s]
u, v, w	Relative velocity components in Cartesian coordinates [m/s]
V_r, V_ϕ, V_z	Relative velocity components in cylindrical coordinates [m/s]

Greek Symbols

α	Thermal diffusivity [m^2/s]
$\beta\Delta T_{max}$	Buoyancy parameter = $(T_{max} - T_{in})/T_{in}$ [1]
β	Thermal penetration depth resolution parameter [1]
Δp	Pressure difference [Pa]
ΔT	Temperature difference [K]
Δt	Time step size [s]
Δx	Mesh spacing [m]
δ^*	Location of peak TKE
δ_p	Thermal penetration depth [m]
δ_{Ek}	Ekman layer thickness [m]
λ_p	p^{th} pole
μ	Dynamic viscosity [Pa s]
μ_t	Turbulent dynamic viscosity [Pa s]
Ω	Rotational speed [rad/s]

ω_0	Base angular frequency [rad/s]
ω_ϕ	Circumferential vorticity [1/s]
ψ	Generic variable
ρ	Density [kg/m^3]
τ	Pseudo time [s]
τ_ϕ	Circumferential shear stress [Pa]
τ_r	Radial shear stress [Pa]

Subscripts / Superscripts

∞	Global reference value
core	Core flow
f	Fluid
in	Inlet
max	Maximum value
s	Solid
sh	Shroud
w	Wall

Other Symbols

$\widetilde{\psi}$	Time-average of ψ
$\widehat{\psi}$	Complex valued Fourier harmonic of ψ
$\overline{\psi}$	Laplace transform of ψ
ψ^*	Normalised value of ψ
ψ'	Fluctuations of ψ, sometimes low frequency coherent fluctuations of ψ
ψ''	High frequency turbulent fluctuations of ψ

Acronyms / Abbreviations

ADE	Auxiliary differential equation
CFD	Computational fluid dynamics

CFL	Courant-Friedrichs-Lewy number
CHT	Conjugate heat transfer
DES	Detached eddy simulation
DFT	Discrete Fourier Transform
HP	High pressure
HTC	Heat transfer coefficient [W/m^2K]
IFT	Inverse Fourier Transform
LES	Large eddy simulation
PSD	Power spectral density
RANS	Reynolds averaged Navier-Stokes
RMS	Root mean squared
SGS	Sub-grid scale
TF	Wall transfer function
TKE	Turbulent kinetic energy
TVR	Turbulent viscosity ratio μ_t/μ
URANS	Unsteady Reynolds averaged Navier-Stokes
WALE	Wall-adapting local eddy viscosity

Chapter 1

Introduction

1.1 Background

1.1.1 Why Rotating Cavity Flows?

The aerospace industry contributes ∼3.5% to the additional heating of the atmosphere caused by human activities (Lee et al., 2021). To reduce its environmental impact in the near to medium term before alternative fuels come online, new architectures such as ultra-high bypass ratio engines, geared turbofans, and embedded distributed propulsion are coming to the fore. In these new architectures, the engine core is likely to be smaller in size compared to contemporary engines. Smaller core sizes generally lead to increased (relative) blade tip clearances (shown in Fig. 1.1), particularly in the high pressure (HP) compressor where the blade heights are smaller. Increasing the blade tip clearance causes an increase in compressor losses, and a decrease in its stability (Atkins, 2013).

The dominant factor governing the blade tip clearance is usually the axisymmetric

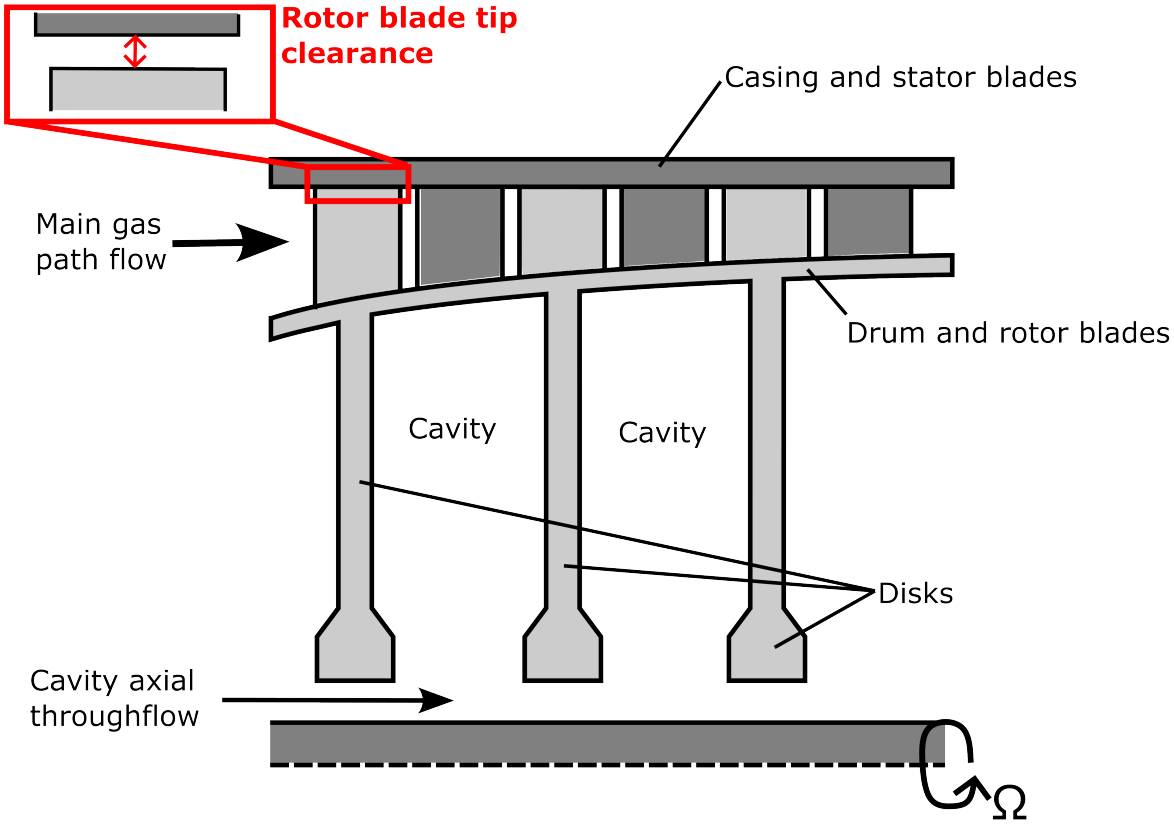

Figure 1.1. Schematic of an HP compressor showing the location of the rotating cavities and disks, and the blade tip clearance.

radial growth of the compressor drum and casing caused by thermal and centripetal effects. The compressor casing is subject to higher heat transfer coefficients and has a lower thermal mass than the compressor drum, the radial growth of which is governed in part by the thermal expansion of the compressor disks that bound the rotating cavities. As a result, the compressor casing responds much more quickly to changes in main gas path flow temperature. This is particularly a concern just after an engine acceleration (which results in a transient maximum clearance) or just after an engine deceleration (which results in a minimum clearance). Both of these scenarios are important: just after take-off the former is the moment of minimum surge margin, and just after an aborted landing (when the engine is subject to a full hot re-slam and undergoes almost instantaneous centripetal growth) the latter set the cold build clearance (Atkins, 2013).

It is clear that there is a need to understand the heat transfer within the cavity to allow for better predictions of the radial expansion of the disks, and ultimately tighter blade tip clearances. This will lead to more efficient, more stable compressors in novel engine architectures, reducing fuel burn, fuel volume/weight carry requirements, and CO_2 emissions.

The cavity disks are often cooled by the axial throughflow of compressor bleed air used for cooling the turbine downstream. The cooling influence of the throughflow leads to the cavity disks radially increasing in temperature. Through interactions with the Coriolis force and centrifugal buoyancy forces, this leads to a complex, inherently unsteady flow structure that has historically proved difficult to compute or measure (Owen and Long, 2015). The flow in the cavity is driven by the disk temperature distribution, which is in turn influenced heavily by heat transfer to the flow within the cavity - this makes it an inherently conjugate problem where the thermal interactions

between the cooling gas in the cavity and the solid disks need to be captured for an accurate prediction. Despite the unsteady conjugate nature of the flow, computations that take this interaction into account have been rare - as far as the author is aware the only example prior to this thesis was Tian and Zhu (2012).

1.1.2 Computational Fluid Dynamics for Aerothermal Analysis

The rapid improvement in computational fluid dynamics (CFD) capabilities over recent decades has enabled the amount of experimental testing required to design new gas turbines to be significantly reduced. It has also lead to physical insights that would otherwise have been impossible to come by (Slotnick et al., 2014) - as noted by Denton (1993), a good physical understanding of the flow mechanisms within turbomachines may be more valuable than accurate empirically-based predictions. Two areas of CFD that are key to this thesis are discussed below.

Turbulence modelling

One of the main causes of uncertainty in any CFD simulation (but especially aerothermal CFD) is the modelling of effects turbulence, particularly in unsteady flows. The unsteady Reynolds averaged Navier-Stokes (URANS) equations are a simple extension on the ubiquitous eddy viscosity based steady RANS models. However, they also suffer from all the same issues as RANS models around being inherently empirical, not accounting for Reynolds stress anisotropy, and failing to account for the effects of buoyancy forces, streamline curvature, and rotation (Tucker, 2016). Although palliatives for these are available, these are empirical, and can have little value beyond the flow that they were calibrated for.

Difficulties arise in URANS due to the method's unsteady nature - it requires a spectral gap between the modelled turbulence and large-scale resolved unsteadiness

(Palkin et al., 2016). This rarely occurs, causing URANS to double count unsteady turbulent structures in flow regimes such as wake flows and vortex shedding (Tucker, 2013; Yao and He, 2020). A further issue is the advection of locally generated eddy viscosity to regions where it is unphysical. This effect has been noted in a HP turbine cascade by Yao and He (2020), where eddy viscosity generated upstream was advected to the trailing edge where it interfered with unsteady vortex shedding.

Large eddy simulation (LES) is the highest modelling fidelity considered in this thesis - it resolves the majority of the turbulent kinetic energy (TKE) - 80% according to Pope (2004) - and the effects of the sub-grid scales are either modelled using an eddy viscosity (e.g. the WALE model of Nicoud and Ducros (1999)), or even with dissipation from the numerical scheme (Margolin and Rider, 2002). It should be noted that this 80% criteria makes a poor *a-posteriori* resolution check as under-resolved LES tends to over-predict the resolved TKE (Davidson, 2009). LES approaches require an extremely fine mesh to accurately resolve the near-wall flow in a turbulent boundary layer - as in RANS models, the wall-normal normalised spacing must be around one, but the wall parallel spacings must be less than 50 and 15 units in the streamwise and cross-stream directions.

The cost of resolving the near-wall flow in LES is off-putting, and makes higher Reynolds numbers hard to reach. As a rough estimate, the cost of a LES simulation is two orders of magnitude large than a RANS simulation on the same configuration (Tyacke and Tucker, 2015). This can be expected to be even worse for higher Reynolds numbers (e.g. engine relevant conditions, full engine simulations, or engine-air frame interaction studies) as the mesh requirement for a fully resolved LES scales with $\mathcal{O}(Re^2)$, mostly due to the cost of resolving the near-wall region (Choi and Moin, 2012). Going from a laboratory configuration to a engine relevant one (at a

Reynolds number that is an order of magnitude larger) will result in a two orders of magnitude increase in computational cost, which can often be prohibitive - in industry there is a strong drive to use the lowest fidelity methods possible to avoid this and keep design cycle times low. These require extensive assessment and calibration - here, highly fidelity numerical simulations can be one hundred times less costly than experimental studies, and yield data that is significantly more useful (Tyacke et al., 2019).

To address this, URANS/LES approaches have been suggested. These approaches model the near-wall turbulence with URANS, but resolve eddies that are detached from the wall with LES. Removing the need to simulate the near-wall eddies reduces the mesh size scaling to $\mathcal{O}(Re)$ (Choi and Moin, 2012), making higher Reynolds number simulations much more practical. There is a contradiction in using these approaches for aerothermal CFD - the most important region for heat transfer is the near-wall region, yet URANS/LES hybrids use the lowest modelling fidelity here. The near-wall region is high gradient, and thus highly sensitive, so the switch of modelling fidelity creates additional uncertainty that may significantly affect the wall heat transfer (He and Yi, 2017). It is therefore reasonable to expect hybrid URANS/LES approaches to suffer from all the same issues in heat transfer as URANS approaches - particularly double accounting, as the URANS region of the flow is subject to high frequency forcing from the outer LES. Even in isothermal flows, URANS/LES approaches need to be used with care due to the well known issues of modelled stress depletion, grid induced separation, and the "grey area" where the simulation is neither URANS or LES (Tyacke and Tucker, 2015).

From this brief discussion, a hierarchy of turbulence modelling fidelity can be proposed, as by Tyacke et al. (2019). For unsteady approaches, from low to high

fidelity (and low to high computational cost) the hierarchy is:

1. URANS
2. URANS/LES hybrids
3. LES

Conjugate heat transfer

Conjugate heat transfer (CHT) refers to a calculation or CFD simulation where the fluid and solid domains are allowed to interact thermally. The boundary between the fluid and solid domains must satisfy both the local conservation of heat flux and temperature continuity on the interface.

The computational expense of conjugate computations means that, to find the wall temperature in rapid design iterations, designers often rely on the heat transfer coefficient (HTC) as an invariant to extrapolate from experimental/computational results at one flow condition to another (Moffat, 1998).

The first effort in this direction was Newton's law of cooling, which states that an object cools at a rate proportional to its temperature difference to the surroundings, with the constant of proportionality being the conventional HTC, defined as

$$\mathrm{HTC}_c = \frac{q}{T_w - T_\infty}, \tag{1.1}$$

where q is the wall heat flux, T_w is the wall temperature, T_∞ is the temperature of the surroundings. This definition was also used in internal flows, where the global reference temperature T_∞ is the bulk fluid mean temperature (Moffat, 1998). With increased interest in boundary layer flows in the gas turbine community in the 1940s, it

became clear that point-by-point values of HTC are needed (Moffat, 1998) - even in simple analytical conjugate solutions of laminar flows, it can be shown that the HTC varies spatially (Dorfman, 2017). In addition, the conventional HTC defined in this way is extremely sensitive to spatial variations in wall temperature - step increases/decreases can force it to $\pm\infty$ (Moffat, 1998).

Using the freestream temperature as a global reference temperature is not a good choice in terms of finding a robust invariant descriptor of heat transfer. A better reference temperature is the adiabatic wall temperature (T_{aw}) - this includes effects from temperature recovery in higher Mach number flows and is better conditioned when there are changes in surface temperature (Moffat, 1998). This leads to an alternative definition, the adiabatic HTC:

$$\mathrm{HTC}_a = \left.\frac{\partial q}{\partial T_w}\right|_{T_{aw}} \approx \frac{q}{T_w - T_{aw}}. \tag{1.2}$$

In this definition, the HTC is defined as the rate of change of wall heat flux with wall temperature, evaluated at the adiabatic wall temperature.

To evaluate the conventional HTC is quite simple - only one computational or experimental data point is needed as the global reference temperature is known *a-priori*. Evaluating the adiabatic HTC is more involved due to the need to find T_{aw} – it requires at least 2 data points in order to draw a straight line - this line intersects with $q = 0$ at $T_w = T_{aw}$. In experimental studies, several points are often used with a linear regression to reduce the effect of random measurement errors.

In principle, once the adiabatic HTC is obtained, it should be able to be used to predict wall temperatures for any temperature of freestream at the same Reynolds number. To this end, the adiabatic HTC works well when the heat transfer is governed by the

aerodynamics, but does not feed back in to them. This is not the case in some flows, including rotating cavities.

It can be shown that wall heating destabilises canonical low-speed boundary layers in air, potentially promoting earlier transition and enhanced local heat transfer (or vice versa) (Özgen, 2004), and there have been several observations of this in gas turbine heat transfer: e.g. Campanaro and He (2022); Maffulli and He (2014, 2017) have all observed transition to turbulence to be sensitive to the near-wall heating.

This means that at different temperature ratios (corresponding to different wall temperatures), the local value of $\partial q/\partial T_w$ is different to the value at T_{aw}. This fundamentally limits the adiabatic HTC as a tool for extrapolation from low temperature ratio studies to engine relevant conditions. Maffulli and He (2014, 2017) addressed this with a first order Taylor expansion of the adiabatic HTC in terms of wall temperature - accounting for the temperature dependent nonlinearities in the fluid domain in this way was observed to give much better agreement with CHT analyses conducted at different temperature ratios than where the HTC was calculated, although it required at least three simulations (instead of two) to fix the parameters.

This situation is even more challenging in rotating cavities, given that the cavity aerodynamics are almost entirely driven by buoyancy. This means that an adiabatic wall temperature can not easily be found - the adiabatic wall temperature itself is a function of the wall temperature, so two-point or linear regression approaches are not valid. *This is at the heart of the need for conjugate heat transfer of rotating cavities in a commercial context.*

It is relevant to note that, even though the adiabatic HTC is much more robust as an invariant, the conventional definition is more convenient. As a result, conventional

HTC-like approaches are still sometimes used where the wall temperature is not known, even in high-resolution turbulence resolved CFD studies that aim to emulate unsteady CHT (e.g. Agostinelli et al. (2021); Flageul et al. (2015)). While in principle the HTC could be unsteady, in practise it is not - here, another issue arises, which is that although a constant HTC may allow temperature fluctuations on the wall, it can not replicate the transient response of the wall temperature to heat flux fluctuations. This has a phase lag and is frequency dependent (Schultz and Jones, 1973).

Unsteady CHT comes with its own challenges, the most significant is finding a way to consistently deal with the fluid-solid timescale disparity - the timescale of the initial transient in the solid domain is generally four orders of magnitude larger than in the fluid domain (He and Oldfield, 2011), rendering unsteady CHT impossible without specialised methodology that goes beyond simply coupling the fluid and solid domain energy equation calculations.

Unsteady simulation - including unsteady CHT - is a requirement for the second grand challenge (off-design turbofan engine transient simulation) in the NASA CFD Vision 2030 study (Slotnick et al., 2014). The study cites the lack of accurate, stable frameworks for coupling high-fidelity CFD with other physics (such as solid domain conduction) as a limiting factor on current multidisciplinary design and analysis, and on future prospects. It is therefore vital to develop new CHT methods that can properly deal with the complex multiscale challenges that arise in unsteady CHT.

1.2 Research Aims

The research in this thesis has two broad aims. The first is to improve the knowledge of the flow structures responsible for heat transfer in rotating cavities and the

computational fidelity (in terms of turbulence modelling and thermal boundary conditions) required to model them. The second is to demonstrate issues in the current state-of-the-art unsteady CHT methods around their treatment of the fluid-solid timescale disparity, and develop a new multiscale framework that allows efficient unsteady CHT solutions that can calculate accurate wall temperature fluctuations, while not being contaminated by the solid material initial state.

1.3 Research Impact

Papers

- Hickling, T. and He, L. (2022). A multiscale framework for unsteady conjugate heat transfer with turbulence resolving methods — with application to rotating cavities. Submitted to *International Journal of Heat and Fluid Flow*.
- Hickling, T. and He, L. (2023). LES-CHT for a rotating cavity with axial throughflow. *Journal of Turbomachinery*, 145.
- Hickling, T. and He, L. (2021). Some observations on the computational sensitivity of rotating cavity flows. *Journal of Engineering for Gas Turbines and Power*, 143.

Conferences

Work from this thesis has been presented at four conferences - ASME Turbo Expo 2020, UK Fluids Conference 2021, ASME Turbo Expo 2022, and Osborne Reynolds Day 2022.

Awards

Hickling and He (2021) won a best paper award from the Heat Transfer Committee at ASME Turbo Expo 2020. It was also awarded the ASME Gas Turbine Award for the best paper published on the subject of gas turbines in 2020.

A long abstract and presentation on the work in this thesis won a runner-up prize at Osborne Reynolds Day 2022 for the best fluid dynamics PhDs in the UK, and was submitted as one of the UK nominations for the Europe wide ERCOFTAC Da Vinci competition.

1.4 Thesis Overview

The remainder of this thesis begins with a review of literature relevant to rotating cavities and conjugate heat transfer, indicating aspects of rotating cavities and CHT that need to be further investigated for this research to meet its aims. A baseline fluid domain modelling study is then conducted - the results of this analysis are used to make the case for our later development of techniques for using LES with CHT. The next chapter examines the conduction part of an unsteady CHT solution, demonstrating a flaw in how most methods for LES-CHT account for the fluid solid timescale disparity. A new multiscale framework for LES-CHT is then developed to address this in the following chapter. In the subsequent two chapters, the novel framework is applied to LES-CHT of rotating cavity flows. The solutions are first investigated from a CHT methodology perspective, before also been investigated to highlight the insights that can be gained from high fidelity conjugate computations.

Chapter 2

Literature Review

2.1 Introduction

This chapter reviews the existing literature on two topics. The focus is first on compressor inter-disk cavity flows. After a brief outline of their large-scale flow structure and expected behaviour in the near-wall regions, past numerical investigations into rotating cavities are discussed to assess the consensus within the community on the required turbulence modelling fidelity for them. The second area of focus is CHT. A top level overview of fluid-solid coupling approaches is given, along with a more detailed discussion on the multiscale issues (in both space and time) that arise when considering unsteady CHT. Before moving on with the rest of the thesis, three outstanding issues identified during the literature review are restated and related to an outline of the remaining chapters.

2.2 Compressor Inter-Disk Cavity Flows

2.2.1 Large Scale Flow Structure

In compressor internal air-system cavities, the shroud (see Fig. 2.1) is usually hotter than the cobs at the bottom of the cavity disks, which are cooled by the axial throughflow of bleed air that will later be used to cool the turbine (Chew and Hills, 2007). This radial temperature gradient can cause an unstable density gradient within the cavity, which interacts with the centrifugal and Coriolis pseudo-forces to form a large scale inertial wave-like flow structure that consists of pairs of circulations that slip relative to the cavity at a speed of about 10% of the cavities rotational speed (Owen and Long, 2015). A diagram of this flow structure, showing one circulation pair, is shown in Fig. 2.2.

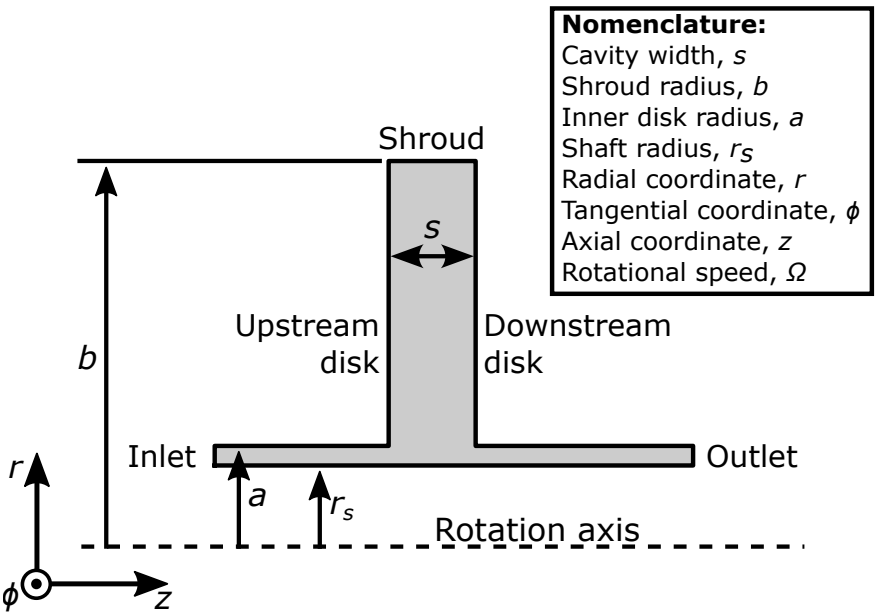

Figure 2.1. Rotating cavity nomenclature and coordinate system.

The reason for the formation of these flow structures is well established. It may be

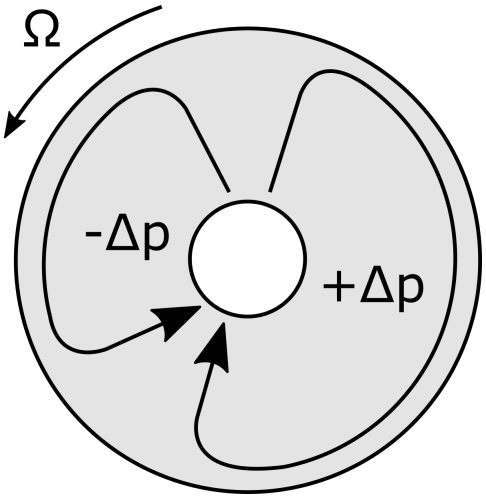

Figure 2.2. Typical rotating cavity mid-plane flow structure with one circulation pair.

explained with the inviscid Navier-Stokes equations, which can be rearranged to show that a circumferential pressure gradient is necessary for the occurrence of radial flow in a rotating fluid (Childs, 2011). As illustrated in Fig. 2.2, pairs of cyclonic circulations (with a reduced pressure, denoted by $-\Delta p$), and anti-cyclonic circulations (with an elevated pressure, denoted by $+\Delta p$) form, creating alternating regions of radial inflow and outflow. The alternating regions of high and low pressure generate the circumferential pressure gradients necessary to balance the Coriolis force from the radial inflow and outflow. The strength of the radial flow is dependent on the strength of the circulations, which affects the strength of the circumferential pressure gradients. This in turn influences the strength of the circulations and the strength of the radial flow. Through this positive feedback loop, the possibility for self-excited disturbances to develop into sustained large scale flow patterns can be seen (He, 2011).

Owen (2010) hypothesised that the number of vortices that form is dependent on the cavity geometry - the most probable number of circulations would correspond to the number where the circulations are most circular, with a diameter of $b - a$. This yielded

a formula for the number of circulations as

$$N_{RA} = \frac{\pi}{2}\frac{(a+b)}{(b-a)}. \tag{2.1}$$

In a comparison to various computations on closed rotating cavities, Owen (2010) found that this ad-hoc hypothesis gave surprisingly good predictions.

Bohn et al. (2006) observed that the number of circulations within the cavity is not necessarily constant - in both experiments and computations, the number of circulations observed within a cavity with axial throughflow varied in a limit cycle from one to two to three circulations and back down again. Long and Tucker (1994a) also observed this in their computations. Bohn et al. (2006)'s computations used a gravity vector fixed in the inertial frame of reference, so it is unclear whether their limit cycle is a result of periodic forcing or a natural instability in the flow. Using the maximum entropy production from nonequilibrium thermodynamics for self organising systems, Owen (2010) showed that a change in number of circulations would result in a reduction in heat transfer from the cavity. This was corroborated in computations in Bohn et al. (2013), who found that changes in number of circulations did indeed occur at disk heat transfer minima. It is worth noting that, as far as this author is aware, Bohn et al. (2013, 2006); Long and Tucker (1994a) are the only computations where this limit cycle has been observed, so whilst interesting, its relevance to rotating cavity flows in gas turbines is perhaps limited.

2.2.2 Non-Dimensional Parameters

Three dimensionless parameters are necessary to fully describe the operating conditions of a rotating cavity with axial throughflow. These are the axial Reynolds number Re_z, the rotational Reynolds number Re_ϕ, and the buoyancy parameter

$\beta\Delta T_{max}$. These are given by

$$Re_z = \frac{\rho_{in} V_z d_H}{\mu_{in}}, \tag{2.2}$$

$$Re_\phi = \frac{\rho_{in} \Omega b^2}{\mu_{in}}, \tag{2.3}$$

and

$$\beta\Delta T_{max} = \frac{T_{max} - T_{in}}{T_{in}}. \tag{2.4}$$

The bore hydraulic diameter, d_H is given by $d_H = 2(a - r_s)$, Ω is the rotational speed of the cavity, and V_z is the velocity of the axial throughflow. T_{max} and T_{in} are the maximum disk temperature and the inlet temperature of the throughflow, ρ_{in} and μ_{in} are the density and dynamic viscosity at the cavity inlet, and a, b, and r_s are geometric parameters defined in Fig. 2.1.

Another relevant non-dimensional groups is the Grashof number

$$Gr = \left(1 - \frac{a}{b}\right)^3 Re_\phi^2 \beta\Delta T_{max}, \tag{2.5}$$

which describes the ratio of buoyancy to viscous forces. The Rayleigh number can be calculated by multiplying Gr by the fluid Prandtl number Pr, and the Rossby number is given by

$$Ro = \frac{V_z}{\Omega a} = \frac{b^2}{a d_h} \frac{Re_z}{Re_\phi}. \tag{2.6}$$

Ro can be thought of as the ratio of inertial to Coriolis forces in a rotating fluid, so that the effects of the axial throughflow dominates at large values of Ro, and rotational effects dominate at smaller values (Owen and Long, 2015). Engine relevant orders of magnitude of these non-dimensional parameters are given in Tab. 2.1.

The heat flux from the cavity disks and shroud is often normalised using a Nusselt

Table 2.1. Engine relevant orders of magnitude for governing non-dimensional parameters (Hickling and He, 2021; Owen and Long, 2015)

Parameter		Value
Axial Reynolds number	Re_z	$\sim 10^5$
Rotational Reynolds number	Re_ϕ	$\sim 10^6$
Buoyancy parameter	$\beta \Delta T_{max}$	$\sim 10^{-1}$
Rossby number	Ro	~ 1
Grashof number	Gr	$\sim 10^{12}$

number, given by the equation

$$Nu = \frac{qr}{k_{in} \Delta T_w}, \tag{2.7}$$

where $\Delta T_w = T_w - T_{in}$. An alternative Nusselt number (Nu_{sh}) is sometimes used on the shroud, this is defined in the same way as Nu, except the radial coordinate r is replaced by half the cavity width, $s/2$. It is important to note that these are not true Nusselt numbers in the sense of

$$Nu^* = \frac{HTC_a \, L}{k} \tag{2.8}$$

due to the previously discussed issues surrounding finding a value for the heat transfer coefficient in rotating cavity flows. As such, they do not provide an invariant non-dimensional description of the heat transfer to be compared from case to case, and are more a neatly normalised heat flux. That said, within the rotating cavities community, Nu and Nu_{sh} are usually reported as Nusselt numbers, so this thesis follows that convention.

2.2.3 Behaviour of the Near-Disk Flow

It is possible to find analytical expressions for the velocity in the near-disk regions of the rotating cavity. Under the assumption that the Coriolis forces in the rotating fluid in

the cavity are much greater than the inertial forces, the boundary layer equations (themselves derived from a simplification of the full Navier stokes equations) can be simplified to give a set of linear equations called the Ekman layer equations, that express a balance between the local shear stresses and Coriolis forces.

Assuming that the radial velocity in the bulk, or core, flow is zero (in the time-average sense), these linear Ekman layer equations can be written as

$$\begin{cases} \dfrac{\partial \tau_r}{\partial z} = -2\rho\Omega(V_\phi - V_{\phi,core}) \\ \dfrac{\partial \tau_\phi}{\partial z} = 2\rho\Omega V_r \end{cases}, \tag{2.9}$$

where τ_r and τ_ϕ are the radial and circumferential shear stresses, ρ is the fluid density, Ω is the cavity rotational speed, V_r and V_ϕ are the radial and relative circumferential velocities, and $V_{\phi,core}$ is the cavity core relative circumferential velocity (Childs, 2011).

Laminar linear Ekman layers

For laminar flows, these equations can be solved to give the laminar Ekman layer equations, which express the velocities at a distance of Δz from the wall as

$$\begin{cases} V_r = -V_{\phi,core} \exp\left(\dfrac{-\pi\Delta z}{\delta_{Ek}}\right) \sin\left(\dfrac{\pi\Delta z}{\delta_{Ek}}\right) \\ V_\phi = V_{\phi,core}\left[1 - \exp\left(\dfrac{-\pi\Delta z}{\delta_{Ek}}\right) \cos\left(\dfrac{\pi\Delta z}{\delta_{Ek}}\right)\right] \end{cases}. \tag{2.10}$$

Here, δ_{Ek} is the laminar Ekman layer thickness, which describes the first off-wall location where the radial velocity is zero. The laminar Ekman layer thickness is given by

$$\delta_{Ek,lam} = \frac{\pi b}{\sqrt{Re_\phi}}. \tag{2.11}$$

Turbulent linear Ekman layers

Equation (2.9) is also valid in turbulent flows - assuming a $1/7^{th}$ power law for the velocity in the turbulent Ekman layer, Childs (2011) found that the velocity in a turbulent Ekman layer could be given by

$$\begin{cases} V_r = r\Omega \left(\frac{\Delta z}{\delta_{Ek}}\right)^{1/7} \left[1 - \min\left(\frac{\Delta z}{\delta_{Ek}}, 1\right)\right] \\ V_\phi = V_{\phi,core} \min\left(\frac{\Delta z}{\delta_{Ek}}, 1\right)^{1/7} \end{cases}, \tag{2.12}$$

where the turbulent Ekman layer thickness (which has the same meaning as in the laminar case) is defined as

$$\delta_{Ek,turb} = 0.0983\, b \sqrt{Re_\phi} \left(\frac{|V_{\phi,\text{core}}|}{\Omega b}\right)^{0.6}. \tag{2.13}$$

As in other canonical flows, the turbulent near-wall layer is less thick than the laminar near-wall layer - this is due to the enhanced mixing of core flow high momentum fluid into the near-wall region in the turbulent case.

Ekman layers in rotating cavities

The consensus in the rotating cavity community is that the Ekman layers remain laminar, even at engine relevant conditions. Many papers give evidence for this, most recently high-fidelity computational studies such as Gao and Chew (2021, 2022); Saini and Sandberg (2021). This is reinforced by fundamental isothermal experimental studies, such as Lingwood (1997); Owen and Pincombe (1980) who observed that the occurrence of instabilities in the Ekman layer is dependent on the magnitude of the radial velocities, which in the absence of radial in/outflow of the cavity, it is reasonable to expect to be fairly limited in the buoyancy driven flow structure, even at engine

relevant speeds. Whether heat transfer affects this in the same way that it does in canonical boundary layer flows (see Özgen (2004)) had not been investigated before this thesis. In addition, there is still little knowledge of how Ekman layers respond to external disturbances - both from the large scale rotating cavity flow structure and smaller scale eddies that form away from the cavity walls.

The laminar Ekman layer modelling consideration has been used quite successfully with empirical calibration from experimental results to build reduced order models for the flow in rotating cavities. An example of this that is relevant to our later consideration of conjugate heat transfer in this thesis is the work of Tang and Owen (2017), who coupled their reduced order model for the flow within the cavity to a fin equation based model to predict the disk temperatures, achieving good agreement with the experimental data of Atkins and Kanjirakkad (2014).

2.2.4 Experimental Investigations

A thorough review of all work carried out on rotating cavities pre-2015 was published by Owen and Long (2015) - as the subject of this thesis is computational modelling, the discussion on experimental modelling is intentionally short. Only a brief listing of three experimental rigs that have provided some of the useful data sets[1] and test cases for the validation of numerical studies on open rotating cavities with axial throughflow is provided here: the measurements of Farthing et al. (1992), Long and Tucker (1994b), and Long (1994) on the University of Sussex single cavity rig; the measurements of Bohn et al. (2000) on the RWTH Aachen University single cavity rig; and the measurements of several authors (e.g. Atkins and Kanjirakkad (2014), Puttock-Brown et al. (2017)) on various builds of the Multiple Cavity Rig facility at the

[1] For the purposes of this thesis, the limiting factor on what cases could be used was the availability and completeness of the geometry description, not the quality or availability of experimental measurements.

University of Sussex. For more information on experimental studies of rotating cavities, the review of Owen and Long (2015) is an excellent starting point. It is worth noting that there have been also been investigations on cavities with radial in/outflow (Atkins, 2013; Owen and Pincombe, 1980), and closed cavities (Bohn et al., 1995).

2.2.5 Computational Investigations

Axisymmetric and reduced order methods

Methods that allow for rapid predictions are important as a component of iterative design cycles. Two approaches with this are discussed in this literature review: axisymmetric steady RANS computations, and reduced order models.

Axisymmetric RANS computations have been extensively used in coupled analyses, particularly in simulations of full flight cycles (Atkins, 2013; Sun et al., 2015, 2010). However, axisymmetric steady RANS models are limited in that they can not capture and are not calibrated for the strongly 3D, unsteady flow structure in rotating cavities. For this reason, there has been interest in developing RANS models that are empirically tuned to reasonable results - an example of this is the enhanced mixing model of Kilfoil and Chew (2009).

Tang and Owen (Owen and Tang, 2015; Tang and Owen, 2017, 2021, 2022; Tang et al., 2015) have had considerable success building a reduced order modelling framework (based on, among other assumptions the laminar behaviour of the cavity disk Ekman layers) that includes fluid-solid thermal interactions and radiation within the cavity disks. Being reduced order models, there are several free parameters that are tuned by comparison to experimental data.

Whilst these approaches can be successful, they require calibration and insight either from experimental data or fully 3D unsteady CFD computations. Different levels of

turbulence modelling fidelity for carrying out the latter are discussed below.

Coarse mesh numerical LES

Many early CFD analyses of rotating cavities with axial throughflow used laminar computations with large cell sizes. This is effectively a numerical LES (NLES) that is able to resolve only the very largest eddies and implicitly models the sub-grid effects with numerical dissipation from the discretization scheme. In some flows, Yao and He (2020) found that this kind of simulation performs better than URANS.

These computations sometimes captured an unsteady number of circulations; Long and Tucker (1994a) found that the flow vacillated between one and two radial arms, and Bohn et al. (2013); Bohn and Ren (2009); Bohn et al. (2006) captured a limit cycle behaviour where the flow oscillated between one, two, and three circulation pairs. The durations of these oscillations were found to correspond to experimental smoke flow visualisation.

To reduce the computational cost of these simulations He (2011) modelled the same case as Bohn et al. (2006) using a Fourier spectral decomposition in the tangential direction to capture the large scale circulations. Six or seven harmonics were found to be sufficient to accurately reproduce the shroud heat flux from a 300 circumferential cell base mesh, this corresponded to a 20- to 23-fold reduction in the number of cells to be solved. Both the base and Fourier harmonic solution failed to reproduce the pattern transition found by Bohn et al. (2006). However, the number of circulation pairs was found to be sensitive to inlet total pressure distortions.

URANS computations

It has been suggested that URANS is not suitable for turbulence modelling in rotating cavities; Tucker (2011) claimed that compressor cavity flows had 'proved hopeless for URANS type modelling'. As previously discussed, this lack of trust in URANS can be attributed to the need for a spectral gap between the resolved coherent scales and modelled stochastic unsteadiness (Palkin et al., 2016), and double counting of unsteady turbulent structures in regimes such as wake flows and vortex shedding Tucker (2013); Yao and He (2020).

Even when the above considerations are not an issue, URANS is limited by its inherent empirical nature; it is well known to struggle to capture the effects of buoyancy, stratification, rotation, streamline curvature, and transition. All of these are relevant for rotating cavity flows. It is therefore confusing that many simulations that have been conducted with URANS Dweik et al. (2009); Owen et al. (2007); Puttock-Brown et al. (2017); Tan et al. (2009, 2014) have provided reasonable predictions of the disk heat flux.

URANS has a consistent issue with accurately predicting the shroud heat transfer, particularly at higher rotational speeds, as seen in computations by Sun et al. (2007) and Puttock-Brown and Rose (2018) (with the latter under-predicting the heat flux by 31%). Having said that, URANS has been used to investigate near-shroud flow structures with some success - Puttock-Brown and Rose (2018); Puttock-Brown et al. (2017) carried out high resolution URANS computations at Grashof numbers of between 7.94×10^{11} and 8.94×10^{11}. These simulations predicted the presence of streaks, a previously unobserved flow structure. The streaks took the form of counter rotating vortices in the near shroud region of cyclonic circulations, and were proposed to be formed by buoyancy effects. The streaks modified the local Nusselt number by

as much as 40%, but have yet to be seen experimentally. Prior to this thesis, these streaks have never been captured using LES, even though one would expect them to be present when the turbulence model intends to resolve the smaller scales of the flow. Thus, if streaks are a universal feature of rotating cavity flows, it is of interest to know whether URANS can consistently model them, or if higher fidelity methods are necessary for a confident prediction of shroud heat transfer.

URANS/LES hybrid computations

Hybrid URANS/LES computations have been used several times to model rotating cavity flows due to the large computational cost of fully resolving near-wall turbulent boundary layers at engine relevant conditions. Atkins and Kanjirakkad (2014) carried out two hybrid URANS/NLES computations at Grashof numbers of up to 7.73×10^{11}. These computations were zonal, in that the URANS model was hard coded to only be active within a certain distance of the wall. At higher rotational speeds, the shroud heat flux reversed the local density gradient, generating buoyant structures that reduce the temperature at higher radii. This effect was also observed in experimental data in the same paper.

Tateishi et al. (2018) carried out a detached eddy simulation (DES) of a full compressor internal flow path. The authors observed interaction effects between the cavities, in particular the formation of a hot cell by radial inflow.

Very Large Eddy Simulations using a Lattice-Boltzmann solver were reported by Kouwa et al. (2018) at Grashof numbers of up to 7.17×10^{11}. The mesh was refined locally around walls and in the axial throughflow/cavity shear layer. The results were verified with a mesh refinement study and validated with experimental disk heat transfer data.

Gao and Chew (2022) conducted wall modelled LES computations at Grashof numbers of up to 1.2×10^{12}. Their simulations underpredicted experimental shroud heat transfer measurements by between 11% and 24% depending on the case, and the disk heat transfer was found to be consistent with conduction across the observed laminar Ekman layers.

Focus has generally been on the ability of wall modelled URANS/LES hybrid methods to eliminate the excessive computational cost of resolving the near-wall region with LES. There has been little consideration of the validity of these methods for heat transfer in rotating cavities - their performance is expected to be limited by the performance of the URANS model in the near-wall layer, which is critical for heat transfer. There is an interesting contradiction between the widespread use of turbulence (RANS or log-law) based wall modelling approaches, and the apparent consensus within the rotating cavity community that the Ekman layers behave in a laminar fashion.

LES computations

LES is the highest fidelity method considered in this report, and the least empirical. The first reported LES computations on rotating cavities were by Sun et al. in 2007 Sun et al. (2007). LES was found to give a much higher shroud heat flux than URANS, and had errors (compared to experimental data) that were in the range of $-25\,\%$ to $6\,\%$. The $-25\,\%$ error in the shroud heat flux was at Gr = 1.01×10^{11}, the highest Grashof number simulated.

Tan et al. (2009) compared URANS and LES computations on the experimental data of Bohn Bohn et al. (2000) at a Grashof number of 3.03×10^{9}. They found URANS and LES gave similar errors in the prediction of disk heat transfer, although the LES

disk heat flux fluctuated significantly more than that of URANS.

LES computations at a Grashof number of 1.88×10^8 were reported by Pitz et al. (2019b). Of particular interest in these computations was that the computed kinetic boundary layer thickness (based on the peak magnitude of the radial velocity fluctuations) was found to closely match the theoretical laminar Ekman layer thickness. In a closed rotating cavity, Pitz et al. (2019a) used the same method for determining the Ekman layer to show that the scaling of the disk boundary layer thickness remained consistent with a laminar Ekman layer at similar Grashof numbers.

Saini and Sandberg (2021) conducted very highly resolved high Rossby number LES simulations at Grashof numbers of 1.017×10^8 and 2.16×10^8. They observed that the thickness of the near-disk layers was consistent with a laminar Ekman layer at the low Grashof number condition, but the thickness deviated from a laminar Ekman layer at the higher Grashof number condition. Both cases were at the same rotational Reynolds number, so the deviation from laminar Ekman layer behaviour could to be due to thermal effects, although Saini and Sandberg (2021) attributed it to increased forcing of the near-disk flow in the higher Grashof number case.

Sun et al. (2022) compared single and dual rotating cavities. They found that, in the dual cavity configuration, a complex phase locking mechanism between the cavities resulted in less stable flow structures, higher air temperatures within the cavities, and reduced shroud and disk heat transfer compared to an isolated cavity.

Meshing for LES

The usual approach to assessing the wall resolution of simulations is to look at the value of the normalised wall distance - Tan et al. (2009) and Sun et al. (2007) provide examples of this for LES of rotating cavities. According to Sagaut (2006), the general

wall resolution requirement for LES of channel flow is normal, stream-wise, and span-wise spacings of less than 1, 50, and 15 units, respectively. Whether this is valid for rotating cavity flows is unclear - neither the disk or the shroud near-wall layers are similar to the classical boundary layers on which these requirements are based.

The mesh sizes and Grashof number of some previous simulations of rotating cavities are plotted in Fig. 2.3. There is no clear separation between the mesh sizes for the different modelling fidelities - one would expect three clear groupings, one for each of LES, URANS/LES hybrids, and URANS (from large mesh counts to small). Here, we see that some URANS and LES meshes are often of a similar size, and that, unexpectedly, hybrid computations have used larger mesh sizes than the LES computations that claim to resolve the near-wall flow at similar conditions. There also appears to be a cluster of very high cell count LES simulations at low Grashof numbers - this either implies that the LES simulations at $Gr > 1 \times 10^9$ are under resolved, or that the simulations at $Gr < 1 \times 10^9$ are over resolved for practical purposes.

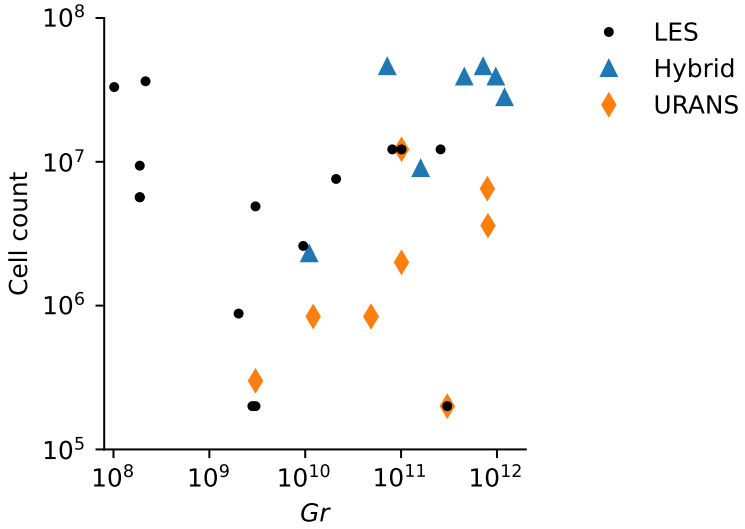

Figure 2.3. Mesh scaling of previous simulations of rotating cavities.

In any case, it is clear that there is a degree of inconsistency in how modelling and

meshing for rotating cavity flows is approached, and a need for clearer understanding of the behaviour and relevant scales of the flow to enable CFD practitioners to make more informed choices on what modelling fidelities and mesh resolutions are appropriate to use, and where.

2.3 Conjugate Heat Transfer

2.3.1 Coupling the Fluid and Solid Domain

Two physical conditions need to be satisfied on a fluid-solid interface in a CHT analysis: the conservation of heat flux, and the continuity of temperature. To do this, two broad classes of method are used: loosely coupled approaches, and directly coupled approaches. These are discussed below.

Loosely coupled CHT

Loosely coupled refers to a CHT analysis with Neumann-Dirichlet boundary conditions on interface between the fluid and solid domains. Loosely coupled CHT indirectly enforces heat flux conservation and temperature continuity on the interface once a fixed point iteration between the fluid and solid domains has converged. To accelerate the convergence of the fluid-solid fixed-point iterations, Robin-Dirichlet interface conditions are also used - however these do not necessarily provide enforcement of conservation and continuity when the iterations have converged (He and Fadl, 2017). In both of these coupling methodologies, the Dirichlet (fixed value, i.e. temperature) boundary condition is applied to the fluid domain, and the Neumann (fixed gradient, i.e. heat flux) or Robin (a fixed linear combination of Neumann and Dirichlet conditions, i.e. HTC) boundary condition is applied to the solid domain. They are often implemented

in partitioned CHT frameworks, where specialised codes are used for both the fluid and solid domains; and data is transferred between these codes to allow them to interact Tucker (2016).

Loosely coupled approaches are not used in this thesis, despite being popular for unsteady CHT computations (e.g. (Duchaine et al., 2009; Fadl and He, 2017; Jaure et al., 2013)). There are two reasons for this:

- They do not guarantee conservation and continuity on the interface - the fixed point iteration between the fluid and solid domains can be computationally expensive to converge, leading to considerable work on convergence acceleration methods (e.g. Anderson acceleration as used by Ganine et al. (2013), and the adaptive HTC approaches of Errera and Chemin (2013); Errera and Duchaine (2016))
- Due to the expense and complexity of transferring data between codes, loosely coupled unsteady CHT codes often do not couple the fluid and solid domains at every time step, leading to additional issues arising around spurious temperature fluctuations in the solid created by aliasing, as observed by Jaure et al. (2013).

Directly coupled CHT

Directly coupled refers to methods where both conservation and continuity are enforced on the interface at every iteration and time-step through a Dirichlet-Dirichlet interface condition where the same wall temperature is applied to both the fluid and solid domains (He and Oldfield, 2011). These are generally implemented in monolithic CHT codes where both the fluid and solid domain data is stored in the same processes. As well as guaranteed enforcement of the conservation and continuity, directly coupled CHT has practical advantages - there is no need to carry out the

expensive inter-process communication necessary to transfer data between solvers, and there is better data locality, making parallel processing easier (He, 2019).

2.3.2 Time and Length Scales in Unsteady CHT

Timescales: temperature fluctuations and the initial transient

There are a large range of time- and spatial-scales that feature in unsteady CHT, especially when using turbulence resolving methods in the fluid domain. There are short timescales (i.e. high frequency) coming from turbulence within the fluid, as well as longer ones coming from unsteady large coherent structures such as the passing of rotating cavity radial arms. In addition, there is also the long solid timescale, which can exceed those in the fluid domain by four orders of magnitude (He and Oldfield, 2011). The timescale disparity between the fluid and solid domains makes the cost of a temporally converged unsteady CHT solution prohibitive without acceleration methods - it would require four orders of magnitude more time steps than a standalone fluid domain simulation.

Length scales: the thermal penetration depth

The timescales also have an associated spatial scale in the solid domain. This can be estimated by considering a sinusoidal wall temperature at frequency f applied to a 1D semi-infinite solid domain with thermal diffusivity α_s. The magnitude of local temperature fluctuations decays according to $\exp(-x\sqrt{\pi f/\alpha_s})$, where x is the distance from the wall (Incropera et al., 2013). This decay of the temperature oscillation amplitude leads to the concept of a "thermal penetration depth", denoted by δ_p. δ_p is taken to be where the amplitude of the temperature oscillation has decayed to

1% of its value at the wall, giving

$$\delta_p = \frac{\ln(100)}{\sqrt{\pi}}\sqrt{\alpha_s/f}. \tag{2.14}$$

The thermal penetration depth must be properly captured for an accurate unsteady conduction analysis in the solid. This was analysed in the context of directly coupled unsteady CHT by Fadl and He (2017), who investigated the scenario shown in Fig. 2.4 where the solid domain mesh spacing is larger than the thermal penetration depth. This is at its heart an aliasing issue - the under-resolved temperature fluctuation has a physical length scale of δ_p, which is aliased by the solid mesh up to a length scale of Δx_s. As the solid domain is a constant temperature (T_s), the incorrect length scale results in an incorrect temperature gradient near-wall; which when combined with the requirement for the fluid and solid heat fluxes to be conservative (as enforced by the interface treatment) results in an over predicted wall temperature fluctuation. It is reasonable to expect other numerical methods (finite elements are particularly of interest for loosely coupled CHT) to exhibit the same behaviour - if the location of the first solution point is not within δ_p of the wall, the temperature fluctuation will be aliased up to Δx_s, and the same magnification of temperature fluctuations can be expected to occur. As this is a length scale issue, it is the author's expectation that moving to higher orders will not alleviate this - the location of the first solution point is key.

Assuming a linear variation of the (accurate) temperature within the thermal penetration depth, they showed that the ratio of the erroneous under-resolved wall temperature fluctuation to accurate wall temperature fluctuation amplitude would be given by

$$\frac{|\hat{T}'_w|_{err}}{|\hat{T}'_w|} = \frac{1 + (Bi_m/\beta)}{1 + Bi_m}, \tag{2.15}$$

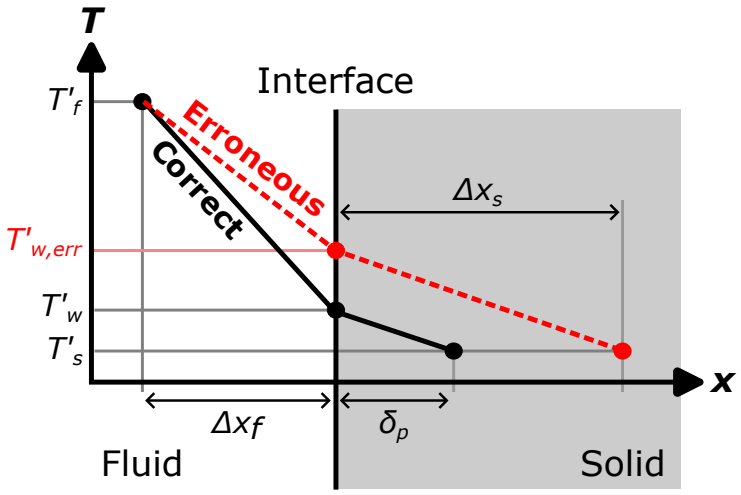

Figure 2.4. Realistic and erroneous unsteady temperature variations at a fluid-solid interface. The thermal penetration depth has been aliased up to the solid domain mesh spacing, resulting in an incorrect interface temperature.

and for the heat flux fluctuation,

$$\frac{|\hat{q}'_w|_{err}}{|\hat{q}'_w|} = \frac{Bi_m + \beta}{Bi_m + 1}. \tag{2.16}$$

Here, the ratio of the under resolved thermal penetration depth to Δx_s is given by

$$\beta = \delta_p / \Delta x_s < 1, \tag{2.17}$$

and the interface mesh Biot number is given by

$$Bi_m = \frac{h_s}{h_f} = \frac{k_s}{\Delta x_s} \frac{\Delta x_f}{k_f}. \tag{2.18}$$

Equation (2.15) predicts that, when $\beta < 1$, the erroneous under-resolved temperatures fluctuations will be larger than the accurate temperature fluctuations as a consequence of conservation and continuity being enforced on the interface. Similarly, Eq. (2.16) predicts that, for the same condition on β, the under resolved heat flux

fluctuations will be lower than in the properly resolved case.

As predicted by the interface response analysis, the magnitude of the error in the wall temperature fluctuation can be quite large - in (Fadl and He, 2017) it reached a factor of almost 10 for a low conductivity solid material. Changes in the behaviour of the unsteady wall temperature may have important effects on the mean-state flow and heat transfer due to non-linear effects caused by temperature dependent properties, the coupling of the momentum and energy equations, or other temperature dependent processes in the fluid domain (e.g. combustion, as observed in Shahi et al. (2015)).

2.3.3 A Multiscale View of Unsteady CHT

The presence of multiple distinct scales implies that it may be useful to consider a multiscale framework for unsteady CHT to enable future turbulence resolved unsteady CHT computations to be conducted consistently. An overview of the scales of thermal unsteadiness that appear in turbulence resolved unsteady CHT computations is shown in Fig. 2.5, along with the relative sizes of the thermal penetration depth and the solid thickness L. Existing methodologies for addressing the issues at each timescale are discussed below:

Short fluid timescales

High frequency thermal fluctuations are particularly challenging to resolve due to their small penetration depth. This situation is exacerbated by the presence of thermal barrier coatings, which further reduce the distance that the disturbance can penetrate into the solid domain (He and Oldfield, 2011).

Even if the long solid domain initial transient caused by the fluid-solid timescale disparity has been properly accounted for, the small mesh spacing required to resolve

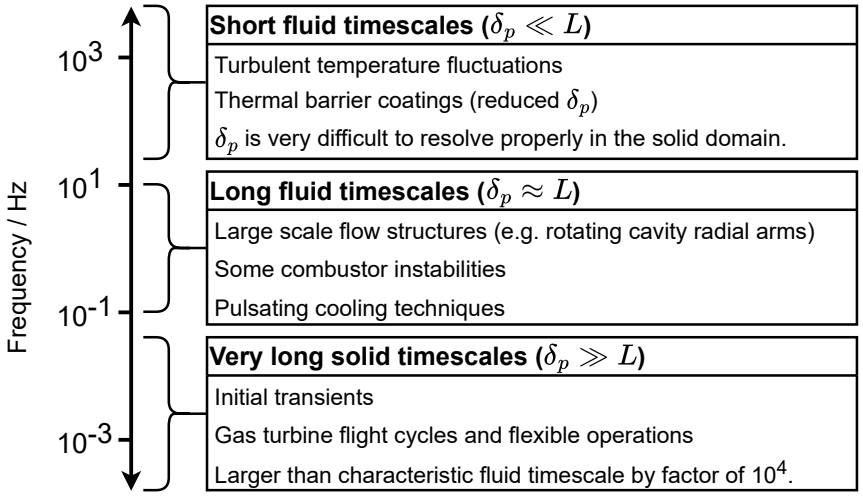

Figure 2.5. Multiple scales of thermal unsteadiness relevant to unsteady CHT with turbulence resolving methods.

δ_p at the highest frequencies present means that it is unfeasible to solve the solid thermal fluctuations and be assured of a solution that does not have erroneously large wall temperature oscillations.

He and Oldfield (2011) used a wall transfer function approach to directly relate the temperature fluctuations in the wall-adjacent cell to the wall temperature fluctuations. This approach relates harmonics of the off-wall temperature fluctuations to the harmonics of the wall temperature fluctuations. The wall temperature harmonics can then be used to reconstruct the wall temperature fluctuations in the time-domain. It is highlighted that this approach is completely local to the wall, and no unsteady components are required to be solved in the solid domain. This approach (with an appropriately modified wall transfer function) has been applied to LES-CHT of a turbine blade with thermal barrier coating in He (2019). Being in the frequency domain it correctly captures the temperature fluctuations at a constant time-average state without contamination by the initial transient. The validity of the semi-infinite assumption is easy to check by evaluating the thermal penetration depth, but the

validity of the local 1D assumption has not been discussed in relation to its use in unsteady CHT.

Long fluid timescales

Long fluid timescales sometimes occur when there is some large scale instability or coherent structure in the fluid. They can be found in combustor instabilities (Jaure et al., 2013), as well as from the periodic passing of the cold fluid in a radial arm in rotating cavities (Hickling and He, 2021). These timescales also appear in pulsating approaches to heat transfer enhancement (Mathie and Markides, 2013; Voigt et al., 2019; Zhang et al., 2022) - indeed some of these approaches explicitly rely on unsteady conjugate effects. Expanding on the discussion of He and Oldfield (2011), Scholl et al. (2016) note that if a low frequency fluid domain harmonic is 20,000 time steps long, a non-accelerated unsteady CHT simulation will need to be run for 40,000,000 time steps - rendering these sorts of computations unaffordable.

Accounting for these timescales of temperature fluctuation is challenging - they interact with the solid domain geometry and external thermal boundary conditions. To capture this it is necessary to solve them directly in the solid domain. Prior to this thesis, the only method to do this was a time domain solution in the solid domain - however as discussed below, this may lead to significant errors in the time-average temperature distribution.

Very long solid timescales

These timescales often appear in situations such as turbine warm-up/cool-down (Fadl and He, 2017) or in transient gas turbine cycles (Atkins, 2013; Sun et al., 2015). As discussed in Section 1.1.1, the latter are of key importance in predicting the maximum and minimum radial growth of the rotating cavity disks. These are usually dealt with in

a quasi-steady manner, whether the long timescale is considered as a sequence of steady states. In turbulence resolved computations, this can introduce errors due to the inconsistent treatment of the turbulence timescales in the fluid and the long solid timescales. A method to more accurately deal with this was introduced in Fadl and He (2017); He and Fadl (2017): the flow variables are decomposed into a long solid timescale component and a much shorter fluid timescale component. The large-scale solid temporal gradient provides a base source term to the unsteady flow equations at each short-scale fluid time-step, and the averaged short (fluid) timescale unsteadiness affects the evolution of the system on the large timescale.

More critically, the long solid timescale renders conducting consistent directly coupled unsteady CHT simulations in a fluctuating steady state almost impossible. Even for the flight cycle timescale computations that are most industrially relevant for rotating cavities this issue is still critical - unless accurate steady states can be reached efficiently, flight cycle computations are not practical (hence the dominant use of steady RANS in this area). This condition is where components will spend the majority of their service life - a transient startup of a land based gas turbine may take a few minutes, but its steady-state operation lasts for several hours (Oh et al., 2021).

To conduct a directly coupled unsteady CHT computation and reach a steady state to gather flow statistics, the simulation will need to be marched through 10,000 times as many flow-through periods than would be required if using a standalone fluid domain (He and Oldfield, 2011). A common way and consistent of overcoming this is to couple a moving average of the fluid near-wall temperature to a steady solid domain (e.g. Scholl et al. (2016)), removing the initial transient at the expense of information on the unsteady wall temperatures (without additional treatment). Another approach is to carry out a desynchronised solution with the solid domain timescale rescaled to be on

the same order as the fluid domain until temporal convergence is achieved - examples of this for unsteady CHT are Agostinelli et al. (2021); Kraus et al. (2018); Oh et al. (2021). These approaches then switch to an unsteady CHT solution with the correct accelerated solid timescale. It is assumed that this will give a solution free from the effects of the initial transient, however despite claims to the contrary (He, 2019) this has not been investigated. Duchaine et al. (2009) used a similar approach, but did not revert the solid domain timescale back to its non-accelerated value once temporal convergence had been reached - as long as the temperature fluctuations in the solid domain do not affect the fluid domain dynamics, this approach yields accurate steady states at the expense of a time-accurate solution of the solid domain.

2.4 Outstanding Issues to be Addressed in this Thesis

This thesis seeks to address three questions to meet the aims outlined in Chapter 1.

1. What modelling fidelity (in terms of turbulence and thermal boundary conditions) is necessary to accurately simulate the effects of all flow structures in rotating cavity flows?

2. How consistent are the accelerated methods for unsteady CHT? Is it possible to carry out a time domain solution in the solid domain, or is this inevitably contaminated by the initial transient?

3. Are the flow structures in rotating cavities affected by the inclusion of accurate heat transfer effects?

The first question is addressed in the next chapter, which, using fluid domain only simulations, addresses the unexpectedly good performance of URANS methods in

some rotating cavity simulations, mesh requirements for LES, and highlights some critical issues with hybrid URANS/LES methods in rotating cavities and heat transfer more broadly. Results from the simulations are also used to make a case from an aerodynamic standpoint for developing techniques for unsteady CHT of rotating cavities.

Then, the multiscale sensitivities of unsteady CHT mentioned in this literature review are thoroughly investigated, resulting in a set of requirements for conducting consistent unsteady CHT. These requirements are used to develop a novel multiscale framework which (as far as the author is aware) is the only framework capable of capturing all frequencies of unsteadiness accurately in unsteady CHT simulations. The multiscale framework is applied to rotating cavity flows, and the simulations are analysed to yield new insights into the effect of heating configuration and cavity disk material on the flow structures within the cavity.

Chapter 3

Baseline Modelling Study

3.1 Modelling Study Aims

Across the open literature, there is no clear consensus on what the most suitable modelling fidelity is for rotating cavity flows, and a degree of inconsistency on how modelling them is approached. As seen in the literature review, URANS, and LES meshes are often of similar sizes, and unexpectedly DES meshes have been used that are larger than LES computations that claim to resolve the near-wall flow at similar conditions. Although it is a widely held opinion that URANS approaches are unsuitable, many authors have succeeded in getting reasonable heat transfer results with them. There is also a lack of research into the validity of hybrid URANS/LES type approaches such as DES. Despite the flow in rotating cavities being an inherently conjugate problem, there has been little consideration of the effect of thermal boundary conditions in these flows.

The aim of this chapter is to establish baseline requirements for the simulation of

rotating cavity flows by addressing the following questions:

- What are the relevant flow mechanisms and structures in rotating cavity flows?
- How do these structures respond to different modelling fidelities and mesh resolutions?
- Is it necessary to include the interaction of the cavity flow and disk material to realistically simulate the cavity aerodynamics?

This chapter presents the experimental cavity and baseline computational methodology used in the rest of the thesis, before examining the results of computations at Grashof numbers of 3.03×10^9 and 3.03×10^{11}. The broad approach taken is to simulate the cavity with different turbulence modelling fidelities, mesh sizes, and thermal boundary conditions. The solver and numerics are kept the same so that any differences between simulations at the same condition are due to modelling fidelity or thermal boundary condition alone.

3.2 Experimental Test Case

The experimental rotating cavity of Bohn et al. (2000) at RWTH Aachen is used throughout this thesis as a test case. This rig is a popular validation case for rotating cavity simulations, having been used for both URANS (Tan et al., 2009, 2014; Tian and Zhu, 2012) and LES (Tan et al., 2009) computations.

The cavity has corotating disks, shroud, and shaft. Bohn et al. (2000) created the disk temperature profile using electrical heaters embedded in aluminium rings so that they supplied an isothermal heat flux to the cavity. The disk heat flux was measured using

thermistors placed on both sides of 5 mm thick epoxy disks positioned between the heaters and cavity. A diagram of the cavity is shown in Fig. 3.1, and the cavity dimensions are given in Tab. 3.1. The upstream and downstream disks are located at $z/s = -0.5$ and $z/s = 0.5$, putting the axial mid-plane at $z/s = 0$.

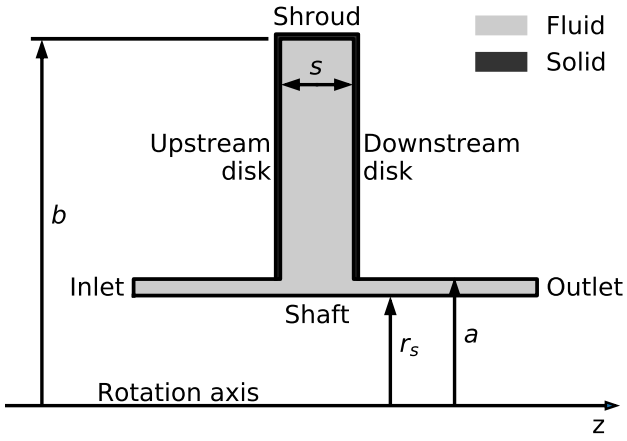

Figure 3.1. Bohn et al. (2000) cavity diagram and nomenclature.

Table 3.1. Bohn et al. (2000) cavity dimensions.

Parameter		**Value [m]**
Shaft radius	r_s	0.12
Cob radius	a	0.138
Shroud radius	b	0.4
Cavity axial width	s	0.08

The range of operating conditions at which Bohn et al. (2000) reported experiment disk temperatures and Nusselt numbers is given in Tab. 3.2. In the experimental rig, the axial through flow was supplied at a temperature of 298.15 K - for $\beta \Delta T_{max} = 0.27$ this would give a nominal maximum temperature in the cavity of 378.15 K.

The Grashof number is two orders of magnitude smaller than what one would find at engine relevant conditions (Owen and Long, 2015), however the Rossby number

Table 3.2. Bohn et al. (2000) experimental rig operating conditions.

Parameter		Min. value	Max. value
Axial Reynolds number	Re_z	3×10^3	1.05×10^4
Rotational Reynolds number	Re_ϕ	2×10^5	8×10^5
Buoyancy parameter	$\beta \Delta T_{max}$	—	0.27
Rossby number	Ro	0.121	0.483
Grashof number	Gr	3.03×10^9	4.86×10^{10}
Angular velocity	Ω	14.17 rad/s	56.67 rad/s

(being proportional to the ratio of the axial and rotational Reynolds number) is broadly inline with engine relevant conditions. Note that Bohn et al. (2000) use a different definition of the axial Reynolds number, given by

$$Re_z^* = \frac{2\rho_{in} V_z a}{\mu_{in}}. \tag{3.1}$$

At $Re_z = 3 \times 10^3$, this alternative definition would give $Re_z^* = 2 \times 10^4$. The definition used in this thesis was chosen to more consistent with recent research on rotating cavities.

3.3 Baseline Computational Methodology

All simulations in this thesis were conducted in the non-inertial frame using the fully compressible pressure based solver in ANSYS Fluent, a popular component of the tooling used in both industrial and academic applications for internal flows and heat transfer.

To avoid the confusion of the effects of modelling fidelity/boundary conditions and numerics, the same numerics were used for all simulations. Pressure and velocity were coupled at each time step using the SIMPLEC algorithm (Van Doormaal and

Raithby, 1984). Unless otherwise stated, face values of velocity and energy were interpolated using a second order upwind scheme; a central scheme was used for pressure and diffusion terms. The governing equations were discretised in time using the second order backwards difference scheme.

Each time step was judged to be converged when the continuity, momentum, and energy residuals had dropped by two orders of magnitude relative to the first iteration of the time-step. In all cases air was modelled as a perfect gas, and a temperature dependent viscosity and thermal conductivity (calculated with Sutherland's law and a Prandtl number of 0.71) were used. A flow chart of the solver process is shown in Fig. 3.2.

In the computational geometry, the inlet and outlet were extended compared to the experimental rig to avoid issues around reversed flow at boundaries. All cases use the same inlet and outlet boundary conditions:

Inlet: The total pressure (with zero swirl) was adjusted to match Re_z and the temperature is set to 298.15 K. No fluctuations were applied to the inlet; it is considered as laminar due to the low value of Re_z.

Outlet: Static pressure set to the rotating cavity operating pressure (calculated on a case-by-case basis to match Re_ϕ and Ω at the inlet.)

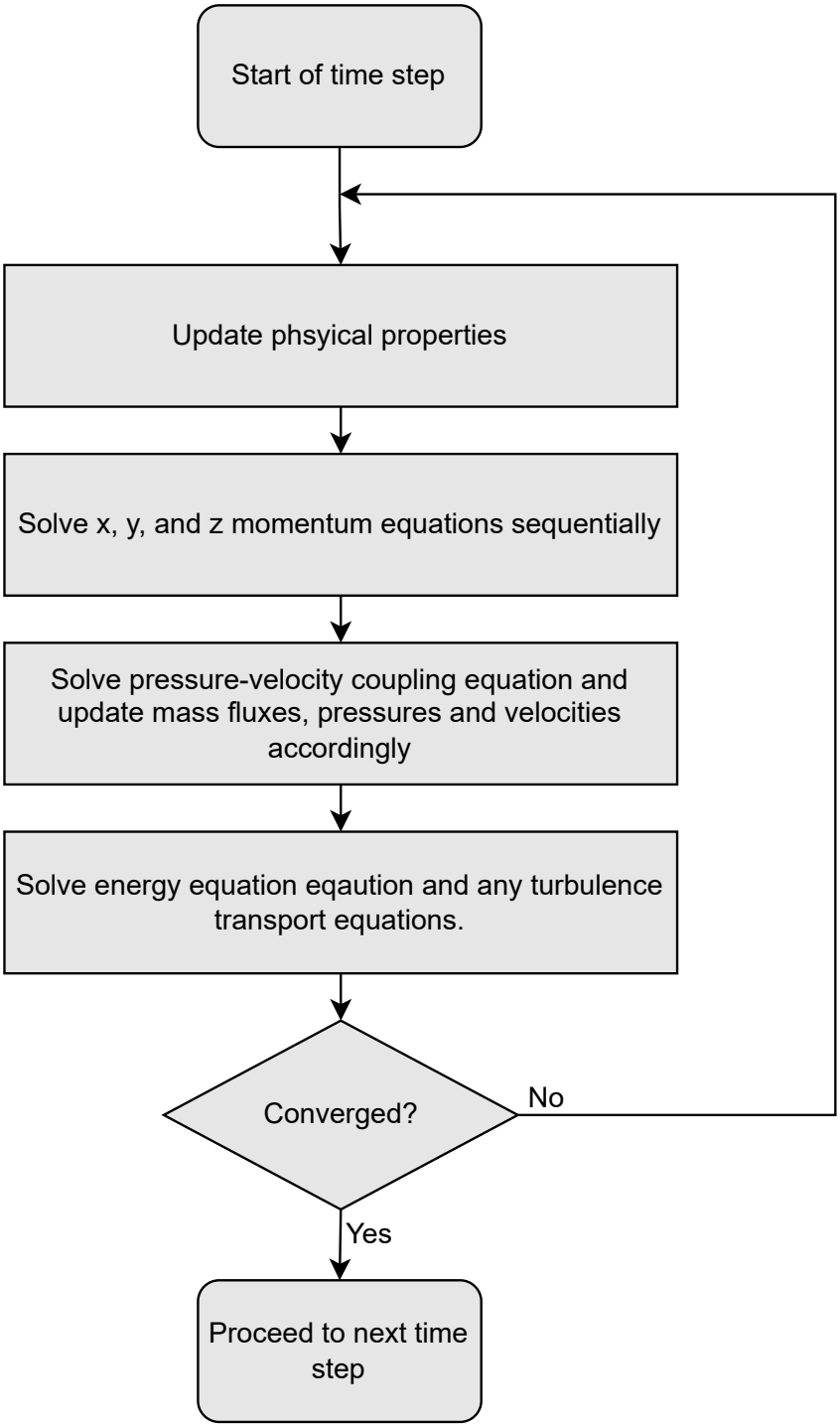

Figure 3.2. ANSYS Fluent compressible pressure based solver solution process.

3.4 Low Grashof Number Computations

3.4.1 Overview of Low Grashof Number Computations

The first computations conducted at the lowest rotational Reynolds number (or equivalently Grashof number) case reported in Bohn et al. (2000). The operating conditions of this case are shown in Tab. 3.3. The disk wall temperatures were set to match the distributions given by Bohn et al. (2000) (Fig. 3.3). The shroud temperature was set to be 353.15 K, in accordance with data in (Bohn and Ren, 2009) - no value for the shroud temperature was given in Bohn et al. (2000) which had an unheated shroud. An adiabatic shroud was not used because the unheated shroud still provides a heat flux to the fluid (due to conduction in the test rig), and the formation of streaks (a flow structure of interest in this paper) is caused by the shroud heat flux Puttock-Brown and Rose (2018); Puttock-Brown et al. (2017). To match experimental conditions as closely as possible, a gravity vector that was fixed in the inertial frame (i.e. rotating at $-\Omega$ in the non-inertial frame) was also included. In the computations of Bohn et al. (2006) this was found to be essential to create the initial instability that developed into the large scale flow structure at this operating condition.

Table 3.3. Low Grashof number operating conditions for the baseline modelling study.

Parameter		**Value**
Axial Reynolds number	Re_z	3×10^3
Rotational Reynolds number	Re_ϕ	2×10^5
Buoyancy parameter	$\beta \Delta T_{max}$	0.27
Rossby number	Ro	0.483
Grashof number	Gr	3.03×10^9
Angular velocity	Ω	$14.17\,\mathrm{rad/s}$

The computations conducted at this operating condition are summarised in Tab. 3.4. Three different modelling fidelities are used: URANS, URANS/LES hybrid, and LES.

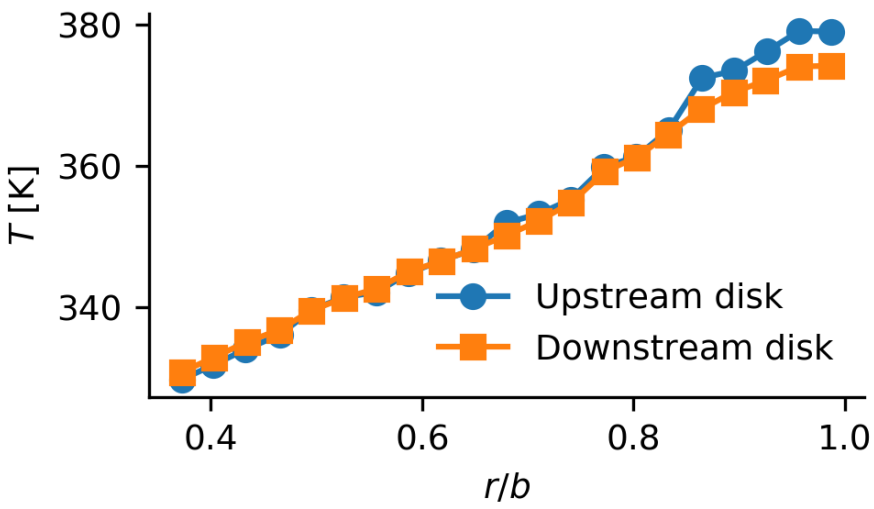

Figure 3.3. Experimental disk temperature profiles from Bohn et al. (2000) for the low Grashof number operating condition.

The models used were the $k-\omega$ SST model (Menter, 1994) for URANS, the wall adapting local eddy viscosity (WALE) sub-grid scale (SGS) model (Nicoud and Ducros, 1999) for LES, and the Shielded-DES (Menter, 2018) for the URANS/LES hybrid model.

Four different meshes were used, with nominal sizes of 1M, 2M, 4M, and 6M cells. The meshes were fully hexahedral and created by meshing the meridional plane in 2D and then rotating the resulting mesh around the z-axis. The 1M cell mesh is shown in Fig. 3.4. URANS computations were carried out on the 1M, 2M, and 4M cell meshes, while DES and LES computations used the 2M, 4M, and 6M cell meshes. Note the inclusion of a 90° bend at the inlet of this case - this was done to better represent the geometry of the cavity, it was verified after the simulation campaign in this section that its inclusion has no impact on the flow structure observed within the cavity, so all subsequent computations in this thesis use the more simple straight inlets as shown in Fig. 3.1.

Table 3.4. Summary of low Grashof number computations for the baseline modelling study.

Turbulence model	Mesh size [cells]			
	1M	2M	4M	6M
URANS	✓	✓	✓	·
DES	·	✓	✓	✓
LES	·	✓	✓	✓

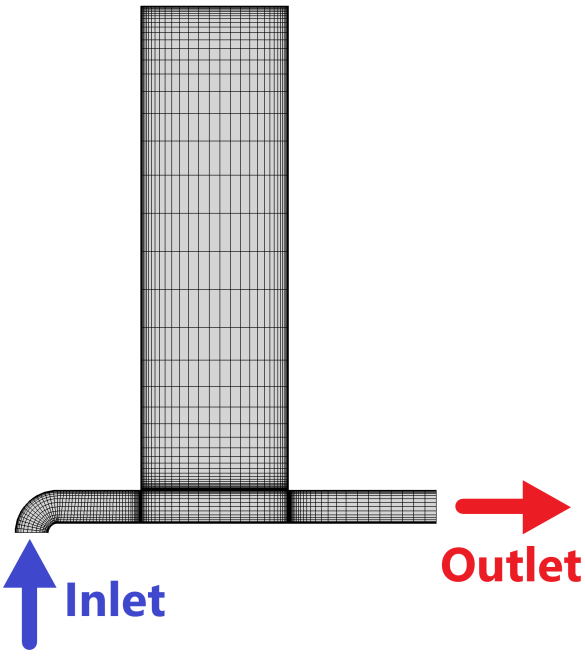

Figure 3.4. Meridional view of the 1M cell mesh used for URANS computations at the low Grashof number operating condition.

For LES and DES, time steps were set to give Courant-Friedrichs-Lewy (CFL) numbers of less than one in the bore. CFL numbers were generally much lower inside the cavity. For the 6M cell mesh, this resulted in 700 time-steps per revolution. URANS solutions used time steps that were four times larger than the LES solutions on the same mesh.

3.4.2 Validation and Verification

Large scale flow structure

The large scale flow structure from the LES simulation on the 6M cell mesh is visible in the temperature contours in Fig. 3.5. It consists of two circulation pairs (marked with arrows) that rotate at approximately 0.925Ω in the inertial frame. The cyclonic circulations are marked with '$-\Delta p$', and the anti-cyclonic circulations with '$+\Delta p$'. The location of the radial arms can clearly be seen by the presence of cold fluid. This flow structure is in agreement with the computations of other authors (e.g. Tan et al. (2009)) on this case, although Bohn et al. (2000) only observed one circulation pair that slips at $0.88 - 0.90\Omega$ in an experimental smoke flow visualisation.

Mesh resolution

The mesh dependencies of the average downstream disk Nu and average Nu_{sh} are shown in Fig. 3.6 for URANS, DES, and LES. On the disk, all three modelling fidelities are converging to mesh independent values, as expected. The picture on the shroud is less clear - there is no convergence of Nu_{sh}, although the size of the mesh dependency is small. It may be that a finer mesh is needed in this area; this is investigated later on in the paper.

To further verify the turbulence resolving simulations, the power spectra of the turbulent kinetic energy (TKE) was calculated at the mid-radial, mid-axial position

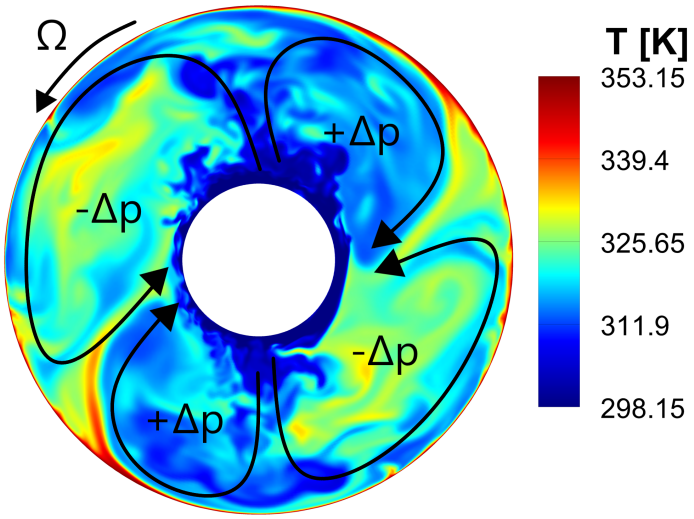

Figure 3.5. Mid-plane temperature distribution and large scale flow structure. (Low Grashof number condition, 6M cell LES.)

$(r/b = 0.6725, z/s = 0)$ in the cavity. The power spectral density (PSD) of the TKE was calculated as

$$\mathrm{PSD}\,(\mathrm{TKE}) = \left[\mathrm{PSD}\left(u'\right) + \mathrm{PSD}\left(v'\right) + \mathrm{PSD}\left(w'\right)\right]/2, \tag{3.2}$$

where the PSD of each Cartesian velocity component was calculating using Welch's method (using a Hann window, three segments, and 50% overlap) to reduce finite sampling effects. The results are shown in Fig. 3.7: a -5/3 inertial range is present in each spectra until approximately 25 Hz, indicating that the dynamics of the turbulent flow are appropriately resolved. This is even the case for URANS up until 6 Hz, indicating that it is resolving some chaotic turbulent fluctuations that should already be accounted for by the RANS model. LES and DES behave equally well in the bulk flow, as expected. Interestingly, at low frequencies, URANS is not far away from LES. Similar results were observed for the 4M and 2M cell simulations, with the 4M cell mesh giving an identical spectra to the 6M cell mesh with LES.

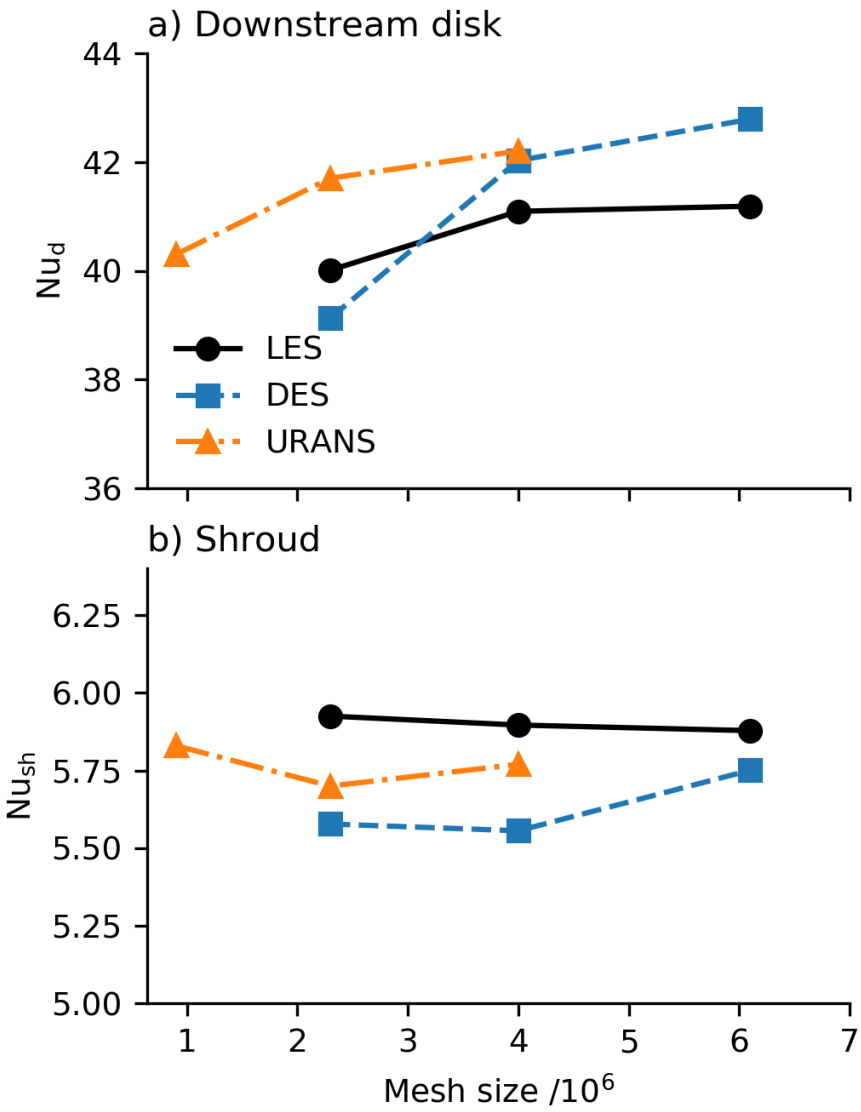

Figure 3.6. Average Nusselt number mesh sensitivity for URANS, DES, and LES at the low Grashof number operating condition.

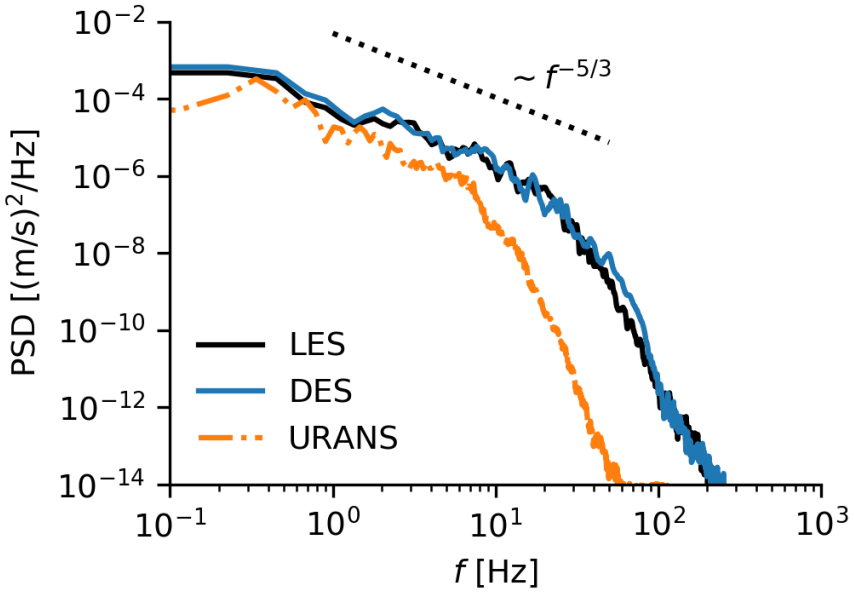

Figure 3.7. TKE power spectra at mid-cavity at the low Grashof number condition. (LES and DES use a 6M cell mesh, and URANS uses a 4M cell mesh.)

The wall spacings used are suitable for wall-resolved LES by the classical boundary layer requirements Sagaut (2006) - the average axial, radial, and tangential mesh spacings on the 6M cell mesh are $\Delta r^+ = 21$, $\Delta(r\phi)^+ = 27$, and $z^+ = 0.28$ on the downstream disk, and $r^+ = 0.22$, $\Delta(r\phi)^+ = 25$, and $\Delta z^+ = 5.2$ on the shroud.

Comparison to experimental data

Figure 3.8 shows a comparison of the computational and experimental time-and-circumferential average *Nu* on the upstream and downstream disks of the cavity. The temperatures used to calculate *Nu* are shown in Fig. 3.3. The computations reported are on the largest mesh used for each modelling fidelity (4M mesh for URANS, and the 6M cell mesh for DES and LES).

The agreement with the experimental data is reasonable; on the upstream disk there is a close correspondence between the experimental and computational heat transfer for all modelling fidelities. On the downstream disk, the agreement is less good. At

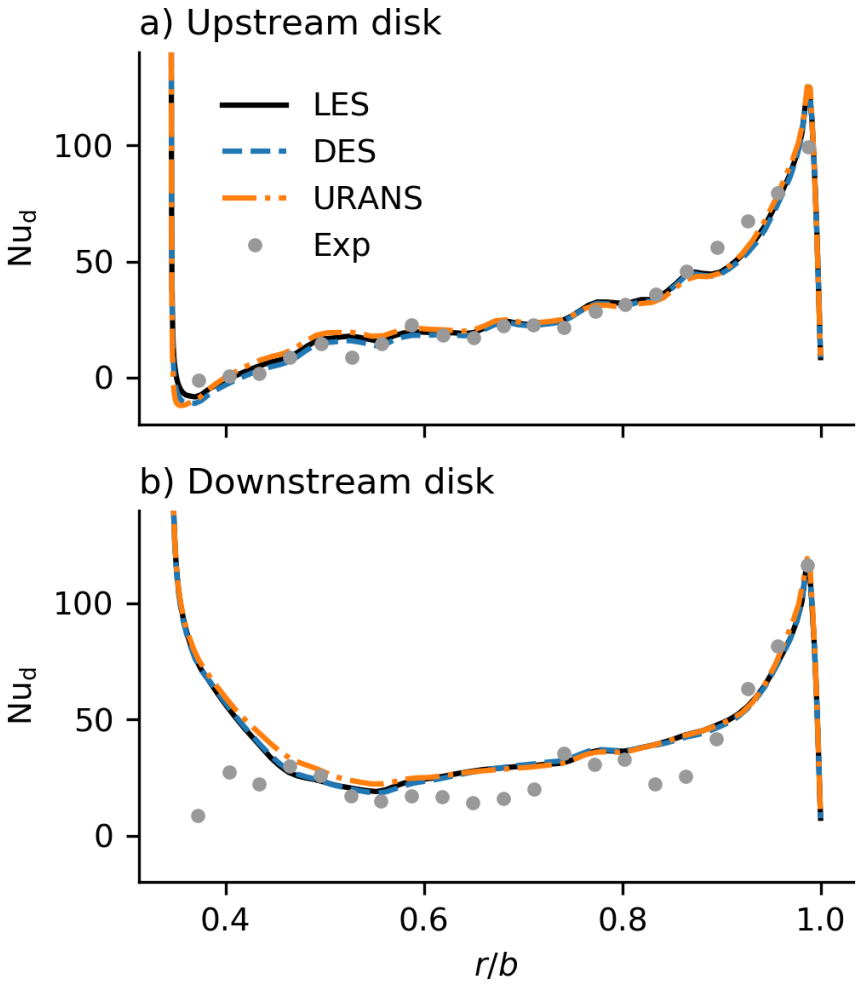

Figure 3.8. Disk Nusselt number distributions at the low Grashof number condition. Experimental data from Bohn et al. (2000). (LES and DES use a 6M cell mesh, and URANS uses a 4M cell mesh.)

very low radii ($r/b < 0.5$) there is a significant over-prediction in Nu present in all simulations - this phenomena was observed to be completely mesh independent and due to the impingement of the cold axial throughflow upon the heated disk. This is a feature of most other computations on this test case Tan et al. (2009, 2014); Tian and Zhu (2012). In Tian and Zhu (2012), the magnitude of the over-prediction was found to reduce with the inclusion of conjugate heat transfer (CHT). At higher radii on the downstream disk the heat flux is still over-predicted.

3.4.3 Near-Disk Flow

The computed disk heat transfer has little dependence on the modelling fidelity (demonstrated in Figs. 3.6 and 3.8). This is because of the nature of the laminar nature of the disk near-wall layers - no structures consistent with Ekman layer transition (for an example of these in a cavity with radial inflow, see Onori et al. (2016)) were observed in the LES solutions. Although near-disk unsteadiness was observed in our computations, this was driven by external unsteadiness and was parallel to the disk, and not generated by local near-wall layer instabilities that create heat transfer enhancing wall-normal transport of fluid.

The TKE at the mid-radial location is plotted against the distance from the upstream disk (Δz) in Fig. 3.9a. The lack of strong peak is evidence for the laminar nature of the near-disk layer: in a turbulent boundary layer, a peak in the TKE distribution due to turbulent production is expected within the buffer layer ($5 < y^+ < 30$). The peak location of TKE occurs at $\Delta z = 2.87\,\text{mm}$, or $z^+ = 18.0$. The very shallow TKE peak in Fig. 3.9a thus implies that, within the near-disk layer, the production of TKE is very low, whereas its dissipation by viscous effects is still clearly appreciable, as shown by the TKE dropping to zero at the wall. This behaviour is consistent with a laminar Ekman layer driven by external unsteadiness.

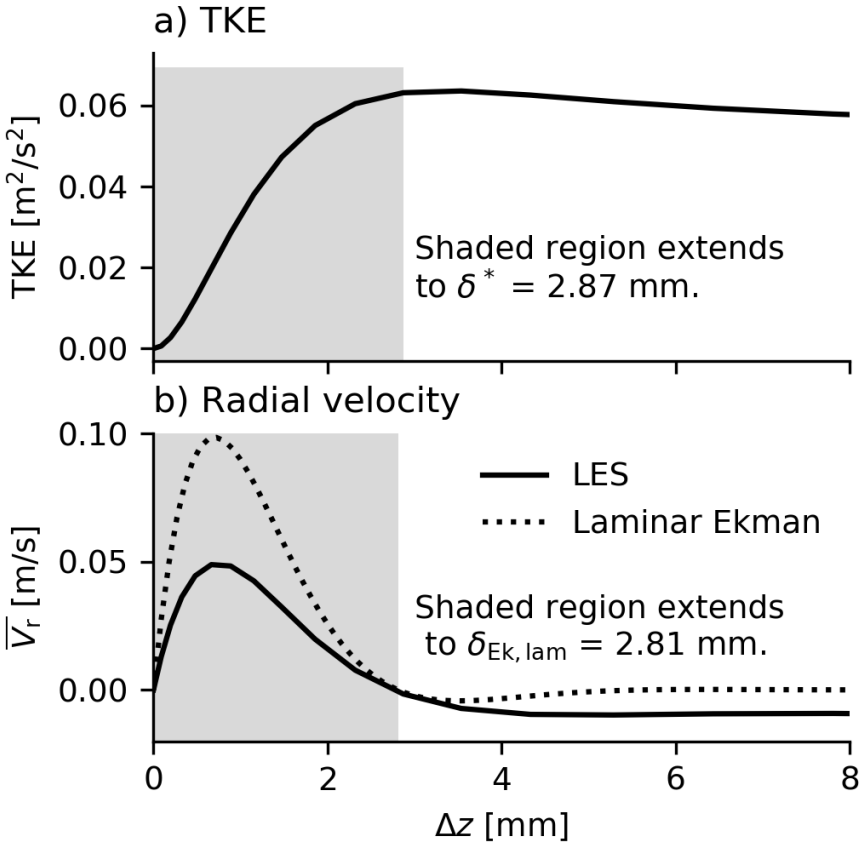

Figure 3.9. Near-disk time-mean radial velocity profile and turbulent kinetic energy at mid-radius on the upstream disk at the low Grashof number condition.

The theoretical linear laminar Ekman layer thickness can be estimated as

$$\delta_{Ek,lam} = \pi b / \sqrt{Re_\phi} = 2.81\,\text{mm}, \tag{3.3}$$

this is the location of the first zero crossing point of a laminar Ekman layer, whose velocity is given by

$$V_r = -V_{\phi,core} \exp\left(\frac{-\pi \Delta z}{\delta_{Ek}}\right) \sin\left(\frac{\pi \Delta z}{\delta_{Ek}}\right), \tag{3.4}$$

where $V_{\phi,\text{core}}$ is the relative tangential velocity of the fluid away from the disks (Childs, 2011). The radial velocity profile is plotted in Fig. 3.9b. Despite the different magnitudes of the peak radial velocity, the computational near-wall layer behaves in a similar way to the theoretical laminar Ekman layer - the peaks are in the same location, and the zero-crossing points are almost identical.

By assuming a Blasius 1/7$^{\text{th}}$ power law profile (Childs, 2011), the turbulent Ekman layer thickness can also be estimated as

$$\delta_{Ek,turb} = 0.0983\, b \sqrt{Re_\phi} \left(\frac{|V_{\phi,\text{core}}|}{\Omega b}\right)^{0.6} = 0.58\,\text{mm}. \tag{3.5}$$

Taking a similar approach as Pitz et al. (2019a,b), and using the location of peak TKE, δ^*, as the upper limit of the disk near-wall layer, we find that the near-wall layer thickness is more consistent with the thickness predicted by laminar Ekman layer theory and over four times thicker than the turbulent theory. These results are tabulated for the upstream disk of the cavity at the mid-radial position in Tab. 3.5.

These results explain the reasonable predictions in the literature with URANS - as the disk near-wall layers are laminar, there are no potentially heat transfer enhancing

Table 3.5. Computed and theoretical upstream disk near-wall layer thickness at the mid-radial location. (low Grashof number condition.)

Case	δ^* or δ_{Ek} [mm]
LES δ^*	2.87
DES δ^*	2.87
URANS δ^*	3.22
Laminar δ_{Ek}	2.81
Turbulent δ_{Ek}	0.58

vortical structures to resolve or model within them. Thus, as long as the behaviour of the off-wall flow is captured accurately, URANS or URANS/LES hybrid approaches should be suitable when the Grashof number is low enough to avoid transition or the presence of significant modelled turbulence within the disk Ekman layer.

3.4.4 The Effect of Disk Thermal Boundary Condition

To assess the effect of the disk thermal boundary condition, extra LES simulations were conducted on the 2M and 6M cell mesh. These simulations were conducted using two types of boundary conditions - the first case uses heated isothermal disks as in the previous simulations in this paper. In the second case, the disks were both set to be adiabatic, and the shroud temperature was adjusted so that the difference between the maximum disk temperature and the throughflow was the same as in the baseline heated disk case. Both of these cases have the exact same description in terms of non-dimensional variables as given in Tab. 3.3 - this means that any differences in aerodynamics are due to the local heating effects within the cavity. In contrast to the rest of this thesis, the simulations in this section used a bounded central differencing discretization for all variables.

The global flow structure with adiabatic disks is unchanged from the isothermal disk

case, with two circulation pairs forming in both simulations although the temperature and relative extent of the cyclonic and anti-cyclonic circulations has changed (see Fig. 3.10). Despite the similarity in the large-scale flows structure between the two cases, the disk thermal boundary condition has a significant effect on the evolution of the disk temperatures and the aerodynamic characteristics of the near-wall flow.

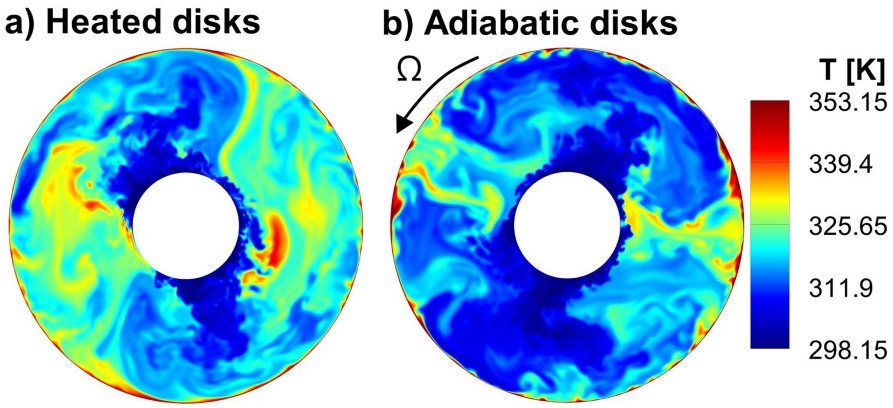

Figure 3.10. Mid-plane temperatures from 6M cell LES with isothermal and adiabatic disks at the low Grashof number condition.

The mean temperature distributions that develop on the adiabatic and isothermal downstream disks are shown in Fig. 3.11. The temperature distribution that develops on the adiabatic disks is very different to the temperature imposed on its isothermal counterpart to match the data of Bohn et al. (2000).

Figure 3.12 shows the mean radial shear stress for both disk boundary conditions for simulations conducted on the 6M cell mesh. When an isothermal boundary condition is used for the disks, the buoyancy forces from the positive radial temperature gradient in the near-wall fluid drives a near-wall radial inflow above $r/b \approx 0.8$. In contrast, for the adiabatic disks, the near-wall temperature gradient is governed by aerodynamic interactions between the flow in the cavity and the disk, and any near-wall radial inflow occurs at a higher radius ($r/b > 0.9$) and is of a much smaller velocity. This phenomena is mesh independent, with very close agreement in the values of the

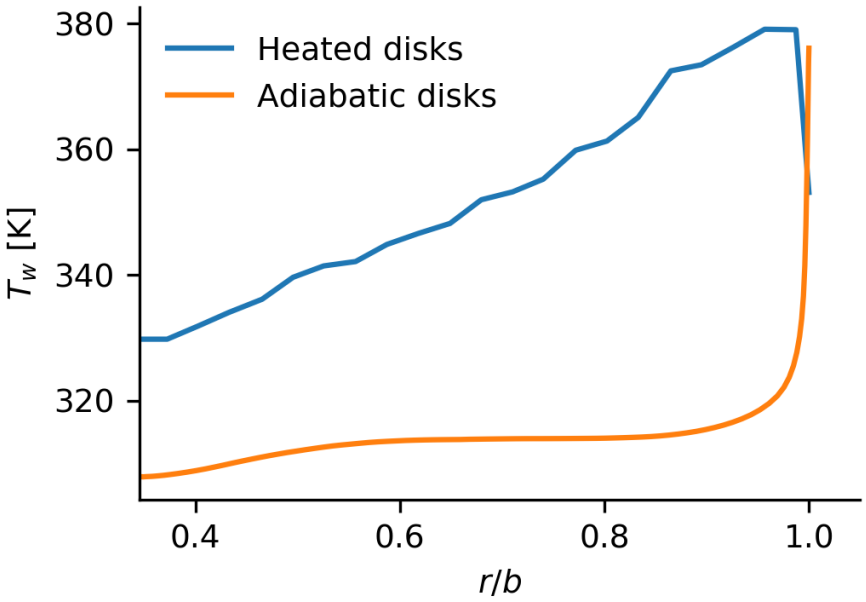

Figure 3.11. Comparison of fluid wall temperatures on the downstream disk at the low Grashof number condition.

shear stress on the 2M and 6M cell meshes.

The meridional velocity streamlines in Fig. 3.13 also show this effect. The location of the reversal in near-disk flow is marked with 'Rev.'; this occurs at locations corresponding to the reversal of the radial disk shear-stress in Fig. 3.12.

This difference in behaviour of the near wall is caused by the local buoyancy forces generated by the wall: when the wall is isothermal, the wall radial temperature gradient generates a radially inward buoyancy force. When the disks are adiabatic, most of the disk has a very small radial temperature gradient (see Fig. 3.11), meaning that there is a comparatively small buoyancy force, and that the behaviour of the near-wall flow is governed only by the flow structures in the flow away from the disk.

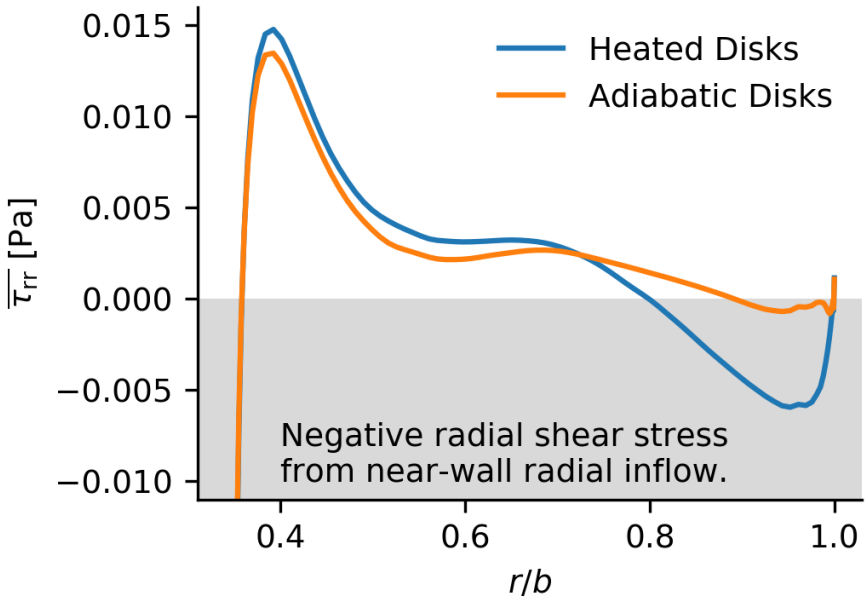

Figure 3.12. Average radial shear stresses on downstream disk with different disk thermal boundary conditions at low Grashof number.

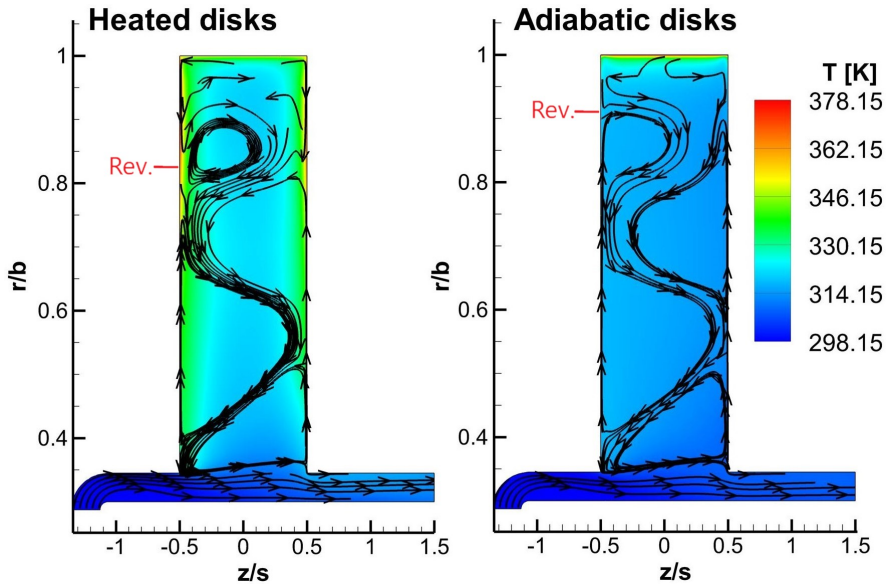

Figure 3.13. Time-average temperature and meridional velocity streamlines showing the effect of disk heating on the cavity flow structure.

3.4.5 Near-Shroud Flow

Shroud streaks

Although shroud streaks have been observed at engine relevant Grashof numbers in URANS simulations (Puttock-Brown and Rose, 2018; Puttock-Brown et al., 2017), to the authors' knowledge they have not previously featured in papers that use higher fidelity methods such as LES at any Grashof number. Both LES and DES capture streaks - their existence can be seen in the Nu_{sh} contours in Fig. 3.14 (along with the radial velocity on the cavity mid-plane), where they occur in cyclonic circulations, in accordance with the observations of Puttock-Brown and Rose (2018); Puttock-Brown et al. (2017). Despite streaks only being captured in the present LES and DES (Fig. 3.14a, b), all three simulation methods give similar values for Nu_{sh}, with LES giving a heat flux that is approximately 2% higher than both DES and URANS (Fig. 3.6b). Investigating what mesh resolutions and modelling fidelities are appropriate for capturing these streaks is the focus of the rest of this section.

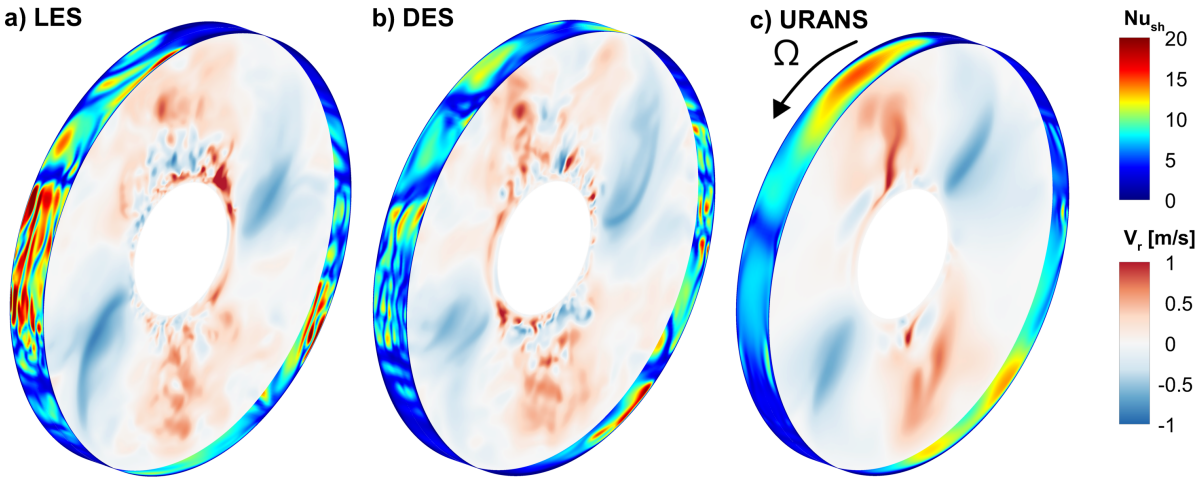

Figure 3.14. Contours of shroud Nusselt number and mid-plane radial velocities from different turbulence modelling fidelities at the low Grashof number condition.

Streak length scales

The mesh on the shroud easily meets classical LES mesh requirements for a channel flow simulation. The average span-wise spacing is $\Delta z^+ = 5.2$, and the average wall-normal spacing is $r^+ = 0.22$. The radial extent of the streaks is quite consistent across the simulations too - their core is at $r^+ \approx 15 - 20$, and they extend out to $r^+ \approx 30 - 40$. However, a significant feature of Fig. 3.6b is that the shroud heat transfer does not converge as the mesh is refined. This mesh dependency is unexpected given that the near-wall meshes meet the usual requirements.

Investigating the span-wise extent of the streaks in the *rz*-plane yields some explanation. The distribution of the tangential vorticity, ω_ϕ, from the LES simulation is shown in Fig. 3.15. The figure shows the cavity in the near shroud region. The region shown in this figure roughly corresponds to $0 < r^+ < 63$.

The vorticity of each streak is concentrated to within 1-3 cells width. This is hardly enough cells to reliably resolve an important flow structure. For mesh convergence, the streaks should be better resolved by, for example, at least 10 cells as suggested by Sagaut (2006).

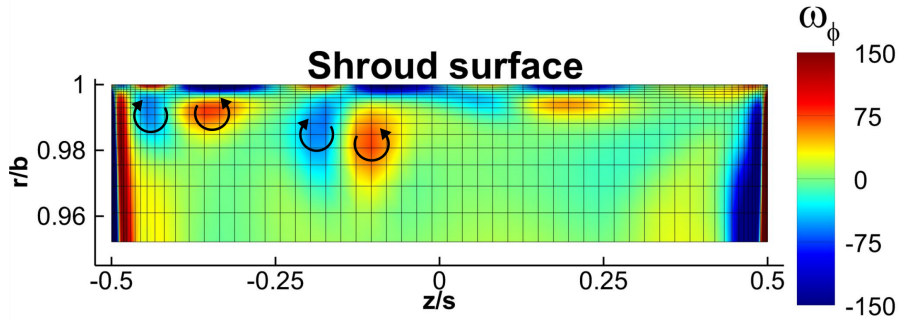

Figure 3.15. Streak tangential vorticity and mesh resolution at the low Grashof number condition. Vortex rotation indicated by arrows.

Modelling fidelity effects

The URANS solution in Fig. 3.14c does not predict the formation of any streaks until close to the end of the cyclonic region - there are weak streaks that raise the local Nu_{sh} to about 7 just before the cyclonic flow separates from the shroud to flow radially inwards. In contrast, the streaks in the LES and DES computations in Fig. 3.14a and b raise the local Nu_{sh} to about 20 in some regions and start adjacent to where the radial outflow meets the shroud.

The question is that, as URANS does not predict streaks, why does it give similar heat transfer to DES and LES? We see that this is because in the URANS solution, the radial arm (positive radial velocity) does not breakdown into smaller structures to the same extent as LES or DES. This means it enhances heat transfer by impinging upon the shroud as a coherent structure. This is visible in the large region of enhanced heat transfer at the top of Fig. 3.14c. The other simulations capture the breakdown of the radial arm into smaller structures, leading to a more diffuse radial arm, which in turn creates a much less significant heat transfer enhancement from impingement on the shroud. Although URANS gives a similar shroud heat flux to LES, it does so for the wrong reasons.

It is interesting that there are streaks in the DES results in Fig. 3.14b given that it uses URANS in near-wall regions. This is because in the near-wall region, the URANS layer in the DES returns negligible turbulent viscosity. Hence the URANS layer behaves as a LES with no SGS model, allowing the streaks to form, and not suppressing them in the same manner as the pure URANS computations. The reason for this difference in behaviour of URANS and DES (note both use the $k-\omega$ SST model in this region) is the vastly different turbulent viscosities predicted by the models.

Figure 3.16 shows the near-shroud turbulent viscosity ratio (TVR) in a cyclonic region

where streaks have been captured by DES. The TVR is calculated by the ratio of eddy viscosity to the dynamic viscosity, or μ_t/μ. The TVR returned by DES is significantly lower than URANS, even within the URANS region of the URANS/LES hybrid. Note that the scale for DES in Fig. 3.16a is an order of magnitude smaller than that for URANS in Fig. 3.16b.

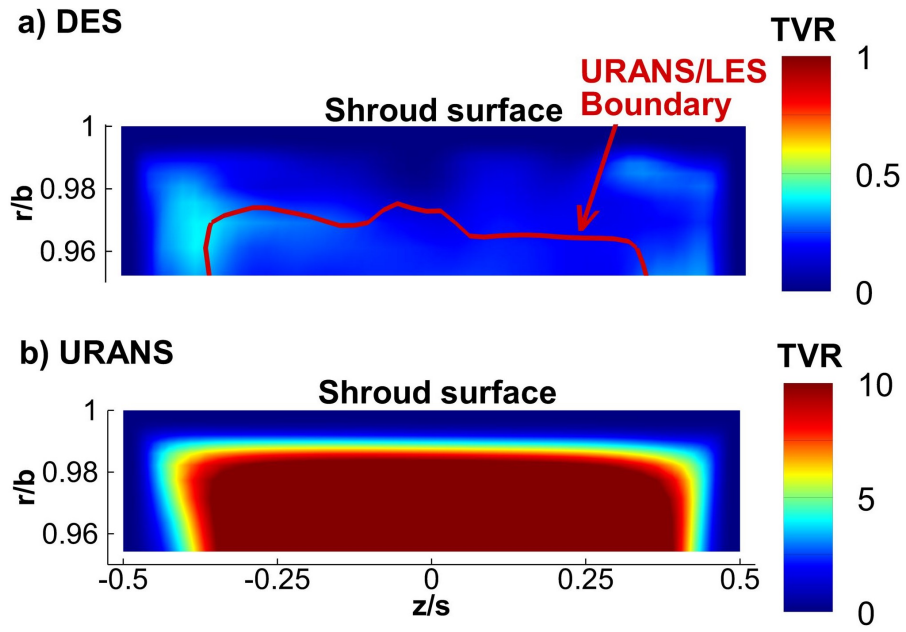

Figure 3.16. Near-shroud TVR (μ_t/μ) distributions in the cyclonic circulation at the low Grashof number condition.

For this particular case, there is no benefit in terms of mesh requirements to using DES over LES, as the flow structures near the wall are captured by the present DES. This does, however, ignore the fact that when not explicitly comparing the models, one would use a much coarser near-wall mesh with DES than LES.

Whilst the DES model in this section performed similarly to LES, its behaviour was inconsistent with being a hybrid URANS/LES model. Whether DES will still behave this way at higher Grashof numbers is unclear and is investigated in the next section.

3.5 Higher Grashof Number Computations

3.5.1 Overview of Higher Reynolds Number Computations

The results in the previous section indicate that there may be an issue with the use of DES: both the laminar near-wall layers on the disk (Fig. 3.9) and the near-shroud streaks (Figs. 3.14, 3.16) occur within the RANS region of the DES model. At a low Grashof number this was mitigated by the DES returning a negligible turbulent viscosity near the wall, thus behaving in a similar manner to LES in all regions of the flow.

To investigate whether this will be the case at higher Reynolds or Grashof numbers, extra simulations were conducted using LES and DES on the same cavity at ten times the rotational speed of the low Grashof number condition, resulting in rotational Reynolds number of 2×10^6 and a Grashof number of 3.03×10^{11} - a 100-fold increase in Gr from the previous condition, and almost at engine relevant levels ($Re_\phi \sim 10^6$ and $Gr \sim 10^{12}$ (Owen and Long, 2015)). The axial Reynolds number was not changed.

These simulations had an imposed disk temperature that varied linearly from 330.15 K at the minimum radii of the disk to 378.15 K at the maximum radii of the disk, and the shroud temperature was set to be 378.15 K. The maximum temperature of the shroud and disks was chosen to maintain the same buoyancy parameter ($\beta \Delta T_{max}$) as the lower Grashof number case discussed previously. A full list of non-dimensional parameters describing this case is given in Tab. 3.6.

The solver set-up was identical to that used for the previous simulations in this paper, expect that the Smagorinsky-Lilly SGS model was used for LES, and the Delayed-DES formulation was used for the URANS/LES hybrid

Table 3.6. High Grashof number operating conditions for the baseline modelling study.

Parameter		**Value**
Axial Reynolds number	Re_z	3×10^3
Rotational Reynolds number	Re_ϕ	2×10^6
Buoyancy parameter	$\beta \Delta T_{max}$	0.27
Rossby number	Ro	0.0483
Grashof number	Gr	3.03×10^{11}
Angular velocity	Ω	$141.7\,\mathrm{rad/s}$

computation (Gritskevich et al., 2012). The cavity was re-meshed to give an appropriate boundary layer mesh sizing for the new flow condition, resulting in a mesh of 6M cells. All solutions were initialised from a coarse mesh laminar solution and ran for 40 revolutions to remove initial transients, before statistics were sampled for 20 revolutions. For the baseline 6M cell computations, 360 time-steps per revolution were used. To confirm the mesh and time-step independence of the conclusions made in this section, the LES computation was repeated on the 6M mesh with 720 steps per revolution and also with a 10M cell mesh again using 360 time-steps per revolution. These computations are summarised in Tab. 3.7. A case on the 10M cell mesh with 720 time-steps per revolution was not run because minimal changes due to time-step size were observed on the 6M cell mesh. The reason for this is likely that the limiting factor on how large a time-step can be (which limited the choice for 360 time-steps per revolution) is the in the axial throughflow. Due to the different mesh sizes and velocities, a reasonable CFL in the throughflow results in a very small (well below one) CFL number in the bulk of the cavity, even in the 360 time-steps per revolution case.

Table 3.7. Summary of high Grashof number computations for the baseline modelling study.

Turbulence model	Mesh size [cells]		
	6M	6M ($0.5\Delta t$)	10M
DES	✓	·	·
LES	✓	✓	✓

3.5.2 Modelling Fidelity Effects

As expected, both LES and DES gave the same large-scale flow structure, which consisted of three circulation pairs. This is visible in the radial velocity distributions in Fig. 3.17.

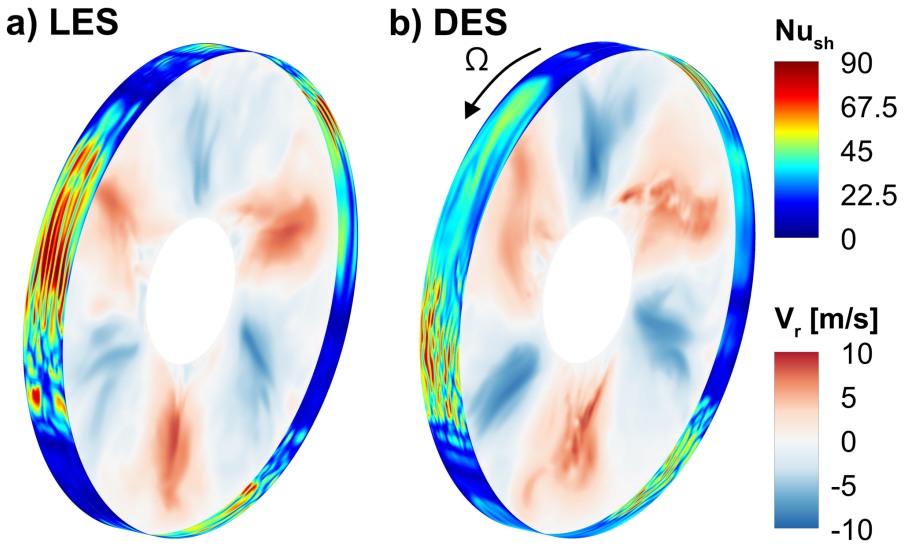

Figure 3.17. Shroud Nusselt number and mid-plane radial velocity at the high Grashof number condition.

Despite the large scale similarities in the flow structure, the heat transfer predicted by the two modelling fidelities is quite different - this is shown in Fig. 3.18. Compared to LES, DES under-predicts the shroud heat transfer by 13.5%, but over-predicts the heat flux through the disk by 14.8%. This inconsistency is still present when compared to LES computations using smaller time steps or a larger number of cells.

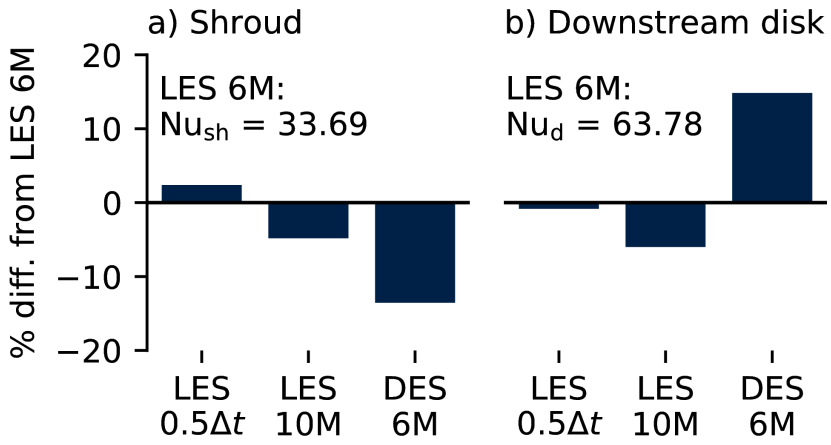

Figure 3.18. Comparison of average disk Nusselt numbers at the high Grashof number condition.

Figure 3.18 helps explain the disparity in the shroud heat transfer calculated by the two modelling fidelities. In the LES (Fig. 3.18a), there are near-shroud streaks covering a large portion of the cyclonic circulation, causing a heavily enhanced heat transfer in that region. In contrast, the DES (Fig. 3.18b) has a region of slightly elevated heat transfer early on in the cyclonic circulation, followed by a region of weak streaks towards the end of the circulation. This difference in behaviour is due to the influence of the higher TVR predicted by DES in the near-shroud region (Fig. 3.19). The RANS branch of the DES in this region is producing enough near-shroud turbulent viscosity to delay the formation of streaks, whilst simultaneously not enhancing the near-shroud heat transfer enough to effectively model the impact of the streaks.

The level of eddy viscosity in Fig. 3.19a is in line with what one would expect from a LES simulation. The distribution of eddy viscosity in Fig. 3.19b is indicative of a larger issue with the use of DES for these types of flows. It is clear from this figure that the behaviour of DES is inconsistent with its expected behaviour: the elevated eddy viscosity is not restricted to the near-wall regions, and instead covers the entire domain, where the value of the TVR should be similar to that in Fig. 3.19a.

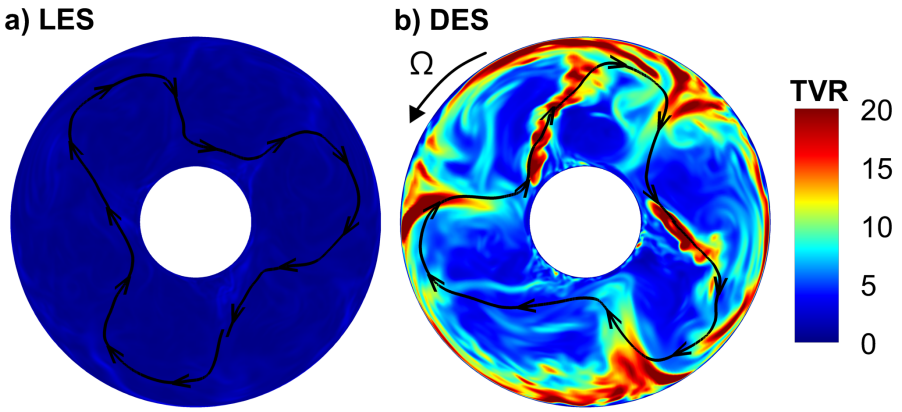

Figure 3.19. Mid-plane Turbulent viscosity ratio (μ_t/μ) and relative velocity streamlines at the high Grashof number condition.

The over-prediction of the disk heat transfer can be explained by examining the wall-normal velocity fluctuations near the downstream disk, as shown in Fig. 3.20. The wall-normal velocity fluctuations are of particular interest as they are responsible for transporting unheated fluid from mid-cavity to the disks. Figure 3.20 includes the resolved velocity fluctuations from both the LES and the DES, as well as the velocity fluctuations modelled by the DES. It can be seen that DES and LES resolve similar amounts of unsteady transport fluid to and from the wall; however, the DES also models a significant amount of wall-normal velocity fluctuation, creating an unphysical enhancement of the wall heat flux. This double accounting of velocity fluctuations is an issue that is known to affect URANS, so it is not surprising to see it here.

The distribution of the wall-normal LES velocity fluctuation in Fig. 3.20 is indicative of a laminar near-wall layer. As with Fig 3.9a for the low Grashof number case, there is no peak, indicating that the near-wall shear is not generating the sort of small-scale unsteady flow layer structures that transport off-wall fluid to and from the wall.

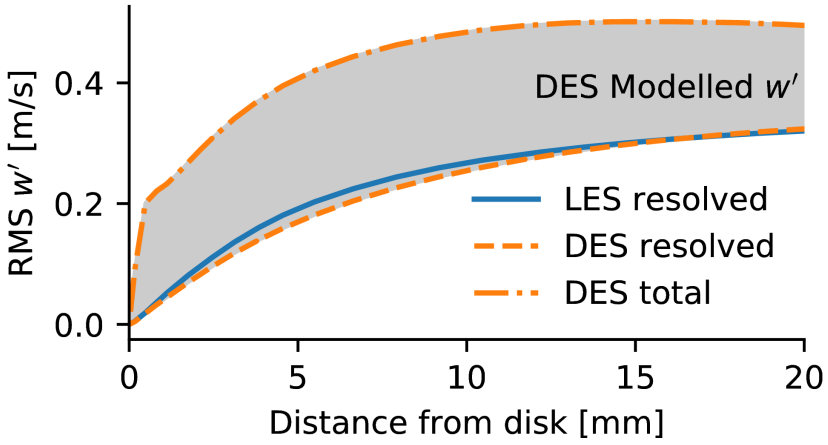

Figure 3.20. RMS of wall normal velocity fluctuations (w') from LES and DES near the downstream disk at the mid-radial location. (High Grashof number case.)

3.6 Further Discussion on Modelling Fidelity

3.6.1 Detached Eddy Simulation

DES relies on the existence of a flow-regime gap where the near-wall and bulk fluid have distinct behaviour and are reasonably separate. The near-wall RANS behaviour of DES is made to collapse to LES behaviour in the bulk flow by enhancing the destruction of eddy viscosity away from the wall. In this flow, the eddy viscosity is injected from the shroud into the bulk flow by radial inflow (shown by the streamlines in Fig. 3.19b). Thus, the eddy viscosity is advected to a region where it physically should not be. It is worth noting that this non-physical transport of eddy viscosity has also been observed in URANS simulations of HP turbines by Yao and He (2020). The presence of the elevated eddy viscosity in the bulk flow is concerning. It means that the double counting of the unsteady flow is not just restricted to the near-wall layers as shown in Fig. 3.20, but affects the entire domain.

It is possible that alternative URANS/LES blending functions would reduce this issue

by increasing the destruction of the eddy viscosity in LES regions. However, this addresses the symptom rather than the actual problem, so it would be impossible to know *a priori* whether a particular simulation would be free from it. As it stands in the current DES simulation, the "grey area" where both URANS and LES are present covers the whole cavity. Even if, with an appropriate blending function, the URANS domain could be restricted to near-wall regions, the behaviour that a CFD user can expect from the simulation is still unclear. This is due to the presence of important heat transfer enhancing structures (streaks) at a similar wall distance to the URANS/LES switch, as shown in Fig. 3.16.

Whilst from these results it is clear that caution is needed when employing DES to research rotating cavities, it is also worth noting that these results may also have implications for future developments of wall-modelled LES. As transport equations of some type are necessary to take into account the effects of boundary layer history (precluding a local wall-model), care will need to be taken to ensure that the effects of any new wall-model are restricted to the wall.

The radial inflow that injected the locally generated modelled turbulence into the bulk flow is a characteristic feature of rotating cavity flows, and indicates that caution is necessary when simulating rotating cavity flows with wall modelling approaches that do not enforce a strong separation between their modelled and resolved regions. This has wider implications for any study that seeks to use hybrid URANS/LES approaches such as DES for heat transfer in internal flows. Wall normal transport is a common feature, be it due to large-scale flow structures, impingement, or film cooling. The results in this chapter show that using DES in such flows introduces considerable addition uncertainties to point where the cost/benefit ratio of using DES over lower fidelity approaches may become unfavourable due to marginal benefits and higher

computational cost.

3.6.2 The Case for Conjugate Heat Transfer

In the literature, there has been little consideration on what fidelity of thermal boundary condition is suitable to properly capture the dynamics of rotating cavity flows. Most simulations use isothermal boundary conditions (i.e. the temperature on each boundary face does not change throughout the computation) to match time-mean experimental data. To the authors' knowledge the only simulation where high fidelity thermal boundary conditions that account for the feedback between the fluid and solid domain (i.e. conjugate heat transfer) have been used was by Tian and Zhu (2012), who found a significant reduction in disk Nusselt number at low radii but did not report any changes in the cavity flow structure.

If the aerodynamics within the cavity influenced the disk heat transfer in a one-way coupling (i.e. the disk shear stress was independent of the thermal boundary condition), isothermal simulations would - with correct boundary conditions - be sufficient to capture the cavity aerodynamics. However, the results in this section are indicative of a two-way relationship, where the aerodynamics influence the disk heat transfer, which also feeds back into the aerodynamics. As there is this two-way relationship, it is likely that it will be necessary to capture the interaction of the fluid and solid domain in a conjugate heat transfer (CHT) computation to properly reproduce the cavity aerodynamics.

The large scale flow structure of rotating cavities presents some interesting challenges from a CHT standpoint, not least because the results in this chapter indicate that it would be necessary to carry out LES-CHT, which leads to several issue around time and length scale disparities (discussed in the next chapter of this thesis).

Figure 3.21 shows the temperature spectra at a point on the mid-radial position 1.25 mm from the downstream disk. The dominant harmonic (amplitude 4 K) in this spectrum is at a very low frequency; its location at $f_0 = 0.34$ Hz implies that the slip ratio of the flow structure relative to the cavity is

$$\frac{\Omega_{\text{core}}}{\Omega} = 1 - \frac{1}{N_{RA}} \left(\frac{2\pi f_0}{\Omega} \right)_{\text{peak}} = 0.925 \tag{3.6}$$

where N_{RA}, the number of radial arms, is two. When calculating the slip ratio directly from the average tangential velocity in the simulation, one finds that $\Omega_{\text{core}}/\Omega = 0.923$ - the dominant harmonic is due to the slip of the large-scale flow structure.

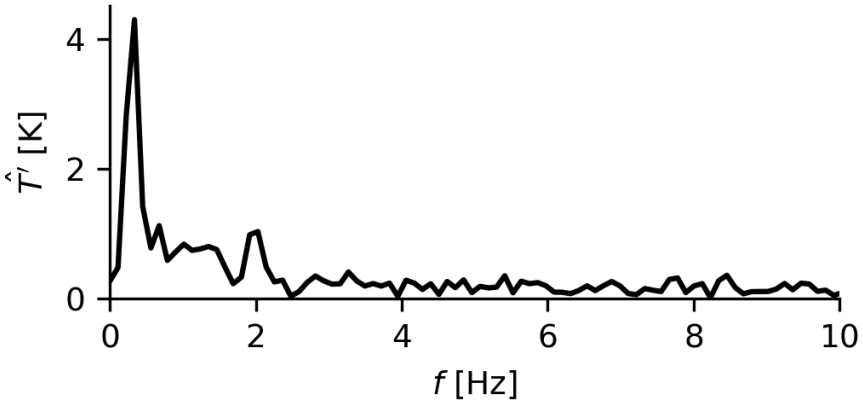

Figure 3.21. Temperature spectrum adjacent to the downstream disk from the 6M LES computation at the low Grashof number condition.

This low frequency coherent temperature fluctuation leads to additional considerations for carrying out accurate CHT on rotating cavities. When the cavity disks are manufactured from a large thermal diffusivity material, such as nickel (see Tab. A.1) it can penetrate through the disk and interact with thermal boundary conditions (or even an adjacent cavity) on the other side. When the disks are manufactured form a low thermal diffusivity material (as in the experimental test rig of Bohn et al. (2000)), the low frequency means that the wall temperature fluctuations on the disk fluid-solid

interface could be on the same order of magnitude as the fluid temperature fluctuations, potentially affecting the cavity aerodynamics. Even if the low frequency temperature fluctuations are not dynamically relevant if properly predicted, it is shown in the next chapter that they may lead to large errors if not handled consistently.

3.7 Implications for Simulating Rotating Cavities

This chapter has presented numerical simulations of a rotating cavity with axial throughflow at Grashof numbers of 3.03×10^9 and 3.03×10^{11}. It has systematically studied the effects of three modelling fidelities (URANS, DES, and LES) and mesh resolution. Simulations were verified in a mesh refinement study, and validated against experimental disk heat transfer data. There are multiple physical mechanisms that dominate in different areas of the flow, these mechanisms are distinct enough for it to be necessary to treat them differently in terms of both mesh resolution and adequate modelling fidelity. The main conclusions from this chapter are:

- Using adiabatic instead of isothermal disks changes the radius at which the radial direction of the near-disk flow reverses, indicating a significant feedback of wall heat transfer to aerodynamics.
- At the low Grashof number condition, the disk heat transfer was found to be insensitive to the modelling fidelity. The eddy viscosity present in the URANS solution prevented URANS from predicting the formation of coherent shroud streaks accurately. Surprisingly, DES also captured the formation of such streaks, despite being in URANS mode in the near-shroud region. The normalised mesh wall spacings for LES indicated that the streaks were well resolved. In the LES, the vorticity of the streaks was found to be concentrated to

within 1-3 cells width. This is very few cells for an important flow structure and indicates that wall mesh spacings alone are not enough to assess LES mesh resolution in this region.

- At the high Grashof number condition (near engine relevant conditions, and on the same order of magnitude as e.g. the computations of Atkins and Kanjirakkad (2014), the near-shroud streaks were observed to be less intense and of a smaller circumferential extent in the DES than the LES, reducing the shroud heat transfer. In contrast, on the disks, DES double accounted for the wall-normal velocity fluctuations, causing enhanced heat transfer. In the LES, a near-wall peak in the disk-normal velocity fluctuation was not observed, indicating that the near-disk layer remains laminar even at the high Grashof number condition. The double accounting by DES in the near-wall region points to potential issues with modelling the near-wall region with even a zonal RANS model.
- DES behaved inconsistently with its expected behaviour in all simulations (in different ways). Locally generated modelled turbulence was observed to be injected from the shroud into the bulk flow by the radial inflow, contaminating the entire solution with an elevated eddy viscosity.

Taking these conclusions together, it can be seen that to properly capture the aerodynamics within the cavity it is necessary to use wall resolved LES, and that high-fidelity thermal boundary conditions from CHT are necessary to properly capture the interaction of conduction within the disks and buoyancy effects within the cavity.

When used on the same (relatively high aspect ratio for LES) mesh for simulations at near engine-relevant conditions, LES performed better than DES. It is interesting to consider whether it is necessary to use hybrid URANS/LES wall modelling approaches for rotating cavities if the Ekman layers remain laminar as observed - it may be that

the usual LES mesh requirements are meaningless here, and a high aspect ratio grid of the type that would usually be used for DES gives more accurate and reliable results without the complication and additional uncertainty of a RANS model.

Chapter 4

Multiscale Sensitivities in Unsteady Conjugate Heat Transfer

4.1 Why Consider Unsteady CHT?

The results in the previous chapter showed that to accurate simulate the flow within rotating cavities it is necessary to:

- Use wall resolved LES to capture the effects of the substantially different small-scale flow structures in different parts of the cavity.
- Consider the thermal interaction of the fluid and solid domains (i.e. use CHT) to ensure that accurate thermal boundary conditions are supplied to the fluid domain.

Solving an LES fluid domain and an unsteady solid domain together in a time consistent manner is extremely challenging. There are two fundamental reasons for

this:

- The characteristic timescale of the solid domain is roughly 4 orders of magnitude greater than that of the fluid domain (He and Oldfield, 2011). The timescale disparity means that for a temporally converged LES-CHT simulation it would be necessary to run the simulation for 10,000 times as long as a standalone fluid domain simulation, rendering such simulations impossible.
- Under-resolving the thermal penetration depth in the solid domain risks overpredicting the magnitude of the wall temperature fluctuations by 1 - 2 orders of magnitude (Fadl and He, 2017). This means that, even if a certain frequency of fluctuation is not dynamically relevant to the flow physics when accurately captured, insufficient solid domain resolution could corrupt the entire flow field due to nonlinear interactions in the fluid domain.

Currently, the only method that consistently deals with these considerations while still allowing time-accurate calculation of the unsteady wall temperature is the closely coupled LES-CHT method of He (2019). The method decouples the time-average solid domain temperature and the fluctuating solid domain temperature. The time-average solid domain is marched in pseudo-time to an accurate steady state. The wall temperature fluctuations are calculated in the frequency domain using a semi-analytical wall transfer function approach derived from consideration of a 1D semi-infinite solid domain.

The semi-infinite assumption places a lower bound on the frequencies that can be considered. If the thermal penetration depth is larger than the solid domain thickness, a temperature fluctuation will need to be solved for in the solid domain to allow for the proper interaction with the geometry and external boundary conditions. In addition,

although it was briefly discussed in He (2019), there has been no demonstration of the validity of the 1D assumption when applied to LES-CHT.

A method that has been proposed to allow the solid temperature fluctuations to be captured is to decouple the time-average and fluctuating solid domains in the manner of Koren et al. (2017a,b, 2018). This is method is intended to allow the initial transient to be neglected by marching the time-average solid domain with an accelerated time-step, while allowing a consistent solution for the temperature fluctuations in the solid domain. Another approach is to calculate a (roughly) correct time-average state in the solid by accelerating the solid timescale, and then switching over to a directly coupled solution with the correct timescale in solid domain. The solid domain timescale can be accelerated by either scaling the thermal diffusivity as in Oh et al. (2021), or by simply increasing the solid domain time step as in Agostinelli et al. (2021); Kraus et al. (2018).

The aim of this chapter is to answer three questions to better understand what it takes to accurately solve for solid domain temperature fluctuations in an unsteady CHT analysis:

- What mesh size is required to accurately resolve a thermal penetration depth?
- Is the 1D assumption used by He (2019); He and Oldfield (2011) valid in the context of LES-CHT?
- Most importantly for the development of this thesis, to what extent can we do a time domain solution of the solid domain? Do the accelerated approaches discussed above lead to consistent temporally converged solutions?

The analysis focuses on the fluctuating steady state (i.e. fluctuations around a

constant mean temperature at a constant operating condition) behaviour of the fluid-solid coupled system. This is important as it is where hot components will spend the majority of their service life - a transient startup of a land-based gas turbine may take a few minutes, but its steady state operation is likely to last for several hours (Oh et al., 2021). Similar observations have been made about experimental rigs by He and Oldfield (2011). It is also important to note that accurate steady state computations are necessary for long timescale simulations such as those of Atkins (2013) - these almost always consider the flight cycle as a sequence of quasi-steady states.

In the remainder of this chapter, a test temperature fluctuation taken from near a rotating cavity disk in a fluid domain only LES analysis is first presented. Then, the wall transfer function approach from the LES-CHT method of He (2019) is outlined and some of its limitations discussed, before using it as a ground-truth method to address the above questions. Finally, we highlight the implications of the results on requirements for the consistent multiscale framework for LES-CHT that is developed in the next chapter.

4.2 Example LES Near-Wall Temperature Fluctuations

To ensure that this section is relevant to turbulence-resolved unsteady CHT simulations, much of it is based on analysing the response of a solid domain to a realistic near-wall temperature fluctuation. This temperature fluctuation is taken from a mid-radial location ($r/b = 0.6725$) 0.2 mm from the disk in a fluid domain-only LES simulation of Bohn et al. (2000)'s rotating cavity at a Grashof number of 4.86×10^{10}. 0.2 mm from the disk corresponds to a z^+ of approximately 16.

A time trace of the temperature fluctuations, which were recorded over a period of 60

revolutions, is shown in Fig. 4.1a, and its corresponding frequency spectrum is shown in Fig. 4.1b. The dominant feature of the near-wall temperature fluctuation is the low frequency oscillation that has a magnitude of slightly over 2 K and a frequency of 1.63 Hz. It was shown in Chapter 3 (and in Hickling and He (2021)) that the dominant near-wall temperature fluctuation is due to the slow anticyclonic rotation of the alternating regions of cold radial outflow and warmer radial inflow that make up the large scale flow structure.

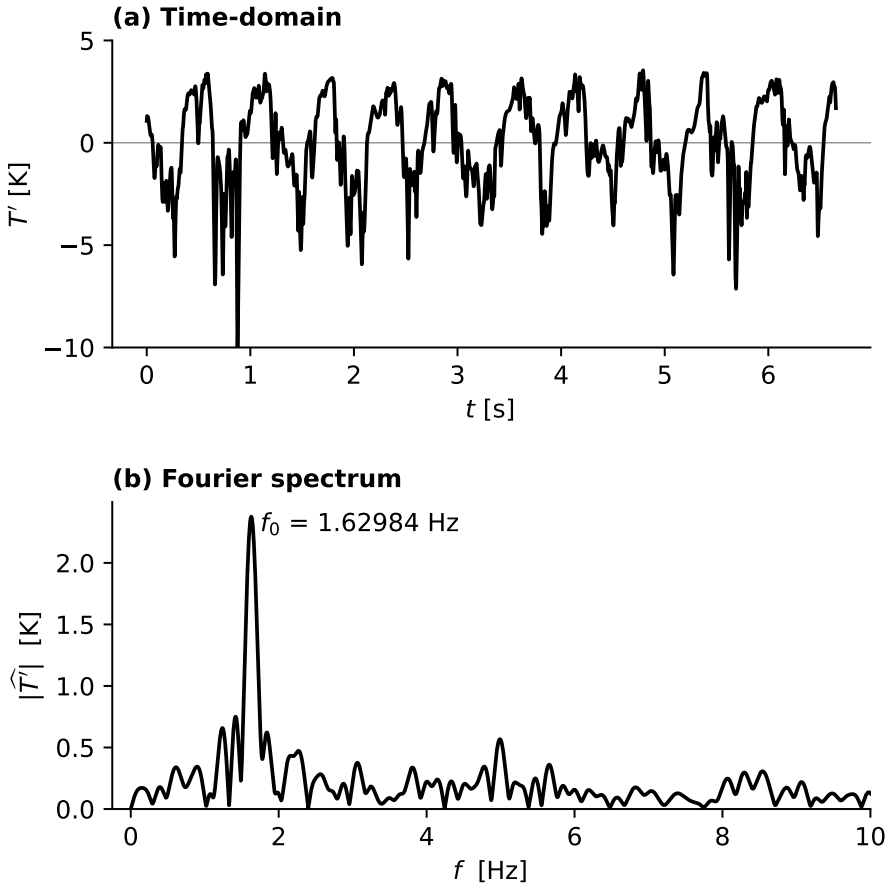

Figure 4.1. Near-disk temperature fluctuations in the time and frequency domain.

4.3 The Wall Transfer Function

In this chapter, the semi-analytical wall transfer function approach is used as a ground truth method for calculating steady state wall temperature fluctuations in 1D scenarios. The method was first proposed in He and Oldfield (2011) for dealing with deterministic unsteadiness, such as that from blade passing. It was extended by He (2019) to capture the effect of high-frequency turbulent fluctuations of the surface temperature of a nozzle guide vane with a thermal barrier coating. This section provides an overview of the closely coupled methodology and the derivation of the wall transfer function, before discussing some of the approaches limitations.

4.3.1 The Closely Coupled LES-CHT Method of He (2019)

Beginning with the general equation for unsteady conduction,

$$\frac{\partial}{\partial t}(\rho_s c_s T) = \nabla \cdot (k_s \nabla T), \tag{4.1}$$

the temperature and thermal properties are decomposed into the sum of time-average ($\widetilde{\psi}$) and fluctuating components (ψ') so that, for a generic variable ψ,

$$\psi = \widetilde{\psi} + \psi'. \tag{4.2}$$

Substituting this decomposition into Eq. (4.1), time-averaging, and assuming that the solid domain thermal properties are only dependent on the mean-temperature (i.e. $\rho_s', c_s', k_s' = 0$) yields an equation for the steady solid domain:

$$\frac{\partial \widetilde{T}}{\partial \tau} + \nabla \cdot \left(\widetilde{k_s} \nabla \widetilde{T} \right) = 0. \tag{4.3}$$

This can be solved by pseudo-time marching in τ at a large but stable time step provided that accurate time-average boundary conditions are available from the fluid domain.

The time-average boundary conditions come from the consideration of instantaneous 1D temperature continuity and heat-flux conservation ($q_f + q_s = 0$) on the interface. This gives

$$h_f(T_f - T_w) = h_s(T_w - T_s), \tag{4.4}$$

where the heat transfer coefficients are given by $h_f = k_f/\Delta x_f$, $h_s = k_s/\Delta x_s$. Δx_f and Δx_s are the cell centre to wall face centre distance in the fluid and solid domains as shown in Fig. 4.2.

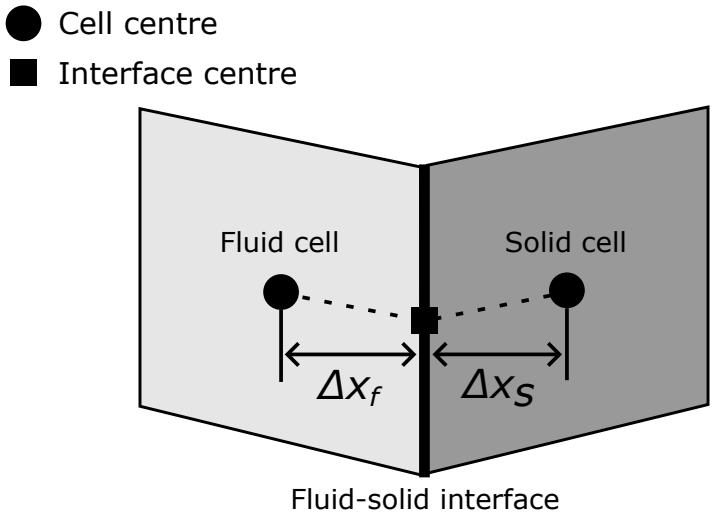

Figure 4.2. Fluid-solid coupled cell face terminology.

In directly coupled unsteady CHT, the instantaneous wall temperature would be calculated from

$$T_w = \frac{h_f T_f + h_s T_s}{h_f + h_s}; \tag{4.5}$$

this will be used later for studies on the unsteady behaviour of the solid domain. In the

closely coupled method, the Reynolds decomposition (Eq. (4.2)) is substituted for the heat transfer coefficients and temperatures in Eq. (4.4). The resulting equation is then time-averaged and rearranged to give the time-average wall temperature at time step $M+1$ from the averages at time step M as

$$\widetilde{T}_{w,M+1} = \left(\frac{\widetilde{h_f T_f} + \widetilde{h}_s \widetilde{T}_s - \widetilde{h'_f T'_w}}{\widetilde{h}_f + \widetilde{h}_s} \right)_M . \tag{4.6}$$

This interface condition enforces time-average temperature continuity and heat-flux conservation at every time step and inner iteration once the moving average is converged. In He (2019), the stability analysis of Giles (1997) was extended to this closely coupled approach. It was shown that, when using explicit time-marching, the stability condition is less restrictive than the corresponding stability condition for unsteady conduction in the fluid or solid domain.

The wall temperature fluctuations are calculated using the T-q transfer function C_{Tq}, that relates the Fourier harmonic of the heat flux into the solid domain ($\widehat{q}$) to the harmonic of the wall temperature fluctuation ($\widehat{T}_w$) as

$$\widehat{q} = \widehat{C}_{Tq} \widehat{T}_w . \tag{4.7}$$

The derivation of C_{Tq} is detailed in the next subsection, once the discussion of the closely coupled approach has been completed. It is calculated analytically from the consideration of unsteady conduction in a 1D semi-infinite solid domain.

The heat flux harmonic $\widehat{q}_f$ is calculated from a 1D finite difference expression of harmonic heat-flux conservation and temperature continuity as

$$\widehat{q} = \widetilde{h}_f (\widehat{T}_f - \widehat{T}_w). \tag{4.8}$$

This is combined with Eq. (4.7) to form the semi-analytical wall transfer function for the wall temperature harmonic as

$$\widehat{T}_w = \frac{\widetilde{h}_f}{\widetilde{h}_f + \widehat{C}_{Tq}} \widehat{T}_f \tag{4.9}$$

The wall temperature fluctuation can be reconstructed in the time domain from

$$T'(t) = \sum_{n=1}^{N} A_n \cos(n\omega_0 t) + B_n \sin(n\omega_0 t), \tag{4.10}$$

where N is the number of harmonics, with base frequency ω_0. The real valued harmonic coefficients for the n^{th} harmonic are given by $\widehat{T}_n = A_n - iB_n$. The temperature harmonics in the fluid wall-adjacent cell ($\widehat{T}_f$) are updated recursively using a sliding discrete Fourier transform (DFT) as

$$\begin{cases} A_{n,M+1} = A_{n,M} + \dfrac{\omega_0 \Delta t_f}{\pi} \left(T'_M - T'_{M-M_0}\right) \cos(n\omega_0 t) \\ B_{n,M+1} = B_{n,M} + \dfrac{\omega_0 \Delta t_f}{\pi} \left(T'_M - T'_{M-M_0}\right) \sin(n\omega_0 t) \end{cases}, \tag{4.11}$$

where the value of the temperature fluctuation 1 period of the base harmonic ago, T'_{M-M0}, is also reconstructed from Eq. (4.10).

4.3.2 Derivation of the T-q Transfer Function

The T-q transfer function can be derived following the procedure of Schultz and Jones (1973). It was originally used to calculate heat fluxes from unsteady wall temperature measurements using thin film gauges. The equation for 1D unsteady conduction (with z as the wall-normal direction and with constant solid thermal properties), is Laplace transformed to obtain a second order homogenous differential equation:

$$\frac{d^2\overline{T}}{dz^2} - \frac{\mathcal{S}}{\alpha_s}\overline{T} = 0. \tag{4.12}$$

Here, $\alpha_s = k_s/\rho_s c_s$ is the solid domain thermal diffusivity, $\mathcal{S}$ is the Laplace variable, and $\overline{T}$ is the Laplace transform of T. This has the general solution

$$\overline{T} = C_1 \exp\left(z\sqrt{\frac{\mathcal{S}}{\alpha_s}}\right) + C_2 \exp\left(-z\sqrt{\frac{\mathcal{S}}{\alpha_s}}\right), \tag{4.13}$$

which upon applying the boundary conditions for a semi-infinite solid domain subject to a wall heat flux,

$$\left.\frac{d\overline{T}}{dz}\right|_{z=0} = -\frac{\overline{q}}{k_s} \qquad \text{and} \qquad \lim_{z\to\infty} \overline{T} = 0, \tag{4.14}$$

becomes

$$\overline{T} = \sqrt{\rho_s c_s k_s}\sqrt{\mathcal{S}} \exp\left(-z\sqrt{\frac{\mathcal{S}}{\alpha_s}}\right) \overline{q}. \tag{4.15}$$

The T-q transfer function as used in Eq. (4.9) is then obtained by evaluating Eq. (4.15) at the wall ($z = 0$), and recasting into the frequency domain to yield

$$\widehat{C}_{Tq} = \sqrt{\rho_s c_s k_s}\sqrt{i\omega}. \tag{4.16}$$

Recasting $\widehat{C}_{Tq}$ into the frequency domain (by using the substitution $\mathcal{S} \to i\omega$, i.e. evaluating the Laplace transform along the imaginary axis) is key to the success of the wall transfer function in He (2019). This is because, being in the frequency domain, it only retains the fluctuating steady state component of the response and discards any transients caused by the wall temperature fluctuation being a causal signal (i.e. being initialised from 0).

4.3.3 Frequency Based Wall Transfer Function Challenges

Despite its success in He (2019), there are a number of challenges and obstacles to wider adoption of the frequency domain wall transfer function approach in its original frequency domain implementation.

It is not possible to use wall transfer function for low frequencies of temperature fluctuation, such as those that come from large-scale coherent structures in the fluid domain. An example of these large-scale coherent structures is the passing of the radial arms in a rotating cavity as in the discussed in Fig. 4.1. The wall transfer function can not be used here because the semi-infinite assumption is not valid because the thermal penetration depth is larger than the solid domain thickness. To properly capture the effects of low frequency temperature fluctuations, it would be necessary to carry out the solution in the solid domain to allow for the physical interactions with geometry and external boundary conditions.

Another challenge is that discrete harmonics seem to be poorly suited to capturing broadband phenomena. Choosing a good combination of number of harmonics and base frequency can be difficult without prior knowledge of the flow and some trial and error on a sample signal. Between 50 and 100 harmonics were necessary to capture the fluid domain broadband unsteadiness in an LES-CHT of a nozzle guide vane in He (2019), creating large additional memory requirements for the LES-CHT solution when using the method. Using 50 to 100 harmonics would require between 100 and 200 computationally expensive trigonometric function evaluations per coupled wall boundary face at each time step; this was observed in (He, 2019) to lead to a 30% increase in computation time.

The final challenge is that the validity of the 1D assumption has not been rigorously assessed. Based on some preliminary discussion (He, 2019), it is expected to be

valid. If the thermal penetration depth is comparable to, or smaller than, the mesh spacing, it is reasonable to expect the flux on wall boundary faces to be accurately evaluated by neglecting the local wall-parallel variations. However, prior to this thesis, this had yet to be demonstrated in a computational experiment.

4.4 Fluid-Solid Timescale Disparity

4.4.1 Initial Transient

As discussed in the literature review, the issue of the fluid-solid timescale disparity is well known for the case where a time-consistent unsteady solid domain is initialised from an initial state that is not close to its steady state.

As a working approximation, it is commonly stated that the characteristic timescales of the fluid and solid domain differ by four orders of magnitude. To gain a feel for this in rotating cavities, the timescale t_s of the diffusive process in the solid domain can be estimated from the Fourier number,

$$\frac{\alpha_s t_s}{L_s^2} = 1, \tag{4.17}$$

where α_s is the solid domain thermal diffusivity, and L_s is a characteristic solid domain timescale. The thermal behaviour of the fluid domain is dominated by convective processes; the timescale of its initial transient, t_f, is thus expected to be on the scale of a flow through time, so that

$$\frac{U t_f}{L_f} = 1. \tag{4.18}$$

Here, U is the fluid bulk velocity and L_f is a characteristic fluid domain length scale. This expression for the flow through time is more relevant to flows such blade

passages without large-scale circulations. However, it would be surprising if the fluid domain timescale differed from this estimate by more than an order of magnitude in rotating cavities.

Taking the LES simulations in Section 3.4, U corresponds to the velocity in the radial arms and is approximately 1 m/s, and $L_s = L_f$ correspond to the disk outer radius, 0.4 m. This yields a characteristic timescale of $t_f = 0.4$ s for the fluid domain. Using the thermal properties of titanium for the solid domain (see Tab. A.1) gives a characteristic timescale of $t_s = 56 \times 10^3$ s (approximately 15-16 hours) for the solid domain initial transient.

The ratio t_s/t_f is 140,000 - i.e. to reach a steady state in a coupled LES-CHT simulation where the fluid and solid domains were marched with the same time step would take 140,000 times as long as a standalone fluid domain analysis. This is clearly prohibitive - standalone fluid domain LES simulations are expensive enough as it is - so it is necessary to use methods to accelerate this timescale. To do this and maintain the time-accuracy of the solid domain in steady state LES-CHT simulations, it is necessary to decouple the time-average and fluctuating temperatures in the solid domain so that the initial transient in the solid domain can be accelerated, and the temperature fluctuations can either be accounted for separately or discarded.

4.4.2 Long-Lived Errors from Accurate Time-Average Initial States

One of the goals for this chapter was to see if it is possible to use time-domain methods for unsteady solid domain solution in LES-CHT. To investigate this, it is necessary to examine whether a solid domain initialised at a temporally converged state is still subject to an initial transient effect. This is relevant to many methods that have previously been used to carry out unsteady CHT with an LES fluid domain -

these approaches either:

- Accelerate the solid timescale until a steady state is reached, and then switch the solid domain back to the correct timescale to solve for the unsteady temperature at a steady state (Agostinelli et al., 2021; Kraus et al., 2018; Oh et al., 2021).
- Decouple the time-mean and fluctuating temperature so that the time-mean response can be accelerated, and the temperature fluctuations can be solved by time marching (Koren et al., 2017a,b, 2018).

This section will show that, while these approaches are simple and attractive, they are still subject to the issues surrounding the scale disparity between the solid initial transient and fluid domain timescales. To illustrate this, a numerical solution of 1D unsteady conduction was carried out in a titanium solid domain (see Tab. A.1 for thermal properties), with length $L = 5\,\text{mm}$ to match the disk thickness in Bohn et al. (2000). At $x/L = 0$, the wall temperature was calculated with Eq. (4.5), with $T_f = 10\sin(2\pi f_0 t)$ - a sine wave at the frequency observed in the fluid domain only LES simulation (see Fig. 4.1b) of the cavity of Bohn et al. (2000). An adiabatic boundary condition was applied at $x/L = 1$. A diagram of the domain is shown in Fig. 4.3. The numerical solution was carried out with a forward-in-time and central-in-space scheme and the results were verified to be mesh and time-step independent.

The results of this time-domain unsteady solution are shown in Fig. 4.4, along with a frequency domain analytical solution calculated by applying the boundary conditions

$$\overline{T}\Big|_{z=0} = \overline{T_w} \qquad \text{and} \qquad \frac{d\overline{T}}{dz}\bigg|_{z=L} = 0, \tag{4.19}$$

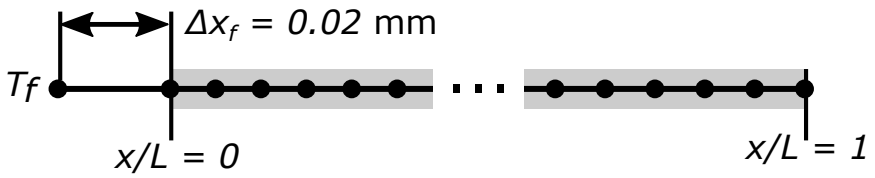

Figure 4.3. Diagram of the 1D titanium solid domain and driving fluid temperature fluctuation used in the investigation of the solid domain timescale disparity.

to the general solution for 1D unsteady conduction (Eq. (4.13)). The resulting expression, recast into the frequency domain to give the fluctuating steady state response, is

$$\frac{\widehat{T}(z)}{\widehat{T_w}} = \mathcal{A}(\omega)\exp\left(z\sqrt{i\omega/\alpha_s}\right) + \mathcal{B}(\omega)\exp\left(-z\sqrt{i\omega/\alpha_s}\right), \tag{4.20}$$

where the frequency dependent terms $\mathcal{A}$ and $\mathcal{B}$ are given by

$$\mathcal{A}(\omega) = \frac{\exp\left(-L\sqrt{i\omega/\alpha_s}\right)}{2\cosh\left(L\sqrt{i\omega/\alpha_s}\right)} \tag{4.21}$$

$$\mathcal{B}(\omega) = 1 - \mathcal{A}(\omega). \tag{4.22}$$

This is used to calculate the heat flux in to the domain as

$$\frac{\widehat{q}}{\widehat{T_w}} = -\frac{k_s}{\widehat{T_w}}\left.\frac{d\widehat{T}}{dz}\right|_{z=0} = \sqrt{\rho_s c_s k_s}\sqrt{i\omega}\left[-\mathcal{A}(0) + \mathcal{B}(0)\right], \tag{4.23}$$

which can then be used as a direct replacement for $\widehat{C}_{Tq}$ in Eq. (4.9) to calculate the temperature harmonic at axial location z with a fluid domain temperature harmonic of $\widehat{T}_f = -10i$ at frequency f_0.

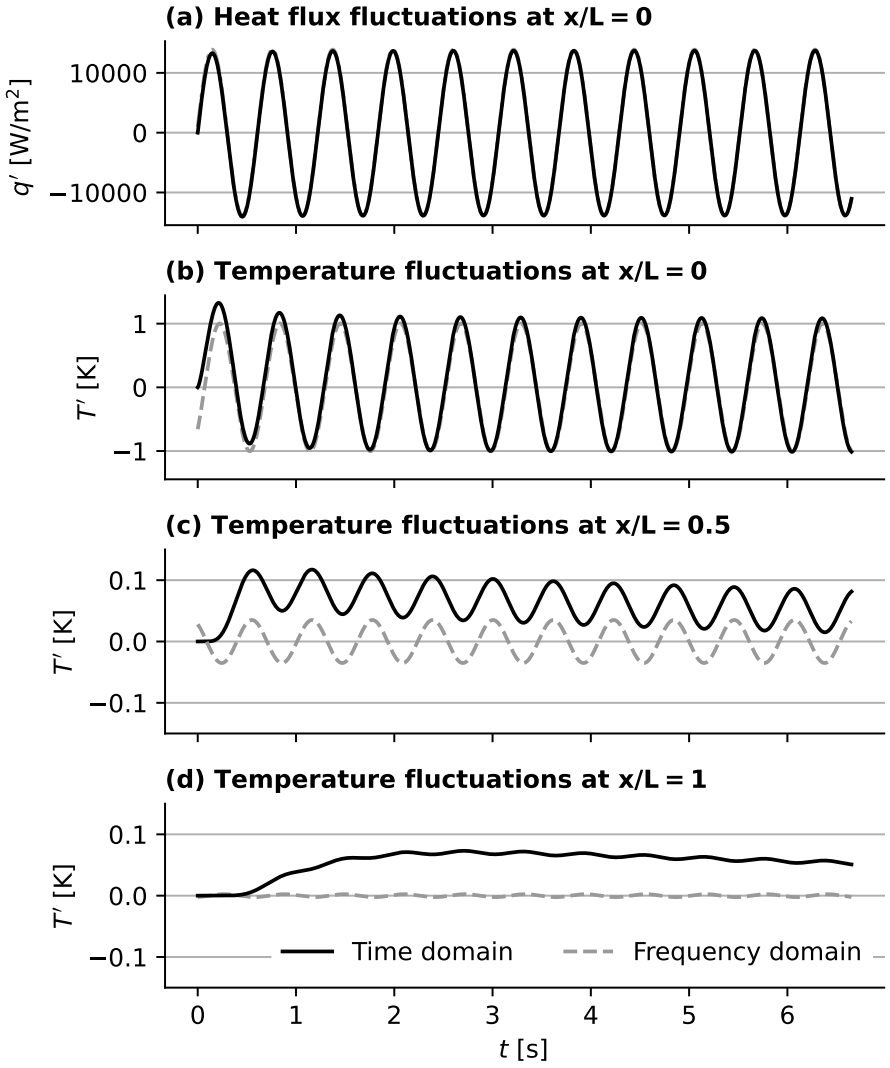

Figure 4.4. Single-direction coupled response of a 1D Titanium solid domain to fluid temperature fluctuations. ($L = 5\,\text{mm}$)

In Fig. 4.4a and Fig. 4.4b, it can be seem that the wall heat flux and temperatures reach a fluctuating steady state almost instantaneously. However, in Fig. 4.4c and Fig. 4.4d, we see that, away from the model fluid-solid interface, the time domain solution has a relatively significant steady state temperature error that persists for the full duration of the solution (which corresponds to 60 revolutions of the rotating cavity). Despite the fluid temperature fluctuations used to calculate the wall temperature at $x/L = 0$ having a time-average of 0, this initial transient does not have a mean of zero, and takes a significant amount of time to approach the fluctuating steady state that is achieved instantaneously by the analytical frequency domain solution.

The reason for this is that, in the time-domain, it is not possible to simply apply a sine wave as an unsteady boundary condition. When a CFD user tries do this (either as an external boundary condition or as an interface condition in an unsteady CHT analysis), they are actually applying the function $H(t)\sin(\omega t)$: a sine wave multiplied by a Heaviside step function (i.e. a single-sided, or causal, signal in signal processing terms). This destroys the periodic nature of the problem, meaning that it is necessary to drive out the initial transient to get to the fluctuating steady state that we are interested in.

Although the causal nature of the time domain solution had little influence on the coupled wall heat flux and temperature in this simple 1D case, the initial transient away from the wall could contaminate other areas in a 3D solid domain - even though it was initialised from a temporally converged state. To the author's knowledge, this fact that has not been previously recognized in the literature.

The results in Fig. 4.4 have implications for the development of a multiscale framework for LES-CHT that can accurately capture the effect of lower frequency temperature

fluctuations (such as those from large-scale coherent flow structures). It is still necessary to solve the lower frequency temperature fluctuations directly in the solid domain so that the proper 3D interactions with geometry and external thermal boundary conditions can be captured. The analysis in this section shows that the only way to do this (without still having to drive out a long-lived steady state temperature error) would be to carry the unsteady solid domain solution in the frequency domain. A time domain solution is not suitable for LES-CHT, whereas using a frequency domain solution would enable immediate convergence to accurate steady state temperature fluctuations (given accurate solid domain boundary conditions).

4.5 Resolution of the Thermal Penetration Depth

Before proceeding with analysing the 1D assumption in the wall transfer function, we need to be clear exactly what wall-normal mesh spacing is required for accurately capturing the transient response of the solid to fluid domain temperature fluctuations. This was one of the motivating factors for the use of the wall transfer function by He (2019) - at higher frequencies of thermal unsteadiness (or low solid thermal diffusivities), it is not feasible to resolve the thermal penetration depth of the temperature fluctuations in the solid domain, so it is necessary to treat them locally on the wall.

The analysis of Fadl and He (2017) (detailed in Section 2.3.2) yielded two equations (Eqs. (2.15) and (2.16)) that describe the response of the wall temperature and heat flux fluctuations when the thermal penetration depth is under-resolved in the solid domain. The derived equations predict that under-resolving the thermal penetration results in an overprediction of the amplitude of temperature fluctuations, and a

corresponding underprediction of the amplitude of heat flux fluctuations. This is qualitatively consistent with several observations in unsteady CHT computations (He, 2013, 2019; He and Oldfield, 2011; Shahi et al., 2015).

In this section, the focus is on the amplification of the temperature fluctuations. This is more important for unsteady CHT than the heat-flux response, as both Dirichlet-Dirichlet and Neumann-Dirichlet coupling schemes usually involve applying the temperature as a boundary condition to the fluid domain, where nonlinear interactions could feasibly alter important aspects of the system. An example of this is in the URANS-CHT simulations of Shahi et al. (2015), where an over-prediction in wall temperature fluctuations caused the amplitude of pressure limit cycle oscillations in a combustor to be over-predicted by a factor of 2 to 3.

For ease of reference, the equation for the erroneous amplification of the wall temperature fluctuations by under resolution of the thermal penetration depth, Eq. (2.15), is reproduced below:

$$\frac{|\widehat{T}'_w|_{err}}{|\widehat{T}'_w|} = \frac{1 + (Bi_m/\beta)}{1 + Bi_m}, \tag{2.15}$$

where Bi_m is the mesh Biot number, and $\beta = \delta_p/\Delta x_s$ is the ratio of the thermal penetration depth (δ_p) to the cell centre to face centre distance in the wall-adjacent cell (Δx_s). When the thermal penetration depth is under resolved, β is less than one, causing the amplification predicted by Eq. (2.15) to grow roughly proportional to $1/\beta$ as the thermal penetration depth is decreased. Given that $\delta_p \propto 1/\sqrt{f}$, the amplification is also expected to be asymptotically proportional to the square root of the frequency of thermal unsteadiness that is being applied to the interface.

The analysis in (Fadl and He, 2017) is based on a linear variation of the temperature

fluctuation within the thermal penetration depth. It can be seen with reference to the analytical solution in Eq. (4.15) that this is not the case. It is therefore of interest to examine the behaviour of an under-resolved solid domain in a representative unsteady CHT setup from the perspective of Eq. (2.15). This will enable two questions relevant to LES-CHT to be answered:

1. Does the erroneous temperature fluctuation amplification vary in the way predicted by Eq. (2.15)?
2. How many cells are necessary to accurately resolve the thermal penetration depth?

To investigate this, a one-way coupled analysis was carried out using a representative LES fluid domain temperature fluctuation. As the issue at hand is due to the numerical discretisation of the solid domain (i.e. not an inherent feature of the solid domain physics) it makes sense to use a methodology for unsteady conduction that is representative of what would be used with the second order general-purpose flow solvers commonly used in the heat transfer community for application-orientated LES.

To be consistent with the previous LES analyses in this thesis, ANSYS Fluent is used for the analysis. A 5 mm^3 solid domain (5 mm corresponding to the disk thickness in the experiments of Bohn et al. (2000)) was meshed with 10 cells in each direction, giving $\Delta x_s = 0.25$ mm. This mesh size was chosen to be broadly consistent with what might be used in an affordable LES-CHT analysis. The LES fluid domain temperature fluctuations shown in Fig. 4.1 were coupled to the solid domain using the directly coupled interface condition (Eq. (4.5)) on one face, and all other faces were adiabatic. The solid domain was initialised at the correct time-average temperature to minimise effects from the initial transient (the validity of this approach for avoiding the initial

transient in a proper LES-CHT analysis will be discussed in the next section). The thermal properties of epoxy (see Tab. A.1) were used for the solid domain.

As a ground truth for calculating the wall temperature fluctuations, the wall transfer function (Eq. (4.9)) is used, with the fluid domain temperature harmonics post-processed from the signal in Fig. 4.1 with a fast Fourier transform. Although the solid domain used is 3D, the problem being investigated is 1D, meaning that for now the validity of the 1D assumption in the wall transfer function is not a concern. The thermal penetration depth of the largest frequency that could be present in the test fluid domain temperature fluctuation (which covers 60 cavity revolutions) is 2.74 mm, meaning that the semi-infinite assumption is also valid.

A snapshot of the resulting wall temperature fluctuations in the time domain is shown in Fig. 4.5. As expected, the amplitude of the wall temperature fluctuations is over-predicted across a wide range of timescales. Although there is a small over-prediction of the large timescale temperature fluctuations at 1.63 Hz (see Fig. 4.1b), the most striking feature of Fig. 4.5 is the significantly larger higher frequency temperature fluctuations.

A clearer picture of the dependence of the wall temperature fluctuations on β in visible in Fig. 4.6. The data in this plot was calculated by taking the amplitude of the wall temperature harmonics from the time-marching solid domain and dividing through by the amplitude of the wall temperature harmonics from the wall transfer function. The amplification introduced by the solid domain mesh resolution is significant. It starts to occur when $\beta \approx 8$ (i.e. there are 4 cells within the thermal penetration depth) and at the Nyquist frequency associated with the solid domain time step it reaches a factor of 40. In higher Reynolds number simulations with a smaller fluid domain time step, this has the potential to exceed two orders of magnitude. The results agree very well with

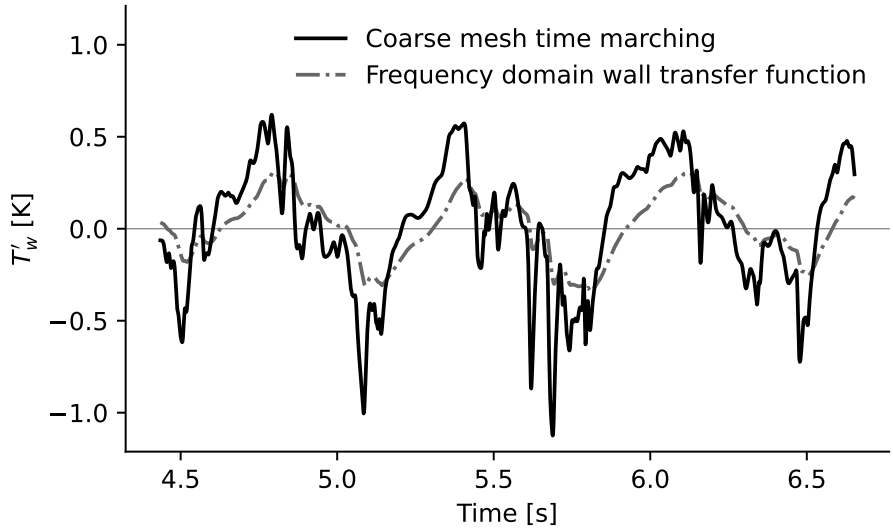

Figure 4.5. Wall temperature fluctuations calculated using an under-resolved solid domain mesh and the wall transfer function.

a slightly modified Eq. (2.15), where β is replaced by 6β to 8β to reflect that 3 to 4 cells seem necessary to properly resolve the thermal penetration depth.

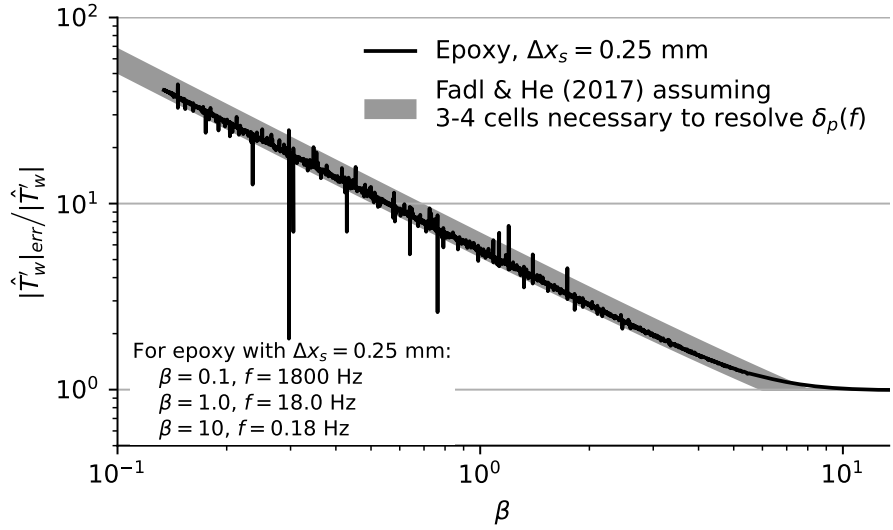

Figure 4.6. Dependence of the erroneous wall temperature fluctuation amplification on resolution of the thermal penetration depth.

Between 3 and 4 cells within the thermal penetration depth are necessary to accurately resolve a given frequency of temperature fluctuation. For the Nyquist

frequency in this analysis, this would correspond to a cell size of micrometers, smaller than the fluid domain wall normal mesh spacing. Using a solid domain mesh of this size would render unsteady CHT computations impractical, even if issues related to the initial transient could be overcome. It is therefore necessary to control the spectral content of any temperature fluctuations that are solved in the solid domain - even if the frequencies of interest are properly resolved in the solid domain, higher frequencies will be amplified by the solid domain mesh, contaminating the results with non-physical high frequency wall temperature fluctuations. In addition, temperature fluctuations that are unresolvable by the solid domain mesh should be dealt with locally on the wall using the wall transfer function.

4.6 Assessment of the 1D Assumption Within the Wall Transfer Function

The 1D assumption is a central assumption in wall transfer function approach used for LES-CHT by He (2019). However, apart from a small discussion in He (2019), there has not been much attention dedicated to its validity in the context of LES-CHT. In particular, it would be good to know if the thermal footprint on the near-wall region of large eddies (whose size is expected to be on the order of a boundary layer's thickness) is captured, as these are the structures that are responsible for the significant heat transfer enhancement in turbulent boundary layers. It is worth noting that validity of the 1D assumption should not only be of interest in the computational heat transfer community - since the work of Schultz and Jones (1973), approaches with the same origin as the wall transfer function have formed the basis of many experimental heat transfer measurement campaigns in both gas turbine and

hypersonic flows.

4.6.1 Scaling Analysis

To gain a qualitative understanding of how robust the 1D assumption is when used for the wall transfer function in LES-CHT, it is useful to conduct a scaling analysis of 3D unsteady conduction. We do this by considering the frequency domain version of Eq. (4.1),

$$i\omega\rho_s c_s \widehat{T} = k_s \left(\frac{\partial^2 \widehat{T}}{\partial x^2} + \frac{\partial^2 \widehat{T}}{\partial y^2} + \frac{\partial^2 \widehat{T}}{\partial z^2} \right). \tag{4.24}$$

Assuming that the temperature varies periodically in the wall parallel x and y directions, with wave numbers κ_x and κ_y; this can be rewritten as

$$\frac{\partial^2 \widehat{T}}{\partial z^2} - \left(\frac{i\omega}{\alpha_s} + \kappa_x^2 + \kappa_y^2 \right) \widehat{T} = 0. \tag{4.25}$$

This can then be solved in the same way used to derive the T-q transfer function by Schultz and Jones (1973) to yield an expression for the wall temperature fluctuations of a semi-infinite (in the z-direction) domain subject to a spatially and temporally periodic heat flux as

$$\widehat{q} = \sqrt{i\omega\rho_s c_s k_s + k_s^2(\kappa_x^2 + \kappa_y^2)}\,\widehat{T}_w. \tag{4.26}$$

For the 1D assumption to be valid, we need the response from the 3D semi-infinite unsteady conduction problem to be the same as 1D unsteady conduction problem, so that

$$\sqrt{i\omega\rho_s c_s k_s + k_s^2(\kappa_x^2 + \kappa_y^2)} \approx \sqrt{i\omega\rho_s c_s k_s}. \tag{4.27}$$

For this to be the case,

$$(\kappa_x^2 + \kappa_y^2) \ll \frac{\omega}{\alpha}, \tag{4.28}$$

which, assuming that one wave number is dominant (as is usually the case for streaks in wall bounded turbulence (Sagaut, 2006)) can be rearranged to give $Fo_{\omega,\kappa} \ll 1$ as a condition for the validity of the 1D assumption. Here $Fo_{\omega,\kappa}$ is a Fourier number at frequency ω and wave number κ, and is defined as

$$Fo_{\omega,\kappa} = \frac{\alpha_s \kappa^2}{\omega}. \tag{4.29}$$

To see whether the condition for the validity of the 1D assumption ($Fo_{\omega,\kappa} \ll 1$) can be expected to be valid in LES-CHT, it is assumed that the smallest scales of the flow are resolved by 10 mesh cells (as suggested is necessary in Sagaut (2006)), so that

$$\kappa \approx \frac{2\pi}{10\Delta x}. \tag{4.30}$$

The temporal variation caused by these small spatial scales is assumed to covered by 10 time-steps, giving

$$\omega \approx \frac{2\pi}{10\Delta t}. \tag{4.31}$$

In an LES, both the CFL number and normalised wall-normal spacing are expected to be approximately 1. Basing the CFL number on the characteristic flow velocity U and wall-parallel mesh spacing Δx gives

$$CFL = \frac{U\Delta t}{\Delta x} = 1. \tag{4.32}$$

Substituting the three previous expressions into our definition for the Fourier number (Eq. (4.29)) gives

$$Fo_{\omega,\kappa} = \frac{2\pi}{10}\frac{\alpha_s}{U\Delta x}. \tag{4.33}$$

This expression still requires some work before a meaningful order of magnitude can

be calculated for $Fo_{\omega,\kappa}$. The normalised wall spacing (with dimensional wall normal spacing $\Delta z \approx \Delta x/10$ for LES) is given by

$$y^+ = \frac{\rho_f u_\tau \Delta z}{\mu} = 1. \tag{4.34}$$

Expressing the friction velocity u_τ as

$$u_\tau = \sqrt{\frac{\tau_w}{\rho_f}} = \sqrt{\frac{C_F}{2}} U, \tag{4.35}$$

(where the wall shear stress is calculated from the friction coefficient C_F as $\tau_w = C_F \rho_f U^2/2$) results in an expression that, when substituted into Eq. (4.33), reduces the expression for the Fourier number to

$$Fo_{\omega,\kappa} \approx \frac{2\pi}{10} \sqrt{\frac{C_F}{2}} \frac{\alpha_s}{Pr\, \alpha_f}. \tag{4.36}$$

C_F is evaluated at a Reynolds number of 1×10^6 using the $1/7^{\text{th}}$ root velocity profile to give

$$C_F = 0.0576\, Re^{-1/5} = 3.63 \times 10^{-3}. \tag{4.37}$$

Using the thermal properties of titanium (see Tab. A.1), and $Pr = 0.71$ and $\alpha_f = 22 \times 10^{-6}\,\mathrm{m}^2/\mathrm{s}$ for air, gives

$$Fo_{\omega,\kappa} \approx 5 \times 10^{-3}. \tag{4.38}$$

This value is significantly less than one, meeting the condition derived earlier for the validity of the 1D assumption in LES-CHT ($Fo_{\omega,\kappa} \ll 1$). While this result is encouraging, several assumptions have been made to reach it, so it is desirable to have direct computational evidence of the validity of the 1D assumption.

4.6.2 Computational Experiment

To further evaluate the 1D assumption, temperature traces were recorded 0.2 mm from the wall in a 10 $\times$ 10 point grid from 60 revolutions of a fluid domain only LES. The grid centred on the same radial location as the signal in Fig. 4.1 and had a point-to-point spacing of 1 mm in each direction. The 1 mm spacing was chosen as it is approximately the same size as the LES grid wall-parallel spacing, which ensures that the conclusions of this analysis are relevant to LES-CHT.

Instantaneous values of the temperature fluctuations calculated from the signal at each cell point are shown in Fig. 4.7a. To give an impression of the higher spatial and temporal frequency components of the signal, a high pass filtered version of the signal is shown in Fig. 4.7b. The higher frequency turbulent structures are resolved by around 4-8 cells, as expected from the analysis of LES flow fields in rotating cavities presented earlier in this thesis and the general discussion in Sagaut (2006).

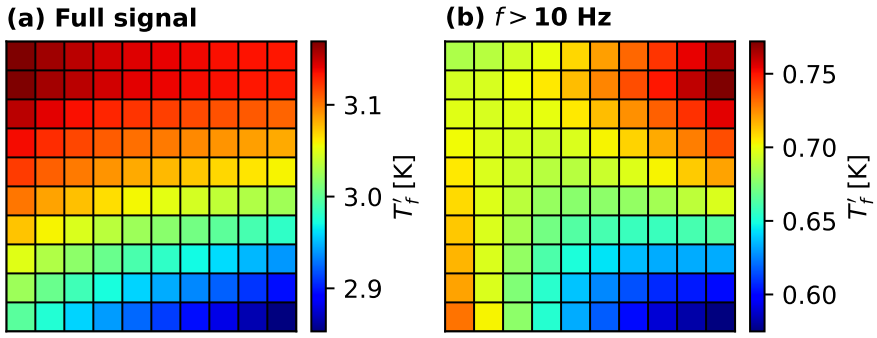

Figure 4.7. Spatial distributions of fluid temperature fluctuations coupled to the 3D domain.

To directly test the 1D assumption, the grid of temperature fluctuations was coupled to a titanium (see Tab. A.1) 3D solid domain. The solid domain had a dimension of 10 mm in the wall parallel directions, and 5 mm in the wall normal direction, to be consistent with the disk thicknesses in the experiment of Bohn et al. (2000). It was meshed with 10 uniformly spaced cells in the wall parallel directions, and 100 uniformly

spaced cells in the wall-normal direction to resolve the thermal penetration depth.

The solid domain used the same time step as was used in the standalone LES simulation, $\Delta t_s = 4.62 \times 10^{-4}$ s, giving a Nyquist frequency of 1082 Hz. This number of cells in the wall normal direction resulted in a mesh spacing of 0.05 mm. This is approximately equal to the thermal penetration depth of the Nyquist frequency, which is 0.053 mm. Although from the analysis in Section 4.5 this would be considered enough to fully resolve the thermal penetration depth at the Nyquist frequency, it is small enough to resolve all frequencies below 136 Hz with at least 3 cells; covering the significant majority of the spectral energy of the test temperature fluctuations. The solid domain wall temperatures were calculated at each coupled boundary face using the directly coupled interface condition given in Eq. (4.5). To remove the effects of the initial transient as best as possible from this analysis, the first 30 revolutions worth of wall temperature fluctuations were discarded.

At each coupled boundary face, an error metric was computed using the root-mean-squared (RMS) of the difference of the temperature fluctuation calculated with the wall transfer function ($T'_{w,\,TF}$) and the temperature fluctuation calculated from the last 30 revolutions of time-marching the 3D solid domain ($T'_{w,TM}$). This was normalised by the RMS of the solid domain wall temperature fluctuations as shown by

$$\text{normalised error} = \frac{\text{RMS}\left(T'_{w,\,TF} - T'_{w,TM}\right)}{\text{RMS}\left(T'_{w,TM}\right)}. \tag{4.39}$$

The values of Eq. (4.39) calculated over the full 30 revolutions of the analysis are shown in Fig. 4.8a. To allow an assessment of the frequency dependence of the validity of the 1D assumption (and implicitly also its dependence on the spatial scale of

the near-wall unsteadiness), the normalised error in Fig. 4.8b-d, is calculated by temperature fluctuations that have been band-pass filtered in the indicated frequency range.

The results show that the 1D assumption is valid in the context of LES-CHT. In the full signal in Fig. 4.8a and the low frequency (1-10 Hz) components of the signal in Fig. 4.8b, the error is uniformly less than 1%. Moving up to the mid-frequencies (10-100 Hz), we see that the error is a little larger; up to around 1.5%. The larger error in the mid-frequency range is likely due to the smaller length scale of the flow structures that make up this portion of the signal creating a small amount of lateral conduction between local temperature minima and maxima. In addition, it can be seen by comparing Fig. 4.8b and c to Fig. 4.8a that the low frequency components are the dominant feature of the near-wall temperature fluctuations. It is worth highlighting that a 1.5% error is still very small, and definitely supportive of the validity of the 1D assumption. To check for mesh-dependency in its conclusion, the analysis was repeated with 1000 cells in the wall normal direction; meaning that the thermal penetration depth of the Nyquist frequency was resolved by 10 cells. This is shown in Fig. 4.9 - again the error in the full signal is negligible compared to the other sources of uncertainty discussed in this chapter.

In this section, a scaling analysis and a computational experiment have shown that the 1D assumption within the wall transfer function is valid in the context of LES-CHT. It is worth noting that the uncertainty introduced by using the 1D assumption (at worst 2% in the computational analysis) is around one order of magnitude smaller than the uncertainty inherent in time marching a solid domain from a temporally converged state as observed in Section 4.4.2. In addition, it is several orders of magnitude smaller than the uncertainties that would arise from under-resolution of the thermal

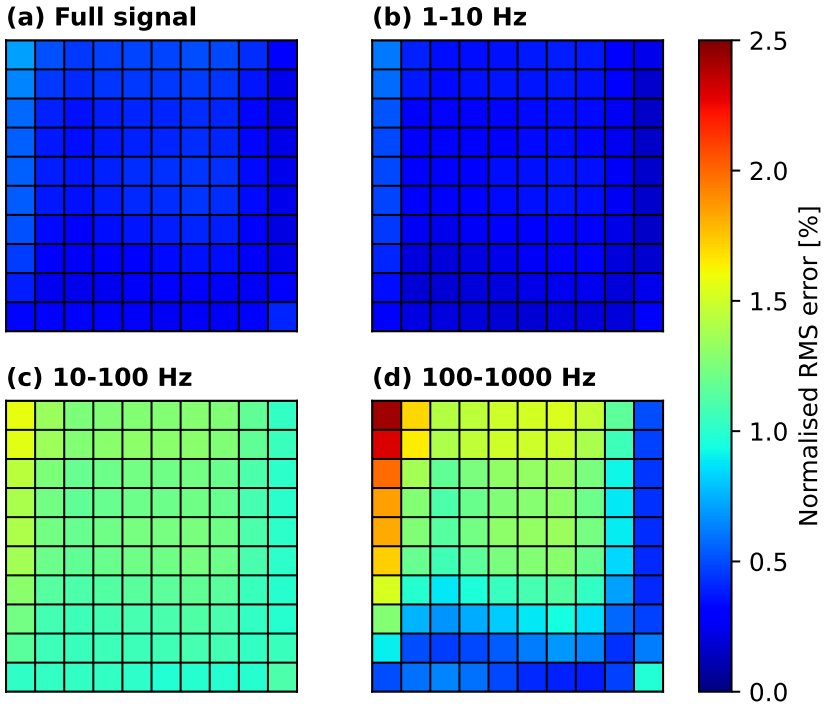

Figure 4.8. Normalised wall temperature fluctuation RMS error with 100 cells in wall normal direction.

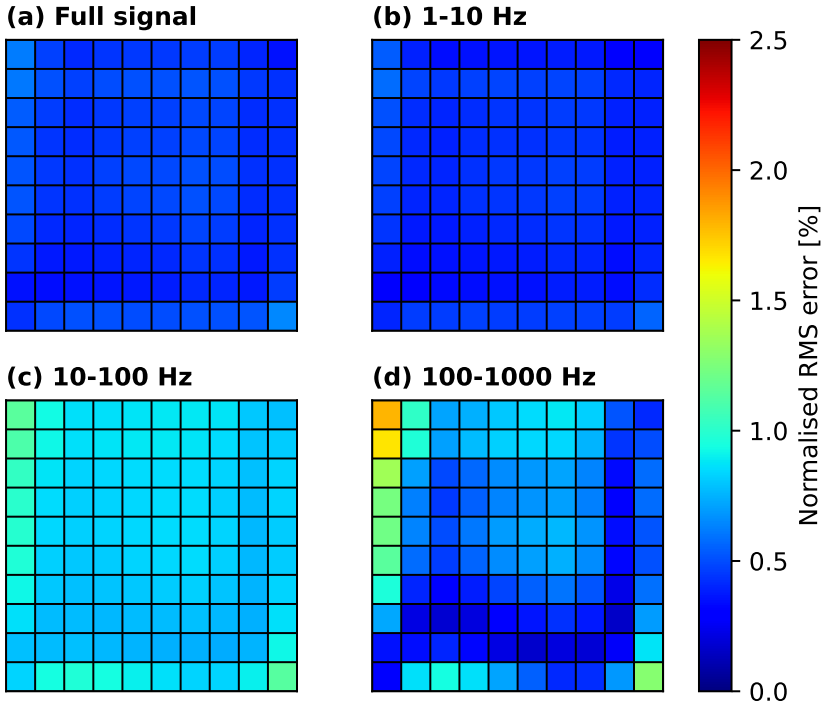

Figure 4.9. Normalised wall temperature fluctuation RMS error with 1000 cells in wall normal direction.

penetration depth when solving the temperature fluctuations directly in the solid domain with a typical LES-CHT mesh (see Section 4.5).

4.7 Multiscale Requirements for Unsteady CHT

As a result of the investigations in this chapter, a number of requirements for building on the method developed by He (2019) to carry out a consistent LES-CHT analysis have been derived:

- The time-average and fluctuating temperatures in the solid domain must be decoupled to allow for the temporal convergence of the solid domain to be accelerated without corrupting the solid domains short timescale response to temperature fluctuations.
- The spectral content of the solid domain must be controlled:
  - Low frequency temperature fluctuations (with a thermal penetration depth that is larger than the solid domain thickness) need to be solved for in the solid domain to allow them to interact with external boundary conditions and geometry.
  - The effect of high frequency temperature fluctuations must be calculated locally on the wall using the wall transfer function approach of (He, 2019). This is so that their thermal penetration depth is not under-resolved, erroneously increasing their amplitude.
- Any solution of the temperature fluctuations within the solid domain must be carried out in the frequency domain to avoid a long-lived steady state error from the causal nature of time marching in solid domain.

- The 1D assumption is valid within the semi-analytical wall function approach. This approach should be reformulated to increase its computational efficiency and to reduce prior knowledge of the flow needed to use it.

Although these requirements have been arrived at following consideration of the flows in rotating cavities, they are relevant to many other applications where LES-CHT can be used to provide useful insights - for instance, in blade and vane heat transfer (Duchaine et al., 2009; He, 2019), internal cooling flows (Oh et al., 2021; Scholl et al., 2016), combustion (Agostinelli et al., 2021; Shahi et al., 2015), or thermal fatigue (Timperi, 2014).

Developing an LES-CHT framework that meets the above requirements will allow the affordable and consistent solution of all scales present in a steady state LES-CHT analysis, including low frequency temperature fluctuations from large-scale coherent structures and chaotic high frequency temperature fluctuations caused by turbulence.

Chapter 5

A Multiscale Framework for LES-CHT

5.1 Aims of the Multiscale Framework

Calculating a time-accurate quasi-steady state unsteady CHT solution is extremely difficult. There are two reasons for this: the first is that the characteristic timescale of the solid domain is four orders of magnitude larger than that of the fluid domain He and Oldfield (2011). It has been widely acknowledged for some time that this presents significant challenges in driving out the initial transient in the solid domain; we showed in the last chapter that this issue also arises even when solving for temperature fluctuations decoupled from the time averaged state, a fact that has previously been under-appreciated in the CHT literature. The second issue is that under-resolving the thermal penetration depth in the solid domain causes an over-prediction in the amplitude of wall temperature fluctuations, potentially making frequencies of thermal unsteadiness are not be dynamically important if correctly resolved affect the solution. The analysis in Fig. 4.6 showed that between 3 and 4 cells are necessary within the thermal penetration depth to prevent this - with LES time steps this would make the

solid domain wall-adjacent mesh finer than the fluid domain, an unaffordable cost.

These factors combine to mean that solving for any temperature fluctuation directly in a time-marching solid domain is incompatible with consistently calculating accurate unsteady CHT solutions. The only methodology that goes some way to addressing this is the closely coupled LES-CHT method of He (2019), which uses a frequency domain semi-analyitcal wall transfer function to accurately deal with broadband thermal unsteadiness, as outlined in Section 4.3.

For application to rotating cavity flows (and many other flows with large scale thermal unsteadiness), the approach of He (2019) is limited by the semi-infinite assumption made in the derivation of the wall transfer function. The low frequency temperature fluctuations caused by these flow structures may be at a frequency where the thermal penetration depth is larger than the solid domain thickness so that non-local interactions with external boundary conditions and the solid domain geometry can occur. There are no existing methods that are able to consistently deal with this timescale of temperature fluctuation. This means that a new methodology account for this timescale of unsteadiness needs to be developed to have a framework that is able to deal with all scales of unsteadiness that are present in unsteady CHT computations with LES.

An additional challenge with the implementation of the wall transfer function in He (2019) is that choosing the number of harmonics and their frequencies is difficult without prior knowledge of the flow. Large numbers of harmonics must be stored on the interface to properly represent the time trace of T'', increasing both computational costs and memory requirements. It is therefore of interest to reformulate the transfer function approach to require less user input and judgement/prior knowledge of the flow, enabling easier uptake by the community.

5.2 Timescale Decomposition and Scale Separation

The unsteady temperature T, and wall adjacent heat transfer coefficient h_f are split into three separate timescales with the triple decomposition used by Reynolds and Hussain (1972):

$$\psi = \widetilde{\psi} + \psi' + \psi'', \tag{5.1}$$

where $\widetilde{\psi}$ is the average of the generic variable ψ, and ψ' and ψ'' are the coherent low frequency and turbulent, chaotic higher frequency temperature fluctuations. The range of frequencies that each fluctuation occupies is case dependent. This is shown applied to the rotating cavity LES unsteady temperature trace from Fig. 4.1 in Fig. 5.1.

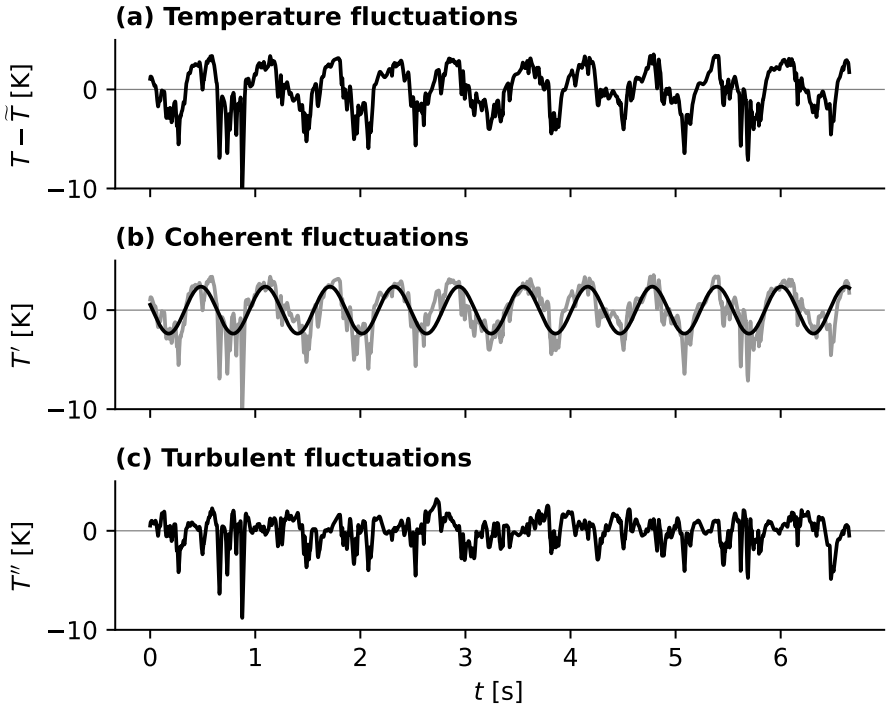

Figure 5.1. Triple decomposition applied to the temperature trace in Fig. 4.1. Full temperature fluctuations shown in grey in (b) for context.

Different frequencies of thermal unsteadiness require different methods to capture

them. The coherent low frequency temperature fluctuations (T') are to be accounted for using a time-spectral (i.e. frequency domain) solution of the temperature fluctuations within the solid domain. This will allow their 3D interactions to be captured while avoiding contamination from the initial transient that would arise if they were solved for in the time domain. The effect of the chaotic high frequency temperature fluctuations (T'') is to be captured using wall transfer function approach reformulated to require less user input and a-priori knowledge of the flow.

The mean values of relevant variables (including temperature) in the interface-adjacent fluid cells are updated at each time-step using a straight forwards recursive moving average. At time-step $M+1$:

$$\widetilde{\psi}_{M+1} = \frac{1}{M+1}\psi_{M+1} + \frac{M}{M+1}\widetilde{\psi}_{M}. \tag{5.2}$$

The effect of initial transients on the moving average can be reduced by simply resetting M to a new, smaller value (He, 2019).

The scale separation problem - decomposing the unsteady temperature into its long and short timescales without introducing a phase lag that destroys the time accuracy of the solution - is challenging. To do this, we use a DFT - this will only take components of T at the frequencies of the harmonics used to calculate it, filtering out T'' and leaving only the low frequency coherent components of the signal remaining.

To remove the need to store a long temperature history on the interface, we need to use recursive methods to calculate the DFT. The sliding DFT with partial substitution (He (1992); reproduced in Eq. (4.11)) was tested for this purpose, however it was ultimately opted against. When ω_0 was set to be the frequency of radial arm passing; the harmonics would not converge to a stable value, causing spurious high frequency

noise in the low-pass filtered signal reconstructed from them. Although this could be overcome by setting ω_0 to a sub-harmonic of the radial arm passing frequency, this meant that it took several radial arm passing periods to converge the harmonics, essentially reintroducing another initial transient - although this does not corrupt the steady state solution in the same way as a time domain initial transient.

Instead, it was chosen to converge the harmonics to stable values in a manner that is consistent with the moving average. They are therefore updated according to

$$\begin{cases} A_{n,M+1} = \dfrac{2}{M+1}\cos(n\omega_0 t)\left(T - \widetilde{T}\right)_{M+1} + \dfrac{M}{M+1}A_{n,M} \\ B_{n,M+1} = \dfrac{2}{M+1}\sin(n\omega_0 t)\left(T - \widetilde{T}\right)_{M+1} + \dfrac{M}{M+1}B_{n,M} \end{cases}, \tag{5.3}$$

where A_n and B_n are real valued coefficients of the n^{th} cosine and sine harmonics respectively. This formula can be simply derived from the definition of the DFT, and was used in Hickling and He (2023). The values of the fluid harmonic coefficients, A_f and B_f, are continuously updated at every time step to prevent aliasing of the signal, an important issue with loosely coupled approaches (Jaure et al., 2013). Given values for the harmonics, the low frequency coherent temperature fluctuation T' can be reconstructed in the time domain using a Fourier expansion with N harmonics and base angular frequency ω_0 as

$$T'(t) = \sum_{n=1}^{N} A_n \cos(n\omega_0 t) + B_n \sin(n\omega_0 t), \tag{5.4}$$

Once $\widetilde{T}$ and T' are known, the high frequency temperature fluctuations T'' can be calculated by rearranging Eq. (5.1).

5.3 Time-Average Solid Domain Solution

Applying the temperature decomposition in Eq. 5.1, neglecting the high frequency fluctuations, and assuming that the solid domain properties are only governed by the time-average temperature, the unsteady energy equation

$$\frac{\partial}{\partial t}\left(\rho_s c_s T\right) = \nabla \cdot \left(k_s \nabla T\right), \tag{5.5}$$

can be separated out into its time-average component

$$\frac{\partial \widetilde{T}}{\partial \tau} + \nabla \cdot \left(\widetilde{k}_s \nabla \widetilde{T}\right) = 0, \tag{5.6}$$

and its low frequency fluctuating component

$$\frac{\partial}{\partial t}\left(\widetilde{\rho}_s \widetilde{c}_s T'\right) = \nabla \cdot \left(\widetilde{k}_s \nabla T'\right). \tag{5.7}$$

The time-average Eq. 5.6 can be solved by marching in pseudo-time (τ) at a large but stable time step. As long as an accurate time-average boundary condition is available, this removes the need to simulate the solid domain throughout the duration of the long initial transient.

The interface condition between the time-average solid domain and the fluid is calculated using the closely coupled moving-average interface condition as in He (2019). This interface condition, derived from the time averaging the 1D interface balance used in Eq. 4.5 to enforce time-average energy balance and temperature

continuity at every time-step, is given by

$$\widetilde{T}_{w,M+1} = \left(\frac{\widetilde{h_f T_f} + \widetilde{h}_s \widetilde{T}_s - \widetilde{h'_f T'_w}}{\widetilde{h}_f + \widetilde{h}_s} \right)_M . \tag{5.8}$$

5.4 Time-Spectral Solid Domain Solution

5.4.1 Time-Spectral Solution for Unsteady Conduction

The unsteady equation needs more treatment to remove the effect of the initial transient and for us to control the spectral content of the solid domain so that the solution is not contaminated by unresolvable frequencies. Substituting the Fourier expansion in Eq. (5.4) into the solid domain temperature fluctuation equation (Eq. (5.7)) and evaluating it at two phase-angles ($n\omega_0 t = 0$ and $n\omega_0 t = \pi/2$) yields a time-spectral equation for the nth harmonics of the unsteady solid domain as

$$\begin{cases} \dfrac{\partial A_n}{\partial \tau} &= \nabla \cdot \left(\widetilde{k}_s \nabla A_n \right) - n\omega_0 \widetilde{\rho}_s \widetilde{c}_s B_n \\ \dfrac{\partial B_n}{\partial \tau} &= \nabla \cdot \left(\widetilde{k}_s \nabla B_n \right) + n\omega_0 \widetilde{\rho}_s \widetilde{c}_s A_n \end{cases} . \tag{5.9}$$

Solving an unsteady solid-domain in this manner was used by He and Oldfield (2011) for validation of the wall transfer function, and has also been used by Mehdizadeh et al. (2017) with a non-linear harmonic solver. Being in the frequency domain, the time-spectral solution method allows the correct quasi-steady state low frequency temperature fluctuations in the solid domain to be calculated instantaneously provided that accurate boundary conditions for the harmonics are available. LES is an intrinsically time domain approach, so a method of interfacing a time-spectral solid domain and a time-marching fluid domain is needed.

5.4.2 Harmonic Balance Interface Condition

To interface the time-spectral solid and time-marching fluid, a harmonic balance is combined with the closely coupled interface of He (2019). The time-spectral solid wall temperature harmonics for the next time step are calculated from

$$\begin{cases} A_{w,M+1} &= \left(\dfrac{\widetilde{h}_f A_f + \widetilde{h}_s A_s}{\widetilde{h}_f + \widetilde{h}_s} \right)_M \\ B_{w,M+1} &= \left(\dfrac{\widetilde{h}_f B_f + \widetilde{h}_s B_s}{\widetilde{h}_f + \widetilde{h}_s} \right)_M \end{cases}, \tag{5.10}$$

where the values of A_f and B_f are obtained using Eq. 5.3.

The time-mean and time-spectral solid domains are only coupled in 1 direction: the time-mean properties (that depend on $\widetilde{T}$) feature in Eq. 5.9, but fluctuating variables or harmonics do not feed back into the time-mean state in Eq. 5.6. This lack of coupling means that an arbitrary number of harmonics can be solved in the solid domain without complicating the approach. The time-spectral solid solution was used with LES in Hickling and He (2023), and its inclusion in the framework fills an important spectral gap in existing methods for carrying out LES-CHT.

5.5 A Reformulated Wall Transfer Function

5.5.1 Motivation for Using Recursive Convolution

Our aim for this part of the framework is to preserve to spirit of the frequency domain wall transfer function approach as used for LES-CHT by He (2019), while reducing the memory requirements of the method and removing the need for the user to judge how many and what frequency range of harmonics to include.

A class of mathematical methods that have had success at this kind of problem within the computational aero-acoustics community are the recursive convolution-type methods as used by Fung and Ju (2001); Shur et al. (2021). To use these we start in the same place as He (2019), with the frequency domain representation of the reciprocal of the T-q transfer function derived from consideration of a 1D semi-infinite solid domain as:

$$\frac{1}{\widehat{C}_{Tq}} = \frac{\widehat{T}_w}{\widehat{q}} = \frac{1}{\sqrt{\rho_s c_s k_s}} \frac{1}{\sqrt{i\omega}}. \tag{5.11}$$

As discussed in Section 4.3, in He (2019) this was used with a discrete expression for the wall heat flux to calculate the wall temperature fluctuation through multiplication in the frequency domain - we aim to use the equivalent operation, convolution in the time domain.

5.5.2 Rational Approximation of $1/\widehat{C}_{Tq}$

Equation 5.11 contains a fractional order term ($\sqrt{\omega}$) that is difficult to use recursive convolution methods with. We approximate the offending term with the sum of P first order real-pole transfer functions:

$$\frac{1}{\sqrt{i\omega}} \approx \sum_{p=1}^{P} \frac{A_p}{i\omega + \lambda_p}. \tag{5.12}$$

This has poles $-\lambda_p$, and residues A_p. λ_p is kept positive to ensure stability of transfer function. It is possible to include complex poles in this approximation (and in the recursive convolution approach we adopt later), but we do not — diffusive processes such as heat transfer are non-oscillatory, so their transfer functions do not have resonant peaks. It is interesting to note that using this sort of approximation for the T-q transfer function is not new - analogue electrical circuits (or "filter-networks") with the same mathematical form as Eq. (5.12) were used for online processing of heat-flux

data from surface temperature measurements as far back as the 1960s (Schultz and Jones, 1973).

The approximation in Eq. (5.12) is fitted to $1/\sqrt{i\omega}$ by logarithmically spacing λ_p out over the range of frequencies of relevance to the simulation and choosing A_p to minimise the magnitude-weighted least-squares error in both the real and imaginary parts. Even with a large number of sample points (e.g. 2048) this procedure is almost instantaneous, and only needs to be carried out once per simulation. It is simple to extend this approximation approach to more complex transfer functions such as those involving a thermal barrier coating (He, 2019) and to use more advanced fitting methods such as fast vector fitting (Gustavsen and Semlyen, 1999), or nonlinear regression.

The largest pole (λ_P) was set to be $2/\Delta t_f$ to ensure a good coverage of the highest frequencies of the response. This is possible as the method was implemented in an implicit flow solver with an unconditionally stable time stepping method; if using an explicit solver, λ_P would be chosen to be as large as possible while still maintaining stability in the recursive convolution. Similarly, for the smallest pole (λ_1), a good choice is the frequency corresponding to a timescale that is an order of magnitude longer than the approximate runtime of the simulation - e.g. if one is expecting to carry out on the order of 10^4 time steps, then $f_{min} = 10^{-5}/\Delta t_f$.

The Bode plot of an approximate (with $P = 6$) and analytical $1/\widehat{C}_{Tq}$ is shown in Fig. 5.2 for an Epoxy solid and Δt_f the same as the standalone LES computations earlier in the paper. The rational approximation of the transfer function agrees extremely well with the exact value, even with this small number of poles: as shown in Fig. 5.3 the largest error in $|1/\widehat{C}_{Tq}|$ is 7% and occurs at the extremes of the frequency range, where it is not much of an issue (the highest frequencies are corrupted by the

discretisation effects in the fluid domain, and the lowest should not be excited within the present framework).

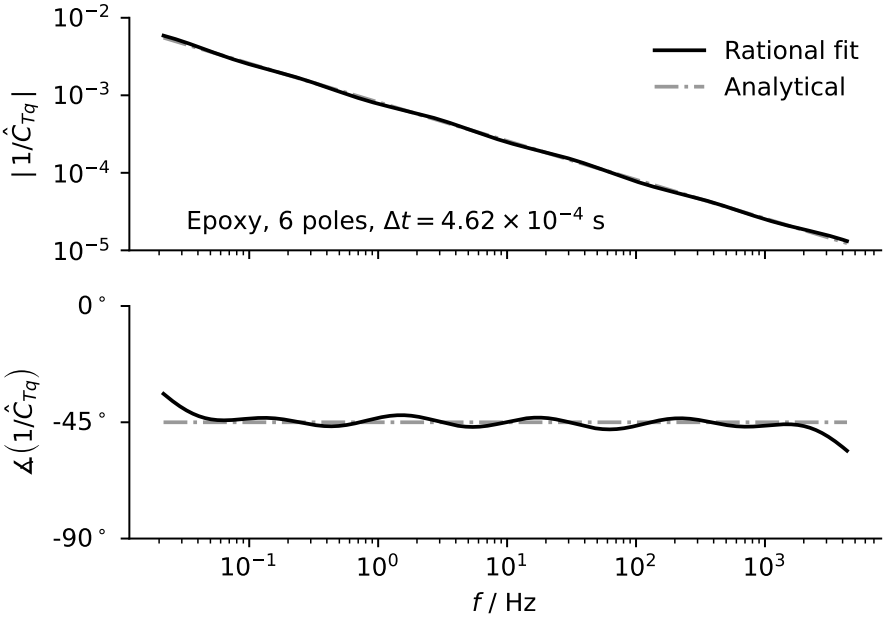

Figure 5.2. Bode plot comparison of $1/\hat{C}_{Tq}$ and its rational approximation.

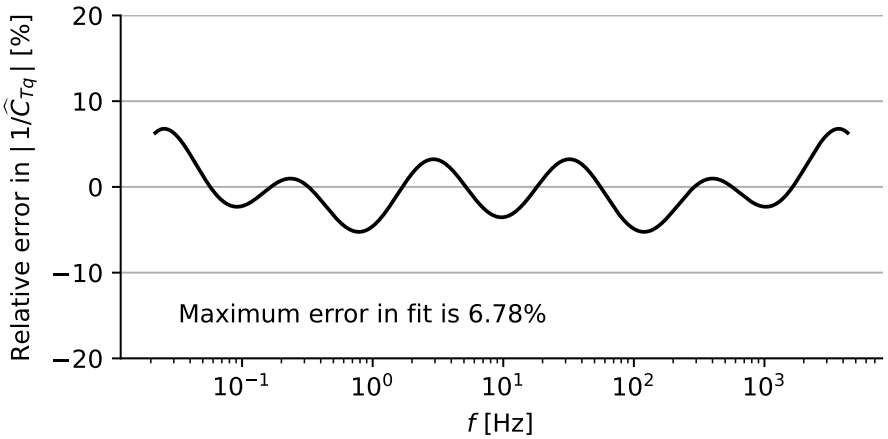

Figure 5.3. Relative amplitude error when rationally approximating $|1/\widehat{C}_{Tq}|$ with 6 poles.

5.5.3 Recursive Convolution with Auxiliary Differential Equations

To carry out the recursive convolution, we use the auxiliary differential equation (ADE) method of Dragna et al. (2015). This method has been used successfully with

turbulence resolving methods in Shur et al. (2021) to model the acoustic response of a duct liner. For a full description of the derivation of ADEs, the reader is referred to Dragna et al. (2015).

Defining P ADEs (with solution $\psi_p(t)$, the p^{th} auxiliary function) as

$$\frac{d\psi_p}{dt} = q''(t) - \lambda_p \psi_p(t), \tag{5.13}$$

T''_w can be calculated from

$$T''_w(t) = \text{IFT}\left(\frac{1}{\widehat{C}_{Tq}}\right) * q''(t) \approx \frac{1}{\sqrt{\rho_s c_s k_s}} \sum_{p=1}^{P} A_p \psi_p(t), \tag{5.14}$$

where IFT is the inverse Fourier transform.

It is desirable to base the solution on wall-adjacent cell-centre temperature fluctuation T''_f, and not q'' to maintain consistency with the Dirichlet-Dirichlet style coupling of the fluid and time average/spectral solid domains. This also avoids potentially awkward dependencies on the solver gradient calculation.

Expressing the heat flux q'' using in terms of T''_f and T''_w gives

$$q'' = \widetilde{h}_f \left(T''_f - T''_w\right), \tag{5.15}$$

where, by re-arranging Eq. (5.1), T''_f is calculated from

$$T''_f = T_f - \widetilde{T}_f - T'_f. \tag{5.16}$$

An advantage of the ADE method is that the ADEs can be solved by stepping in time in a way that is fully consistent with the flow solver. In an implicit code using second

order backwards differencing (consistent with the LES and LES-CHT computations in this paper),

$$\frac{d\psi_p}{dt} \approx \frac{3\psi_{p,M} - 4\psi_{p,M-1} + \psi_{p,M-2}}{2\Delta t_f}. \tag{5.17}$$

Combining Eqs. 5.15 and 5.17 gives

$$\left(1.5 + \lambda_p \Delta t_f\right) \psi_{p,M} + \widetilde{h}\Delta t_f T''_{w,M} = \widetilde{h}\Delta t_f T''_{f,M} + 2\psi_{p,M-1} - 0.5\psi_{p,M-2}. \tag{5.18}$$

Along with Eq. 5.14 this forms a small, sparse $(P+1) \times (P+1)$ linear system in the form $\mathbf{Ax} = \mathbf{b}$, where

$$\mathbf{A} = \begin{bmatrix} 1.5 + \lambda_1 \Delta t & 0 & \cdots & 0 & 0 & \widetilde{h}\Delta t \\ 0 & 1.5 + \lambda_2 \Delta t & & 0 & 0 & \widetilde{h}\Delta t \\ \vdots & & \ddots & & \vdots & \vdots \\ 0 & 0 & & 1.5 + \lambda_{P-1}\Delta t & 0 & \widetilde{h}\Delta t \\ 0 & 0 & \cdots & 0 & 1.5 + \lambda_P \Delta t & \widetilde{h}\Delta t \\ -A_1 & -A_2 & \cdots & -A_{P-1} & -A_P & 1 \end{bmatrix}, \tag{5.19}$$

$$\mathbf{x} = \begin{Bmatrix} \psi_1 \\ \psi_2 \\ \vdots \\ \psi_{P-1} \\ \psi_P \\ T''_w \end{Bmatrix}_M, \tag{5.20}$$

and

$$\mathbf{b} = \widetilde{h}\,\Delta t\; T''_{f,M} \begin{Bmatrix} 1 \\ 1 \\ \vdots \\ 1 \\ 1 \\ 0 \end{Bmatrix} + 2 \begin{Bmatrix} \psi_1 \\ \psi_2 \\ \vdots \\ \psi_{P-1} \\ \psi_P \\ 0 \end{Bmatrix}_{M-1} - 0.5 \begin{Bmatrix} \psi_1 \\ \psi_2 \\ \vdots \\ \psi_{P-1} \\ \psi_P \\ 0 \end{Bmatrix}_{M-2} . \tag{5.21}$$

The system is solved at each coupled face using Gauss-Jordan elimination to get $\psi_{p,M}$ and $T''_{w,M}$ from the values of ψ_p at previous time steps and $T''_{f,M}$ at the current time step. In an iterative implicit solver $T''_{f,M}$ is needed to calculate $T''_{w,M}$. However, $T''_{w,M}$ needs to be set before carrying out an iteration. This is easily addressed by using $T''_{f,M}$ from the previous iteration to calculate $T''_{w,M}$ for the present iteration, so that once the fluid domain has converged at the current time step, so has $T''_{w,M}$.

In an explicit code, this would be simpler; the ADEs can be advanced using data from the current time step/Runge-Kutta stage to give T''_w at the next.

5.5.4 Demonstration of the New Formulation

To validate the new approach for the wall transfer function, the wall temperature fluctuations are computed for the signal in Fig. 4.1 and compared to the analytical frequency domain solution, achieving excellent agreement. This is shown in Fig. 5.4.

The new approach does not require choosing numbers and frequencies of harmonics, as the entire range of timescales that could feasibly be relevant to the problem can be covered economically. It is also memory efficient, requiring the storage of only $2P$ variables per coupled face for the second order implicit time stepping used in this

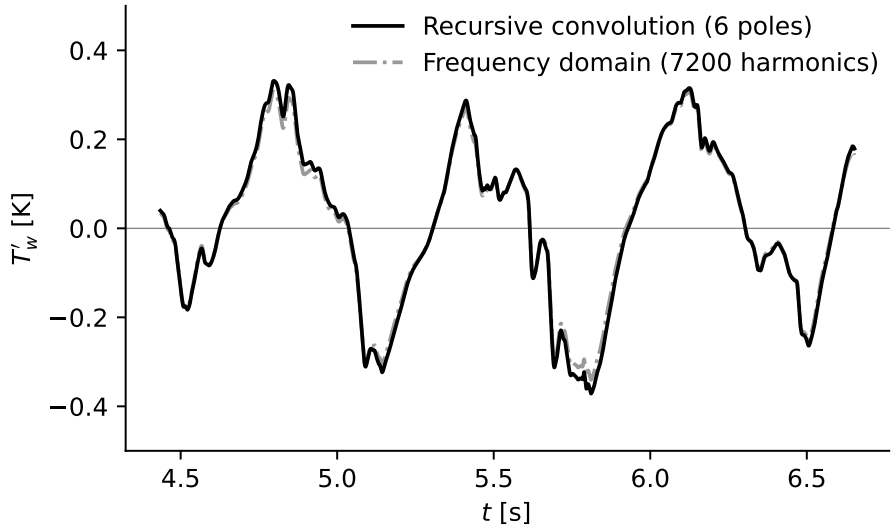

Figure 5.4. Comparison of recursive convolution and analytical results for wall temperature fluctuations.

paper.

Although the recursive convolution happens through the time domain, it does not suffer from the issues seen in Fig. 4.4. This is because we are working from a frequency domain representation of the physics (vs a Laplace domain representation) which means we only capture the fluctuating steady state behaviour of the system, avoiding the issues that come from applying single-sided signals (e.g. $H(t)\sin(\omega t)$). In any case, the recursive convolution based wall transfer function is completely local to the coupled fluid-solid faces, so the issues that arise away from the wall in Fig. 4.4 cannot contaminate other parts of the solid domain.

5.6 Implementation in a Commercial CFD Solver

All aspects of the approach are implemented for the implicit solvers in ANSYS Fluent using the user defined function (UDF) C language programming interface and Scheme

solver macros. ANSYS Fluent is a commercial solver that is popular within both academic and industrial heat transfer communities. The benefit of implementing in a commonly used commercial solver over in-house codes is that, being closed source, it was not possible to change under-lying solver architecture, indicating the readiness for the adoption of the framework into existing workflows. An additional benefit of implementation in a commercial solver is the potential for easy integration of other models going forwards, such as wall-modelling, combustion, and radiation. A flow chart for the multiscale framework in an implicit solver is shown in Fig. 5.5.

The general work flow for using the multiscale framework is as follows:

1. Calculate A_p and λ_p for use in the recursive convolution method.
2. In the CFD solver, time march a directly coupled fluid and solid domain with $\Delta t_s \gg \Delta t_f$ to drive out the initial transient out of the solid domain.
3. Initialise the moving average, DFT, and the ADE variables, as well as the time-average and time-spectral solid domains. The moving average and time-average can be initialised with the instantaneous values for the first time step, and the ADE, DFT, and time-spectral solid domain should be initialised to zero. Apply the appropriate boundary conditions to the fluid and solid domains.
4. Advance the simulations for sufficient time steps to converge the time-average and time-spectral solid domains.
5. Gather statistics and other data for post-processing.

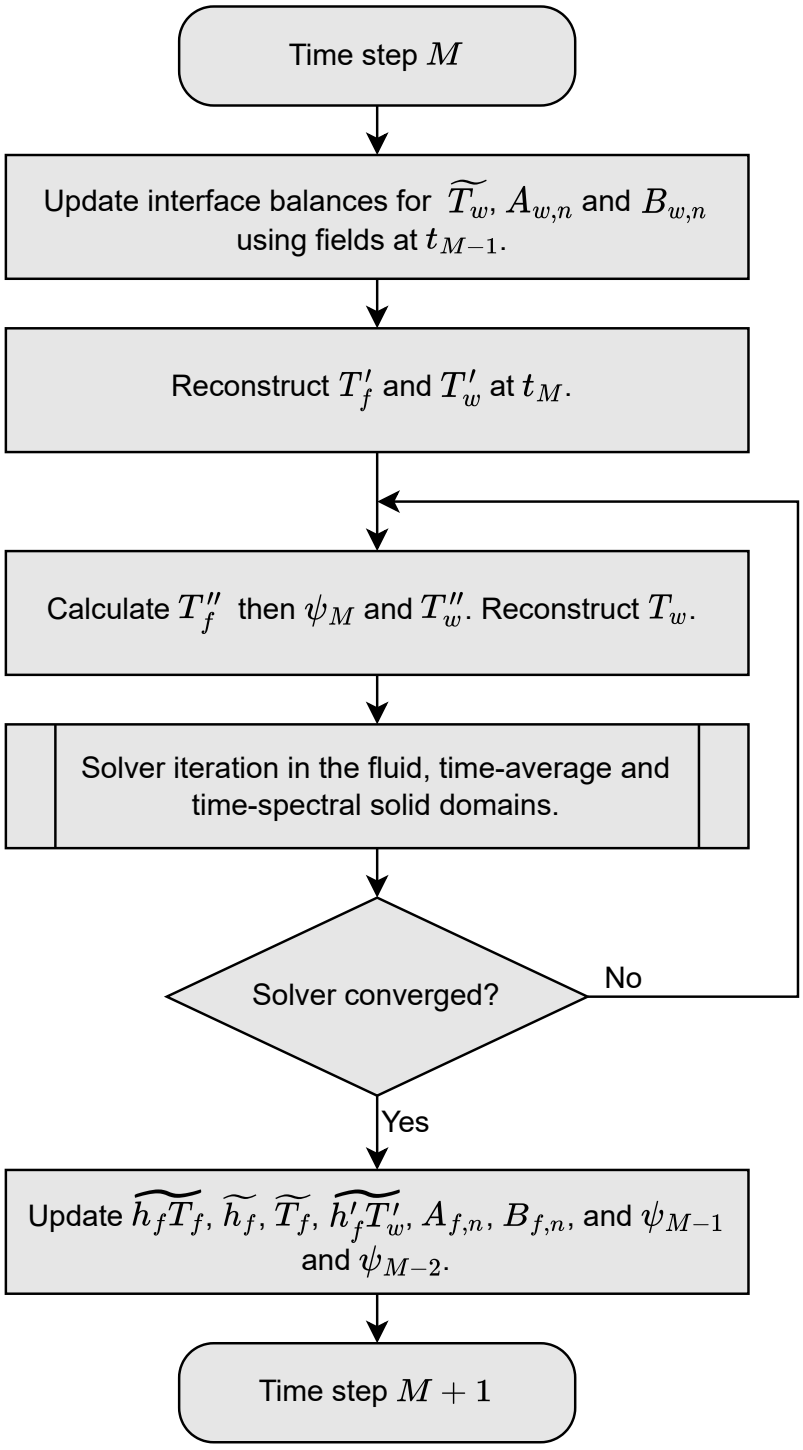

Figure 5.5. Implementation of the multiscale unsteady CHT framework in a flow solver with implicit time stepping.

5.7 Summary of the Multiscale Framework

The multiscale framework developed in this chapter represents the only existing methodology for consistently carrying fully unsteady LES-CHT. This enables the effects of wall temperature fluctuations on the aerodynamics to be calculated or the prediction of the thermal fatigue that they cause. The framework can be summarised as follows:

- The time-average state of the fluid domain and time-average solid domain are coupled at every time-step. This avoids having to drive the initial transient out of the solid domain, which would take an impracticably long time. The time-average state of the fluid domain is updated at each time step using a moving average.
- The low frequency coherent temperature fluctuations from the fluid domain and the time-spectral solid domains are coupled using a harmonic balance interface condition. The value of the harmonics on the fluid side of the interface is calculated using a recursive DFT. If the penetration depth of a coherent temperature fluctuation is too small to capture in the solid domain, it can also be solved on the wall using the frequency domain wall transfer function.
- High frequency turbulent temperature fluctuations are captured using a new recursive convolution based formulation of the wall transfer function.
- The unsteady wall temperature (necessary as a boundary condition for the fluid domain) is reconstructed from the value of the time-average temperature, temperature harmonics on the interface, and the recursive convolution based wall transfer function.

In trying to develop it to be usable in present day CFD tooling, the framework has evolved into a simple add-on to time-average CHT (as carried out by e.g. Scholl et al. (2016)), with a choice of small selectable overheads that can be included or left out depending on the multiscale considerations of the problem at hand. It is worth noting that, although intended for use with turbulence resolving methods, the methodology in this chapter is equally applicable to other types of unsteady flow solution, for example URANS. It is also not rotating cavity specific, and, due to its implementation in commercial CFD software, it could be straightforwardly applied to many other flows where steady state unsteady CHT predictions are of interest. The methodology would also fit well into long timescale computations of rotating cavities, such as those of flight cycles by Atkins (2013) - it could be easily integrated with the source term based approach of Fadl and He (2017); He and Fadl (2017) to provide a framework for turbulence resolved flight-cycle computations, or used as a data source for training reduced order models or enhancements to axisymmetric RANS.

With the drive to decarbonise aviation and power generation, unsteady CHT is likely to become a more important feature of tooling to enable accurate heat transfer predictions (Slotnick et al., 2014). Examples of this are of applications to power electronics cooling (Zhong and Tucker, 2004), novel inherently unsteady conjugate cooling configurations such as those investigated by Mathie and Markides (2013); Zhang et al. (2022), or combustion, where LES-CHT is increasingly being used for simulations of conventional (Agostinelli et al., 2021; Berger et al., 2018; Koren et al., 2017a,b, 2018; Kraus et al., 2018) and alternative fuel (Agostinelli et al., 2022; Mari et al., 2016) burners.

Chapter 6

LES-CHT Computations of Rotating Cavity Flows

6.1 LES-CHT Computations Overview

The multiscale framework developed in the previous section enables LES-CHT simulations of rotating cavities to be carried out for the first time. The purpose of these simulations is two-fold: first, is to demonstrate the efficacy of the newly developed multiscale framework; and second, to investigate the effect of disk material and cavity heating configuration on the aerodynamics within the cavity.

This chapter presents the experimental test case that the LES-CHT simulations are based on and validates the fluid domain modelling approach for this case with standalone LES simulations. The results of the simulated LES-CHT cases are examined to provide evidence on the efficacy of the multiscale framework in four key aspects:

- The interaction of low frequency temperature fluctuations with solid domain geometry and external boundary conditions.
- The similarity of wall temperature fluctuations calculated from the time-spectral solid solution and the frequency domain wall transfer function when the solid the thermal penetration is resolved and the semi-infinite condition is met.
- The advantages of using recursive convolution over harmonics to calculate high frequency wall temperature fluctuations.
- The benefit of the framework over accelerated time marching methods that do not consistently deal with the initial transient or thermal unsteadiness.

6.2 Test Case and Baseline LES

6.2.1 Choice of Test Case

For the computations in this chapter, we remain with the experimental rig of Bohn et al. (2000) at RWTH Aachen, the details of which are given in Section 3.2. In this experiment, 5 mm thick epoxy disks were heated to provide a radially increasing temperature distribution, and the disk heat fluxes and wall temperatures were measured. The computations in this chapter were conducted at the condition shown in Tab. 6.1. This operating condition was chosen to be as high a Grashof number as possible while still having experimental data available for validation - $Gr = 4.86 \times 10^{10}$ corresponds to the highest Grashof number reported by Bohn et al. (2000). The theoretical laminar Ekman thickness at the operating Re_ϕ is

$$\delta_{\mathrm{Ek}} = \frac{\pi b}{\sqrt{Re_\phi}} = 1.40\,\mathrm{mm}. \tag{6.1}$$

Table 6.1. Operating conditions for LES-CHT computations (Bohn et al., 2000).

Parameter		Value
Axial Reynolds number	Re_z	3×10^3
Rotational Reynolds number	Re_ϕ	8×10^5
Buoyancy parameter	$\beta \Delta T_{max}$	0.27
Grashof number	Gr	4.86×10^{10}
Rossby number	Ro	0.121
Angular velocity	Ω	56.67 rad/s

The URANS-CHT simulations of Tian and Zhu (2012) were conducted on this cavity, but they were done at a rotational Reynolds number of 2×10^5. At this operating condition, Tian and Zhu (2012) reported good agreement with experimental data and an improvement in results when URANS-CHT was used instead of URANS, especially at low radii on the downstream disk. Tian and Zhu (2012) also reported fluid only URANS simulations at $Re_\phi = 8 \times 10^5$ and achieved reasonable agreement with the experimental Nusselt number distributions at this condition. This illustrates the suitability of the operating point in Tab. 6.1 for testing the LES-CHT framework.

6.2.2 Fluid Domain Only LES

The LES-CHT simulations used the same solver setup as the previous rotating cavity computations in this thesis. Instead of using an explicit SGS model, the dissipation inherent in the numerical scheme was used to account for sub-grid fluid motions (Margolin and Rider, 2002), making these simulations implicit/numerical LES. The rationale this is to avoid contaminating laminar areas of the flow observed in Chapter 3 with non-physical eddy viscosity. Implicit/numerical LES has been used successfully in rotating cavities before - for example by Onori et al. (2016).

To verify the setup and assess the fluid domain mesh sensitivity at this operating condition, fluid domain only LES simulations were first conducted. Simulations were

conducted on a coarse, medium, and fine mesh to observe the mesh dependency of the solution. The cell counts, wall-normal spacings, and time steps used for each mesh are shown in Tab. 6.2. The medium and fine meshes were initialised from the solution at the previous mesh level. Simulations were run for enough time steps to drive out their initial transients, (90 revolutions for the coarse mesh, 30 revolutions otherwise) and then their statistics were obtained over 30 revolutions. For the fluid domain only simulations, the temperatures on the disks were set to radially vary in the same way as the experimental measurements by Bohn et al. (2000). As no shroud temperature was available, this was set to the average of the two experimental disk temperatures at maximum radius.

Table 6.2. Baseline LES mesh and time step details.

Mesh	Cell count	Δx_w [mm]	Δt per rev.
Coarse	2.4M	0.2	180
Medium	5.1M	0.15	240
Fine	10.2M	0.1	300

All three meshes gave the same large scale flow structure, shown for the medium mesh in Fig. 6.1. The normalised temperature is defined as $T^* = (T - T_{in})/(T_{max} - T_{in})$ and the normalised radial velocity as $V_r^* = V_r/\Omega b$.

The flow structure consists of three circulation pairs that rotate slightly slower than the cavity in the absolute frame of reference. Figure 6.1 clearly shows the transport of cold fluid from the bore to the shroud and of hot fluid from the shroud to the bore by the radial outflow and inflow.

To evaluate the resolution of the meshes in the bulk flow, the power spectral density (PSD) of the resolved turbulent kinetic energy was checked at the cavity's mid-axial mid-radial position (Fig. 6.2). The coarse mesh departs from the inertial range $-5/3$

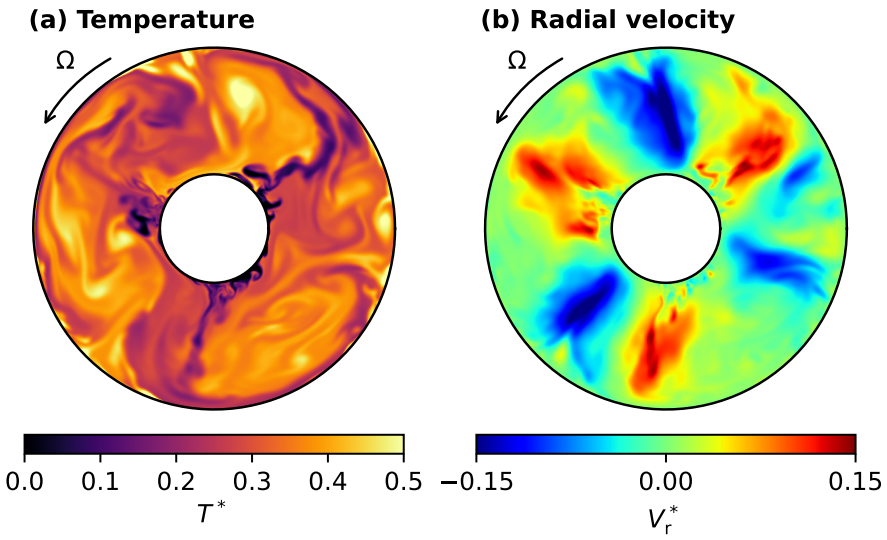

Figure 6.1. Instantaneous cavity mid-plane temperature and radial velocity from fluid domain only LES at $Gr = 4.86 \times 10^{10}$.

fall off at a low frequency of 40 Hz. In contrast, the medium and fine meshes have a similar spectrum until 80 Hz - at this frequency, the PSD of the medium mesh drops sharply, while in the fine mesh it rolls off gradually. This behaviour suggests that both the medium and fine meshes are resolving a significant majority of the inertial range of the turbulent spectrum at this location, and are thus both suitable LES meshes. The lack of a build up in spectral energy at higher frequencies in Fig. 6.2 indicates the presence of sufficient numerical SGS dissipation in the simulations.

Figure 6.3 shows the computed distribution and experimental (Bohn et al. (2000)) of the time- and circumferentially-averaged disk Nusselt numbers, defined as

$$Nu = \frac{qr}{k_{in}(T_w - T_{in})}, \tag{6.2}$$

where q is the wall heat flux, T_w is the wall temperature, and k_{in} and T_{in} are the thermal conductivity and temperature at the cavity inlet. [1]

[1] It is important to remember that this is not a true Nusselt number, but a normalised heat flux.

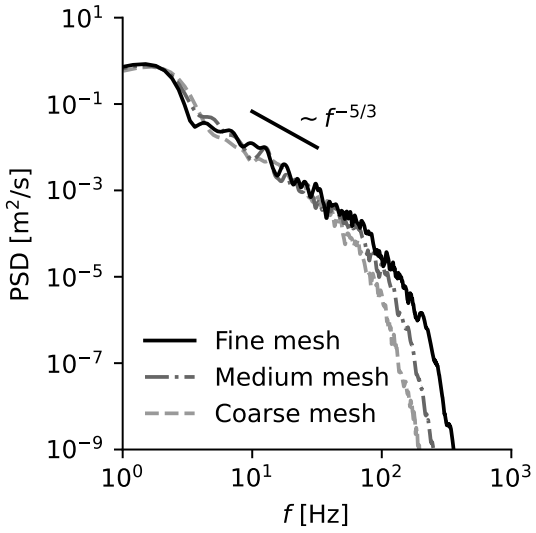

Figure 6.2. Bulk flow turbulent kinetic energy spectra.

In general, the agreement between the computational and experimental data is good and the solution is not sensitive to the mesh resolution, although *Nu* is systematically under-predicted at low radii. On the upstream disk this under-prediction improves when moving from the coarse to the medium meshes, but is very similar between the medium and fine meshes. For both disks, the location of maximum error is at low radii, where the experimental data is most poorly conditioned due to the smallest temperature differences.

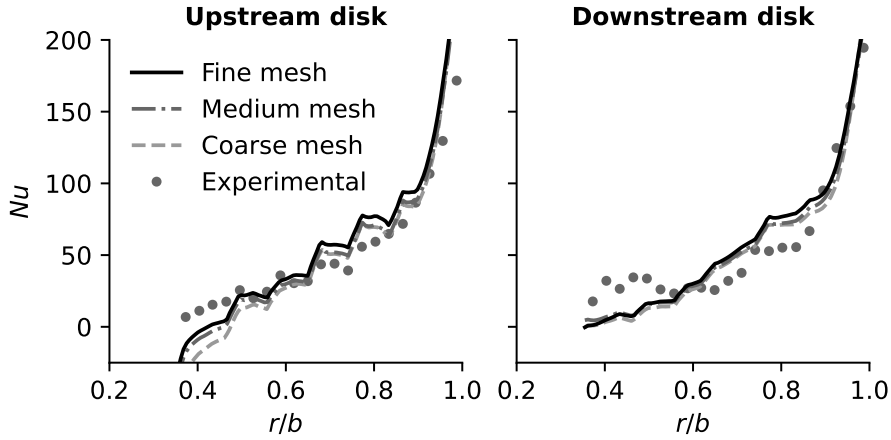

Figure 6.3. Computational and experimental (Bohn et al., 2000) average disk Nusselt numbers at $Gr = 4.86 \times 10^{10}$.

Given that both the medium and fine meshes appear to sufficiently resolve turbulent flow structures inside the cavity, and that there is little difference in Nu calculated on both meshes, all further computations in this chapter use the medium mesh. This mesh had area-averaged normalised wall-normal spacings of $z^+ = 1.26$ on the disk (corresponding to $0.11\Delta_{Ek}$) and $r^+ = 0.72$ on the shroud. The average aspect ratios of the wall normal cells (with the square root of the face area as the wall-parallel length scale) were 22 on the disks and 17 on the shroud. The volume average CFL number for this mesh was 0.4. These values are in line with simulations reported in Chapter 3.

6.3 Case Information

To match the experiments of Bohn et al. (2000), the fluid domain is coupled to an $L = 5$ mm thick solid domain, which is meshed with 10 uniformly spaced cells. The fluid domain mesh and numerical settings were identical to the medium mesh baseline computation shown in Fig. 6.3. LES-CHT simulations were conducted with both axial and radial heating configurations. A diagram of these heating configurations and the external boundary conditions is shown in Fig. 6.4, and a summary of LES-CHT cases is shown in Tab. 6.3.

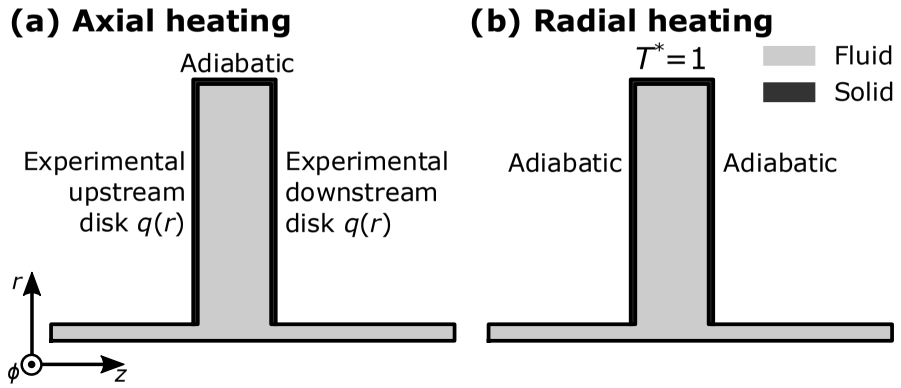

Figure 6.4. LES-CHT boundary conditions corresponding to Tab. 6.3. Inflow and outflow regions have been extended to prevent reverse flow on fluid domain inlets and outlets. Axial throughflow is in the positive z direction.

Table 6.3. Summary of LES-CHT computations using the multiscale LES-CHT framework.

Case	Material	$\delta_p(f_0)/L$	Unsteady wall temperature method	Heating configuration
A	Epoxy	0.16	Transfer function (frequency domain)	Axial
B	Epoxy	-	Transfer function (recursive convolution)	Axial
C	Epoxy	-	None (time-average)	Axial
D	Titanium	0.81	Time-spectral solid	Radial
E	Titanium	0.81	Transfer function (frequency domain)	Radial
F	Nickel	1.92	Time-spectral solid	Radial

The axial heating configuration closely matches the experimental rig of Bohn et al. (2000) and is similar to other experimental configurations, such as Owen and Powell (2006). In this case (Fig. 6.4a), the experimental heat fluxes measured by Bohn et al. (2000) are applied to the external surface of the disks and the exterior of the shroud is left adiabatic. The thermal penetration depth of the radial arm passing frequency (termed $\delta_p(f_0)$ in Tab. 6.1) is small (less than two solid domain cell widths) due to epoxy's low thermal conductivity (0.2 W/mK). As shown by the analysis in Section 4.5, this is insufficient to properly resolve this frequency of thermal unsteadiness. Because the thermal penetration depth can not be resolved, computations on the epoxy/axially heated case use both wall transfer function approaches to enable a comparison of their results. To complement this comparison, a simulation is included that has no treatment of the wall temperature fluctuations - this simulation is still within the multiscale framework; the LES fluid domain is coupled to a time-average solid domain in the manner of Karalus et al. (2020); Scholl et al. (2016)

The radially heated case is more representative of how a rotating cavity would be heated in an aero-engine compressor. In this case (Fig. 6.4b), a normalised temperature of $T_{max} = 378.15\,\mathrm{K}$ (i.e. $T^* = 1$) is applied to the shroud external surface, and the exterior of the disks have an adiabatic condition. Two disk materials are used for the radially heated case - titanium with a medium thermal conductivity (7.3 W/mK), and nickel with a high thermal conductivity (80 W/mK). The titanium disks result in a thermal penetration depth that is smaller than the solid domain thickness, but is still sufficiently resolved by 8 cells. This enables a comparison of wall temperature fluctuations calculated by the frequency domain wall transfer function and by coupling the fluid domain temperature harmonics to the time-spectral solid domain solution. In the nickel case, the thermal penetration depth is almost twice the solid domain width; this means that non-local interactions with external boundary conditions and cavity

geometry are possible and it is necessary to use the time-spectral transfer function.

It is worth highlighting that the non-dimensional conditions are the same for all LES-CHT cases, the only difference is the heating configuration used to reach T_{max}.

6.4 LES-CHT Solution Process

All LES-CHT cases proceeded by time-marching both the solid and fluid domains in a desynchronised fashion with $\Delta t_s = 10,000 \Delta t_f$ for 30 revolutions to drive out the initial transient. Then, 10 revolutions of this desynchronised time-marching were used to calculate values to initialise the moving average, DFT, and ADE variables. Data gathered from numerical sensors placed near the disks in this period was used to calculate a value for ω_0 for the DFT and time-spectral solid domain. Only one Fourier harmonic (at ω_0) was used with the frequency based wall transfer function or time-spectral solid domain. The recursive convolution based wall transfer function uses the 6 pole approximation shown in Figs. 5.2 and 5.3, this reproduces the frequency response from the frequency domain semi-analytical wall transfer function to within 7%.

The boundary conditions were then changed to the time-mean and harmonic balance conditions and the flow was solved for 20 revolutions. A pseudo time-step of $10,000 \Delta t_f$ was used for the time-mean solid domain, and a pseudo time-step of $100 \Delta t_f$ was used for the time-spectral domain. Finally, flow-field statistics were collected for a further 30 revolutions.

The value for the solid time-step Δt_s in the initial steps of the solution process was chosen to approximately equalise the characteristic fluid and solid time-scales as

discussed in Chapter 4. As implicit time-stepping is used, there are no stability considerations for choosing Δt_s; if explicit time-stepping was to be used then it would be chosen to be as large as possible while preserving stability.

6.5 LES-CHT Results

Before demonstrating the efficacy of the framework developed in Chapter 5, a top-level overview of the results of the cases in Tab. 6.3 is presented. Figure 6.5 shows the time- and circumferentially-averaged disk temperature and Nusselt number for each of the materials; separate lines have not been shown for each of the different wall temperature methods used for epoxy in Tab. 6.3, as the values were close enough to be indiscernible.

The results for the axially heated epoxy disk case in Fig. 6.5 can be used as an experimental validation of the multiscale framework due to the similarity to the experimental rig of Bohn et al. (2000). In terms of the Nusselt number, the agreement with experimental data is very good, and the wall temperature is reasonably well-matched given that it was not possible to include every conduction path in the test rig in the computational geometry. It is interesting to note that agreement of the Nusselt numbers with experimental data in the LES-CHT computation that best represents the test rig is significantly better than the fluid domain only case; and that even the radially heated case that retains a significant amount of disk heating (nickel disks) matches the experimental Nusselt numbers well.

The results for the two radially heated metal cases are quite different. The titanium cavity has significantly lower disk temperatures than the nickel cavity and has a region of strong curvature around $r/b = 0.85$ that is not present in the nickel results. The

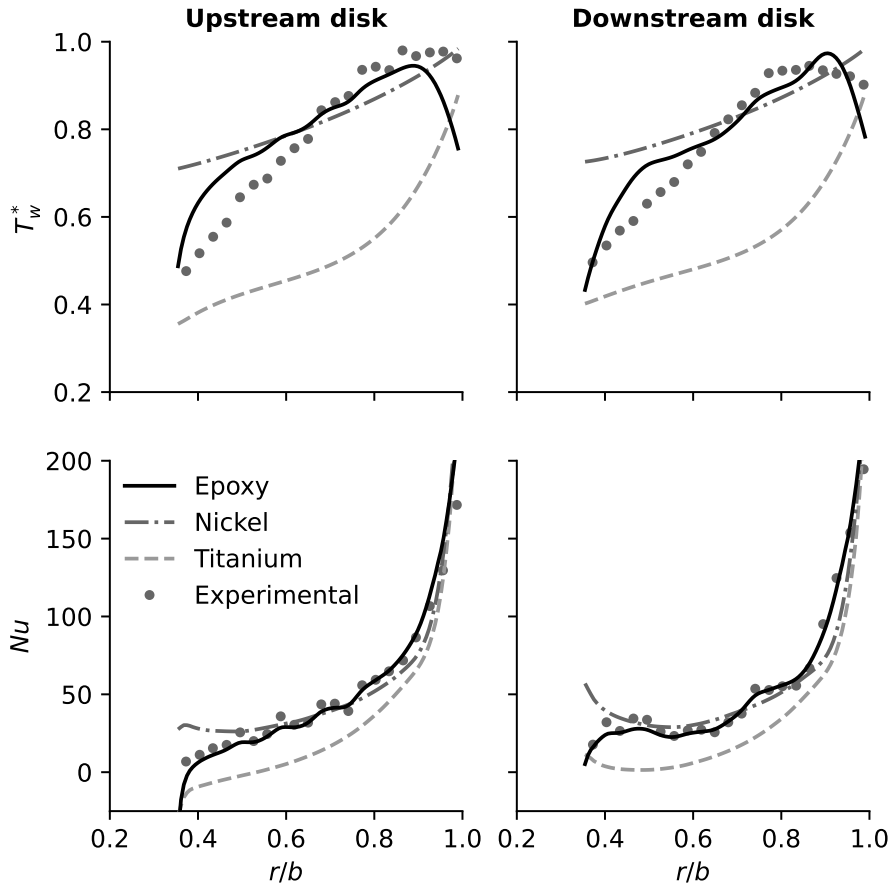

Figure 6.5. Average wall temperature and Nusselt number from the LES-CHT simulations. (Experimental data from Bohn et al. (2000).)

difference in disk temperature also manifests itself in the distribution of the Nusselt number, which is consistently lower for the titanium case than the nickel one. This is most stark on the upstream disk, where the "cool" fluid inside the cavity has a net-heating effect on the titanium disk at low radii, giving regions of negative heat flux.

All simulations gave the same three circulation pair large scale flow structure as the baseline fluid only computations. This is shown in Figs. 6.6 to 6.8.

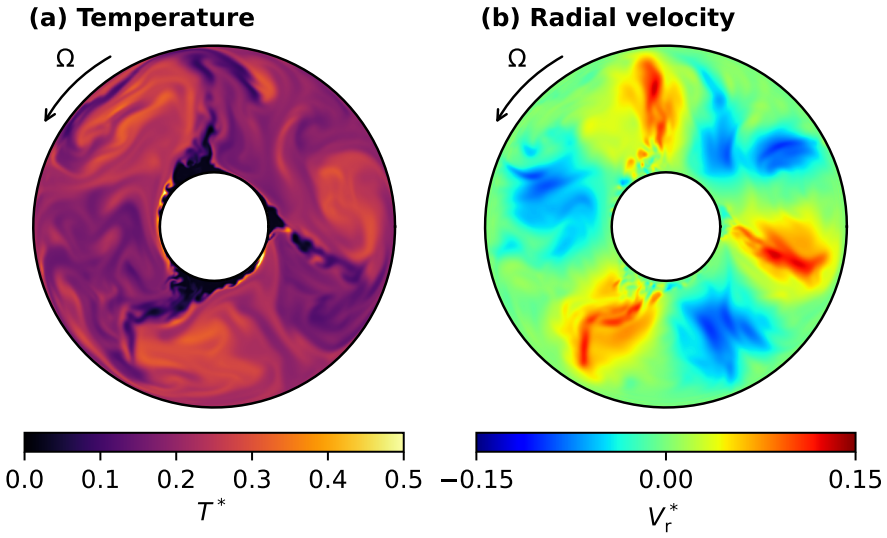

Figure 6.6. Instantaneous cavity mid-plane fluid temperature and radial velocity. (LES-CHT case A: epoxy with frequency domain transfer function.)

Given the similarity in disk temperature and Nusselt number in Fig. 6.5 between the axially heated epoxy cavity and the radially heated nickel cavity, the reader may be surprised at the difference in mid-plane temperature in Figs. 6.6a and 6.8a, and by the less intense radial arms in Fig. 6.6b compared to Fig. 6.8b. This has been explained for a similar situation by Hickling and He (2023), and will be investigated further in the next chapter: in short, shroud heating is more efficient at heating the fluid inside the cavity due to the relative lack of wall-normal velocity fluctuations near the disks compared to the shroud.

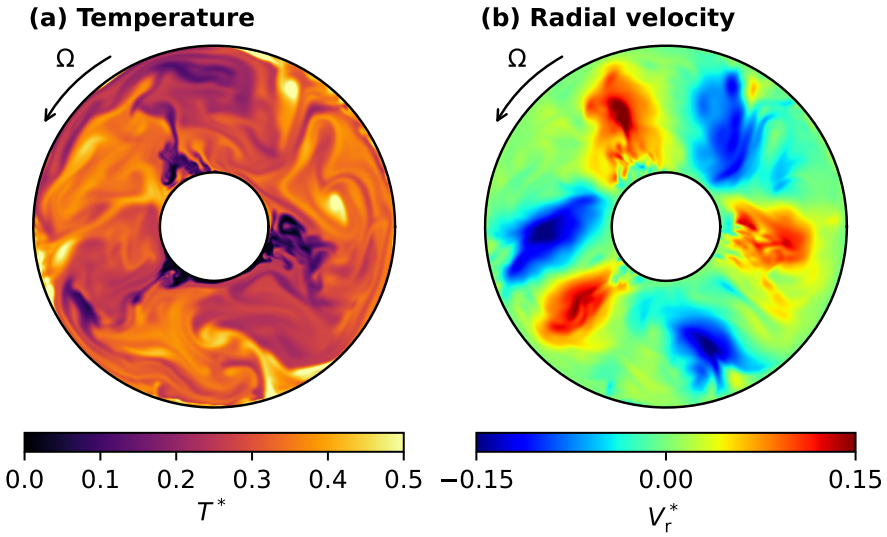

Figure 6.7. Instantaneous cavity mid-plane fluid temperature and radial velocity. (LES-CHT case D: titanium with time-spectral solid domain solution.)

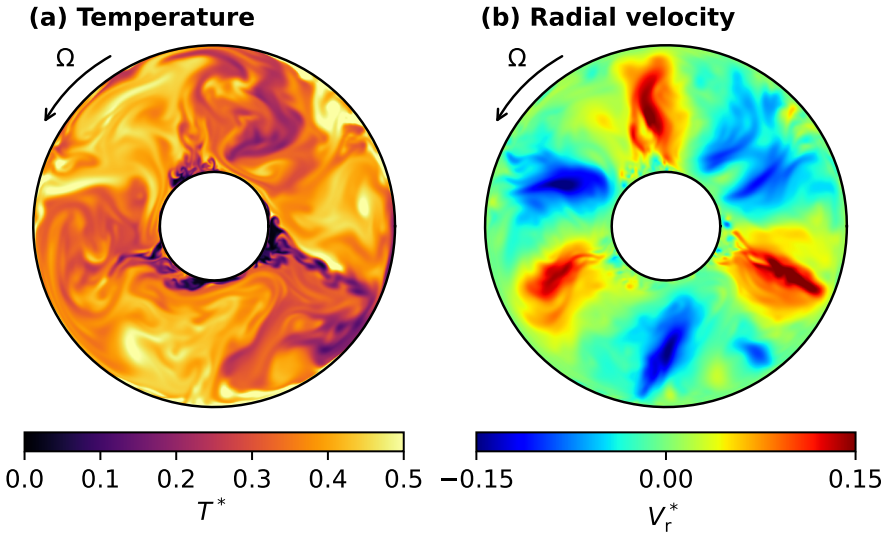

Figure 6.8. Instantaneous cavity mid-plane fluid temperature and radial velocity. (LES-CHT case F: nickel with time-spectral solid domain solution.)

6.6 Multiscale Framework Case Studies

The aim of this section is to demonstrate the benefit of the newly developed multiscale approaches over approaches that do not consistently deal with the multiscale nature of LES-CHT. To show the functionality of the time-spectral solution, the penetration of wall temperature fluctuations through the disks and to the exterior disk boundary is illustrated. Wall temperature functions from both the titanium and epoxy cases are compared, serving two purposes: to demonstrate the consistency of the time-spectral and wall transfer function approaches when the semi-infinite condition is met and to show the advantage of using recursive convolution over discrete harmonics to calculate high frequency wall temperature fluctuations. Finally, the issues that arise with time-marching LES-CHT approaches (as seen in Section 4.4.2) will be shown.

6.6.1 Through-Disk Penetration of Temperature Fluctuations

The motivation for developing the time-spectral solid domain solution approach was to enable low frequency temperature fluctuations from large-scale coherent structures to interact with the solid domain boundary conditions and geometry in a consistent manner.

The temperature fluctuation harmonic coefficients from the nickel case are shown on the downstream disk in Fig. 6.9, and their distribution within the disk at the mid-radial (r/b = 0.269) position at the 12 o'clock position is shown in Fig. 6.10. Due to the low thermal diffusivity of nickel, the wall temperature fluctuations penetrate through the disks and interact with the boundary conditions on the other side, proving the need for time-spectral solid domain solution in certain scenarios. A comparison with a 1D analytical (not semi-infinite) solution of the conduction using the same boundary

conditions as the LES-CHT simulation gives an identical distribution of the harmonics, verifying the implementation of this component of the framework.

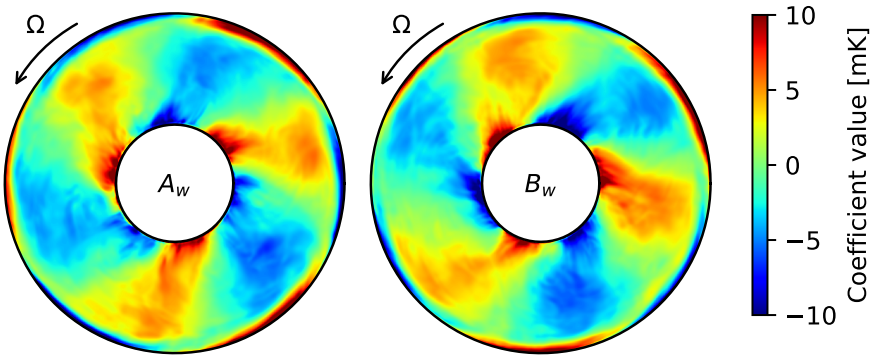

Figure 6.9. Wall temperature harmonic coefficients A_w and B_w on the downstream disk. (Case A: Nickel with time-spectral solid domain solution.)

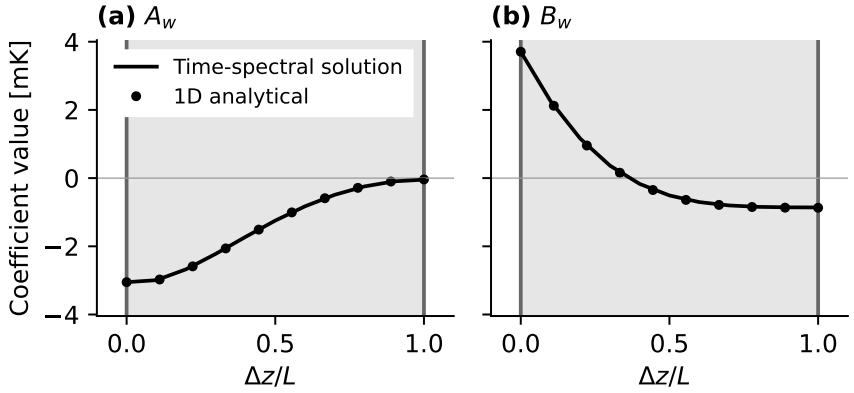

Figure 6.10. Nickel disk internal temperature harmonics at $r/b = 0.269$. Fluid-solid interface is at $\Delta z/L = 0$ and the adiabatic external boundary condition is at $\Delta z/L = 1$.

6.6.2 Calculation of Wall Temperature Fluctuations ($\delta_p \approx L$)

To complement the analysis in Section 4.6 and further demonstrate the validity of the 1D assumption made in the derivation of the T-q transfer function, we investigate the titanium case. The solid domain mesh is able to resolve δ_p well enough to use the time-spectral solid domain (case D in Tab. 6.3). $\delta_p < L$, so the semi-infinite

assumption is still valid and the wall transfer function (case E in Tab. 6.3) can also be used. Both of these cases use 1 harmonic.

The harmonics from both of these approaches are shown in Fig. 6.11. The amplitude of the harmonics is very similar for all cases, although there is a spatial phase difference between the two approaches, this is due to a difference in initial state.

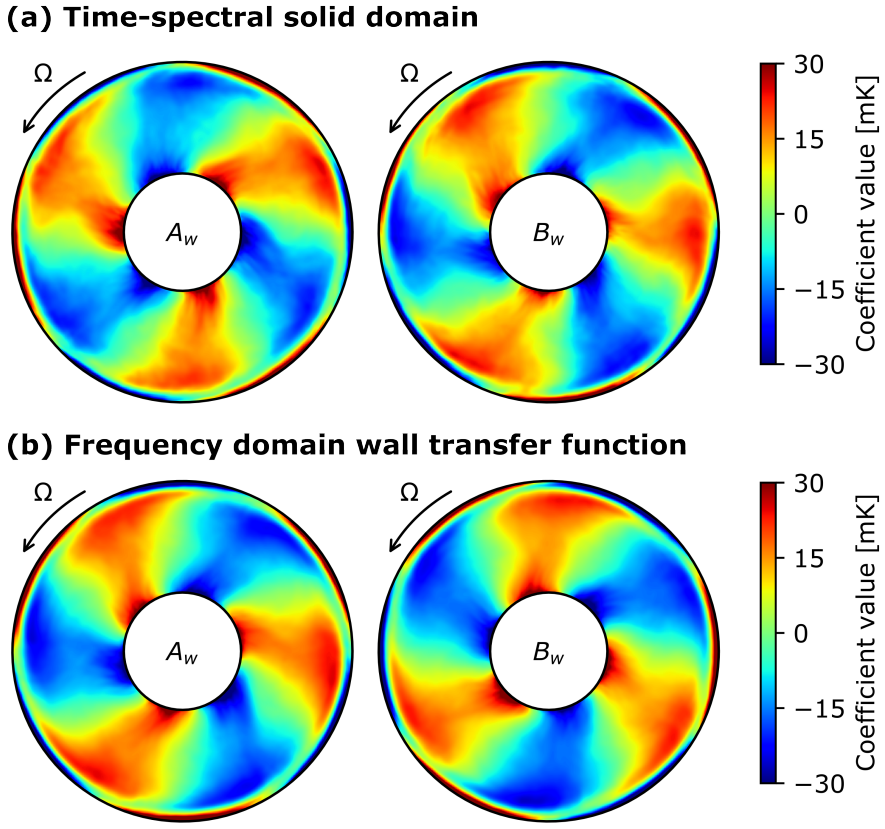

Figure 6.11. Downstream disk wall temperature harmonics A_w and B_w using time-spectral solid domain solution and the wall transfer function. (Titanium disks, LES-CHT cases D and E.)

A comparison of the circumferentially averaged RMS wall temperature fluctuations is shown in Fig. 6.12. Both the time-spectral solid domain and frequency domain wall transfer function give very similar results, further showing the validity of the 1D assumption in the context of large spatial scale low frequency temperature fluctuations.

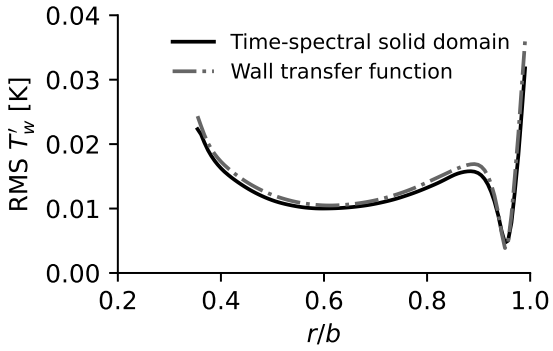

Figure 6.12. Radial distribution of RMS wall temperature fluctuations on the downstream disk using the time-spectral solid domain and frequency domain wall transfer function. (Titanium disks)

6.6.3 Calculation of Wall Temperature Fluctuations ($\delta_p < L$)

It is necessary to use wall transfer function approaches for the Epoxy disks - δ_p is less than 2 mesh cells width, so can not be resolved properly in the solid domain. Two additional directly coupled simulations were also conducted for the epoxy disks. These are not listed in Tab. 6.3 as they were not conducted using components of the multiscale framework. Both of these simulations used the interface condition in Eq. (4.5) and were initialised from an initial state reached by desynchronous time-marching with $\Delta t_s = 10,000 \Delta t_f$, as in the LES-CHT simulations conducted using the multiscale framework. The first directly coupled simulation proceeded from this initial state with both the solid and fluid marched in time with the same time step ($\Delta t_s = \Delta t_f$, similar to the approaches of Agostinelli et al. (2021); Kraus et al. (2018); Oh et al. (2021) to attempt to calculate time-accurate temperature fluctuations. In the second, the time step used in the solid domain was kept to be 10,000 times the fluid time step to see the effect of the solid domain acceleration on the solution as by Duchaine et al. (2009).

The RMS temperature wall fluctuations on the disks for all approaches are shown in Fig. 6.13. As expected, the directly coupled approach with $\Delta t_s \gg \Delta t_f$ causes a

significant overestimation of the disk temperature fluctuations by a factor of almost 10 in some locations. This is due to the time-accuracy of the solid-domain being destroyed by this approach - the solid domain "sees" a frequency that is 10,000 times lower than it actually is, with effects that are predictable with the wall transfer function and consideration of non-physical interactions with external boundary conditions. When $\Delta t_s = \Delta t_f$, there is still an overprediction of the wall temperature fluctuations due to under resolution of the thermal penetration depth, as previously discussed.

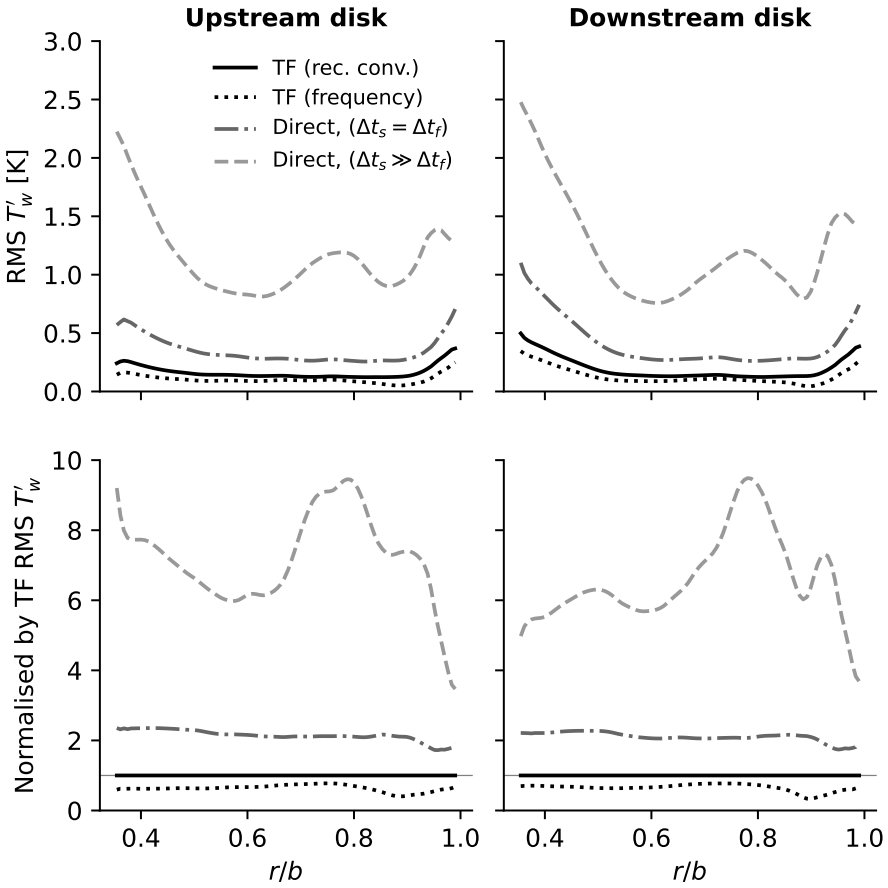

Figure 6.13. Wall temperature fluctuations from various unsteady CHT methods. (TF - wall transfer function) (Epoxy disks.)

The lower level of disk temperature fluctuations when using the frequency domain wall transfer function (with 1 harmonic) instead of the recursive convolution based version highlights the advantages of the latter approach. Instantaneous temperature

fluctuations from both methods are shown in Fig. 6.14. The large scale structure of both is similar, but the recursive convolution results in Fig. 6.14a are much less uniform and also less rotationally symmetric. The recursive convolution approach allows the user to include both sub-dominant and higher frequency temperature fluctuations (see Fig. 4.1b) with a very small computational overhead. Although it would be possible to have the same outcome by including more harmonics in the frequency domain (as in He (2019)) this would require prior knowledge to place those harmonics - this not necessary when using the recursive convolution approach.

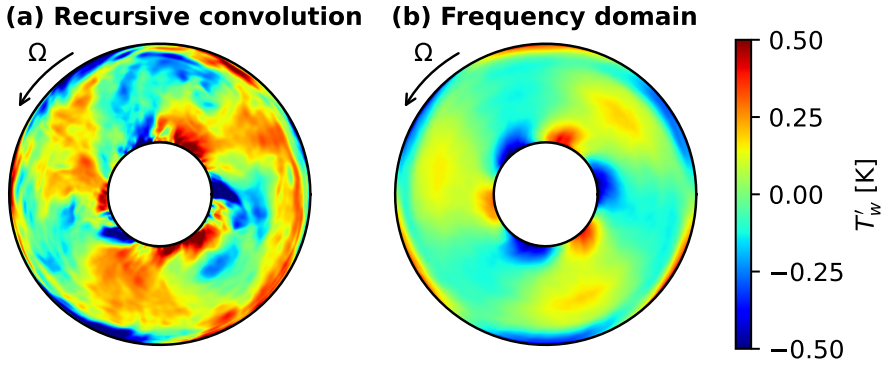

Figure 6.14. Instantaneous wall temperature fluctuations from the frequency and recursive convolution based wall transfer function approaches.

6.6.4 The Effect of Inconsistent Treatment of the Initial Transient

To illustrate the errors that can arrive from even slightly mistreating the initial transient, the average disk wall temperature distributions from five methods (the three epoxy cases in Tab. 6.3, and the two time-marching directly coupled cases discussed above) are shown in Fig. 6.15. All simulations have quite similar results, although the directly coupled solutions (particularly the case with $\Delta t_s = \Delta t_f$) gave a time-average temperature error compared to the simulations conducted using the multiscale framework. This is shown more clearly in Fig. 6.16, which plots the difference in the wall temperature calculated using the five methods tested to the wall temperature

calculated using the recursive convolution wall transfer function.

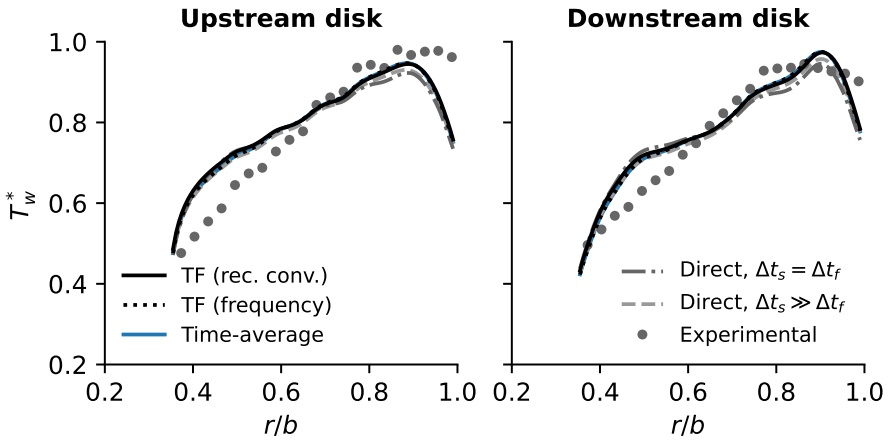

Figure 6.15. Time- and circumferential-average epoxy disk wall temperatures. Experimental data from Bohn et al. (2000). (TF - wall transfer function.)

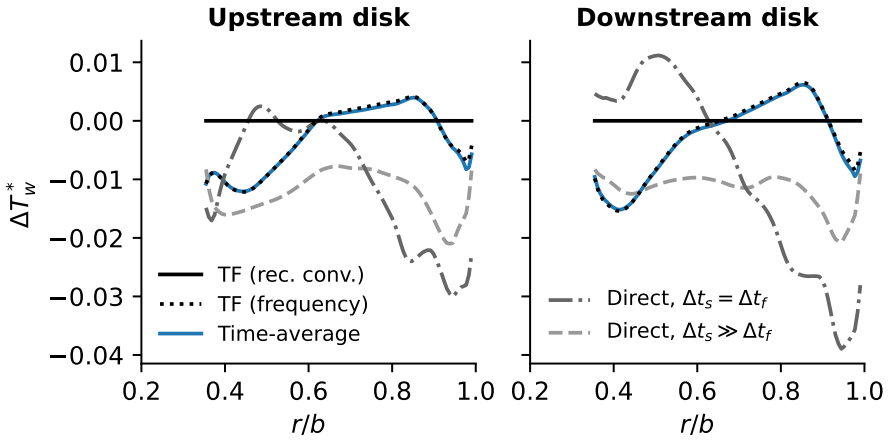

Figure 6.16. Difference in time-average disk wall temperatures to those calculated using the recursive convolution wall transfer function. (TF - wall transfer function.)

The frequency domain wall transfer function and the time-average coupled solution (both carried out within the multiscale framework) have an error that is mostly within the range $-0.01\Delta T_{max}$ to $+0.005\Delta T_{max}$ (for context, $0.01\Delta T_{max} = 0.8\,\mathrm{K}$). The accelerated directly coupled case differs from the recursive convolution wall transfer function by less than $0.02\Delta T_{max}$. The non-accelerated directly coupled case (with $\Delta t_s = \Delta t_f$, but initialised from $\Delta t_s \gg \Delta t_f$) introduces the largest uncertainty in the

time-average wall temperature, with differences between $-0.04\Delta T_{max}$ to $+0.01\Delta T_{max}$, over twice the largest deviation than the other methods.

The fact that the accelerated directly coupled case and the time-average coupled case both give smaller errors than the non-accelerated directly coupled case implies that this error is due to insufficient treatment of the initial transient. The accelerated directly coupled case equalises the fluid and solid timescales at the expense of significantly overpredicted wall temperature fluctuations (see Fig. 6.13) - the result in Fig. 6.16 shows that the effect of these over-predicted wall temperature fluctuations is smaller the effect due to the initial transient in the synchronised directly coupled case.

The natural next question is whether this difference affects the cavity aerodynamics. The peak time-average radial shear stress in Fig. 6.17 in the time synchronised directly coupled case is significantly lower than in any other case. This is quantified in Fig. 6.18; the peak radial shear from the three other cases is within $\pm$3.5% of the peak radial shear calculated using the recursive convolution wall transfer function. In comparison, the time synchronised directly coupled case deviates from this by almost 9%. A physical explanation for this difference can be found by looking at Fig. 6.16 - the presence of the initial transient in the solid domain in the time synchronised directly coupled case results in a lower radial temperate gradient, particularly on the downstream disk. This results in a lower local buoyancy force (that acts to drive the flow radially outwards) than in the other cases which all have comparable disk radial temperature gradients.

Neither the significantly overpredicted disk temperature fluctuations from the accelerated directly coupled case nor the time-average coupled case (with no disk temperature fluctuations) result in a similar sized error. It is thus clear that the issue with the time synchronised directly coupled approach is due to steady state errors in

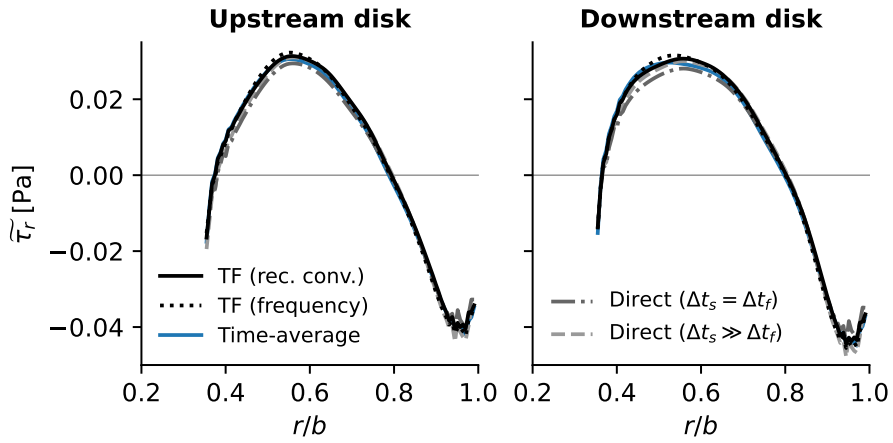

Figure 6.17. Time- and circumferential-average epoxy disk radial shear stress. (TF - wall transfer function.)

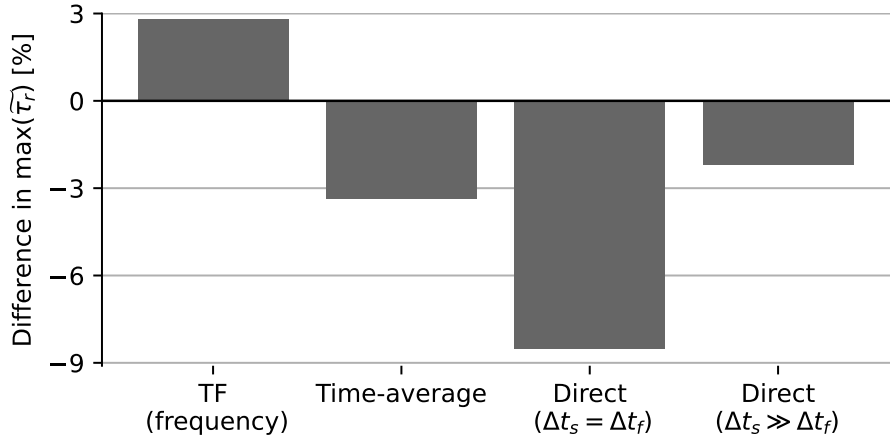

Figure 6.18. Difference in maximum time-average disk radial shear stress to the recursive convolution wall transfer function on the downstream disk. (TF - wall transfer function.)

the disk temperature distribution. This again illustrates the issues that can arise when the initial transient is not managed in a sufficiently consistent manner - even when some efforts are made to drive out the initial transient with a temporally converged initial state calculated with an accelerated directly coupled solution. The multiscale framework offers the best of both worlds here - time accurate wall temperature fluctuations can be calculated for all frequencies of unsteadiness, and the solutions are not contaminated by an initial transient that has not been fully driven out of the solid domain.

6.7 Summary of Framework Efficacy

This chapter has presented the application of the multiscale framework developed in Chapter 5 to first-of-their-kind LES-CHT simulations on rotating cavities. These simulations have been examined in light of the analysis in Chapter 4 to demonstrate the efficacy of the framework.

The time-spectral solution methodology has been shown to capture non-local interactions of low frequency temperature fluctuations with geometry and external boundary conditions in the solid domain. The consistency of time-spectral solid domain solution and the frequency domain wall transfer (it conditions where both approaches are valid to use) has also been illustrated. This shows the applicability of the novel multiscale framework to any frequency of unsteadiness that could be present in a LES-CHT simulation that aims to accurately calculate a time-accurate quasi-steady state.

The benefits of using the multiscale framework in Chapter 5 over other approaches for LES-CHT are clearly shown.

(a) Carrying out a desynchronised directly coupled solid domain solution with $\Delta t_s = 10,000 \Delta t_f$ (as by e.g. Duchaine et al. (2009)) removes the initial transient and calculates an accurate time-average state, but destroys the time-consistency of the solution, leading to an over-prediction of the RMS disk wall temperature fluctuations by almost an order of magnitude.

(b) Similarly, coupling the LES fluid domain to a time-average solid domain like Karalus et al. (2020); Scholl et al. (2016) also effectively removes the initial transient and calculates an accurate time-average state. With this approach, this happens at the cost of discarding all unsteady information about the solid domain.

(c) Carrying out a synchronised directly coupled solid domain solution with $\Delta t_s = \Delta t_f$ starting from a temporally converged initial state captures wall temperature fluctuations more accurately (although it is still limited by resolution of the thermal penetration depth), but results in a solution that is still contaminated by the initial transient to the point where buoyancy forces cause substantial differences in disk radial shear stress.

The multiscale framework is demonstrated to not suffer from any of the issues above - as far as the author is aware, it is the only methodology for LES-CHT that allows accurate solution of the wall temperature fluctuations without contamination from the solid domain initial transient. Showing that approach (c) does not in fact consistently deal with the initial transient in an LES-CHT computation (in addition to the simplified 1D case in Chapter 4) is particularly significant. This is because it has recently emerged as a popular choice in both the internal heat transfer (Oh et al., 2021) and combustion Agostinelli et al. (2021); Kraus et al. (2018) communities.

From a point of view of modelling rotating cavities; the improvement in agreement with

benchmark experimental data from including conjugate heat transfer effects (wall temperature fluctuations does not seem to be important for this) is significantly greater than moving from URANS to DES to LES. If a limited amount of compute is available, these results suggest that the largest improvement and most efficient use of resources is to include conjugate effects before the step change in cost of turbulence resolving methods.

Chapter 7

Conjugate Heat Transfer Effects on Thermally Induced Instabilities

7.1 Conjugate Problems in Rotating Cavities

Up to this point, this thesis has established the need to use both LES and CHT to simulate the flow within rotating cavities. The challenges associated with doing this have been examined, and a new multiscale framework has been developed that is the only existing methodology that can deal with these challenges consistently. Simulations have been conducted using the framework, but so far they have only been examined from a CHT methodology standpoint, as opposed to being used to yield new insights into the effect of fluid-solid thermal interactions in rotating cavities.

There is some prior evidence that this could yield interesting results. Saini and Sandberg (2021) observed a deviation from the laminar Ekman layer thickness when the cavity heating was increased at the same rotational speed. In addition, it was

shown in Chapter 3 that the average disk shear stress was different when comparing an isothermal and adiabatic disk with the same overall temperature difference, and the disk Nusselt numbers and temperatures shown in Fig. 6.5 are dependent on the disk material and heating configuration.

Most papers that investigate CHT in rotating cavities focus on the long timescale variations that are relevant to the variation of disk temperatures over a full flight or test bed cycles (Amirante et al., 2021; Sun et al., 2015). These tend to use a RANS fluid domain solution, which - although simpler to properly couple to a solid domain solution - is not able to accurately capture the fluid domain physics. The only paper prior to this thesis that has considered unsteady CHT of a rotating cavity in a quasi-steady state is Tian and Zhu (2012). These simulations used URANS, which was shown in Chapter 3 to struggle to reproduce the effects of the small scale near-wall flow structures that are relevant to heat transfer.

The question that this chapter aims to address is: *does the flow structure within the cavity depend on the exact details of the local heating?* To answer this, three of the LES-CHT cases from the previous chapter are examined:

- Axially heated disks made from a low thermal conductivity material (epoxy, case A in Tab. 6.3).
- Radially heated disks made from a medium thermal conductivity material (titanium, case D in Tab. 6.3).
- Radially heated disks made from a high thermal conductivity material (nickel, case F in Tab. 6.3).

These cases are relevant to both academic and industrial configurations. The axially

heated case is representative of some experimental rigs (e.g. Bohn et al. (2000)), whereas the radially heated cases are more representative of how a rotating cavity would be heated in an aero-engine compressor. The materials of the two radially heated cases are both used in HP compressors - titanium is usually used due its high strength to weight ratio, but nickel is often used nearer to the combustor because it holds its mechanical properties better at higher temperatures (Soares, 2008).

All three of these cases have the same bulk description in terms of non-dimensional parameters ($Re_z = 3 \times 10^3$, $Re_\phi = 3 \times 10^8$, and $\beta \Delta T_{max} = 0.27$). This means that any differences observed in the flow structures within the cavity is due to local details of how the fluid domain is heated, something that can only be predicted using CHT.

7.2 Large Scale Flow Structure

The time- and circumferentially-averaged disk temperatures and Nusselt numbers from the three cases considered in this section are shown in Fig. 6.5. Instantaneous temperatures and radial velocities on the axial mid-plane ($z = 0$) are also shown for these cases in Figs. 6.6 to 6.8.

The temperature contrast between the radial inflow and outflow is smaller for the axially heated case (Fig. 6.6a) than either of the radially heated cases (Fig. 6.7a for titanium, and Fig. 6.8a for nickel.). This is the case despite the significantly hotter disks in the epoxy case in Fig. 6.6a than in the titanium case in Fig. 6.7a. Comparing Fig. 6.6b and Fig. 6.7b or Fig. 6.8b, the radial out/inflow in the axially heated case is less intense than in either radially heated case - this is consistent with the large scale flow structure being buoyancy driven and the smaller temperature differential between the cold outflow and warm inflow.

Despite these differences the large-scale global flow structure remains qualitatively unchanged (3 circulation pairs) for both the axially heated and radially heated case. However, it is also possible that the local heating has an effect on the cavity aerodynamics and local small-scale flow structures that are important for predicting heat transfer. To investigate this, we now focus on the flow in two key areas (near the shroud and near the disk) to see if and how they are impacted by the different local heating condition or disk material.

7.3 Shroud Flow Structures

On the shroud, Fig. 7.1 shows a substantial difference in the thermal behaviour of the two cases. For the axially heated case, the shroud temperature is low due to the low thermal conductivity of the solid domain, and the Nusselt number drops significantly towards the mid-axial location $z/s = 0$. For the cases heated by radial conduction (nickel and titanium), the shroud temperature is uniform and close to T_{max}, and the Nusselt number does not have the large variation present in the axially heated case. This conclusion is the same irrespective of the radially heated disk material, although the lower Nusselt number for the nickel case is unexpected given the higher shroud temperature in that case. This will be explained later in this section.

Figure 7.2 shows the instantaneous Nusselt numbers on the shroud and the downstream disk corresponding to the cases in Fig. 7.1. Looking at the shroud, streaks of enhanced heat transfer are visible in the radially heated case (Fig. 7.2b and c), but not in the axially heated case (Fig. 7.2a). Referring back to the average shroud Nusselt numbers in Fig. 7.1, it can be seen that the occurrence of these streaks leads to an overall enhanced shroud Nusselt number.

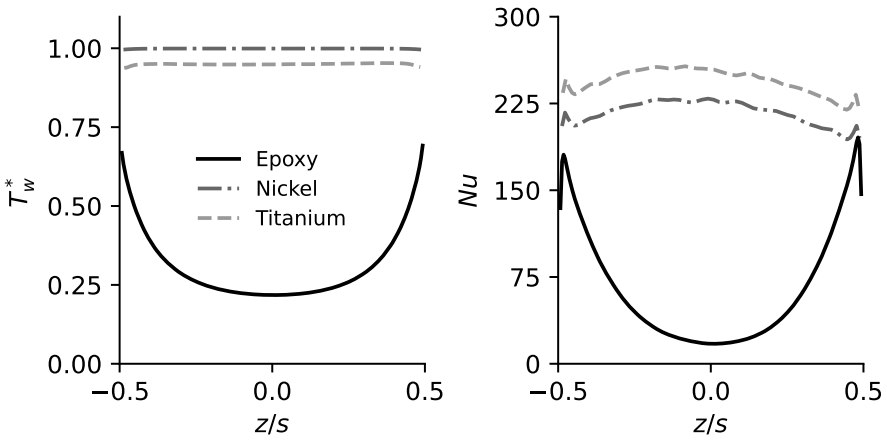

Figure 7.1. Average shroud temperature (left) and Nusselt number (right).

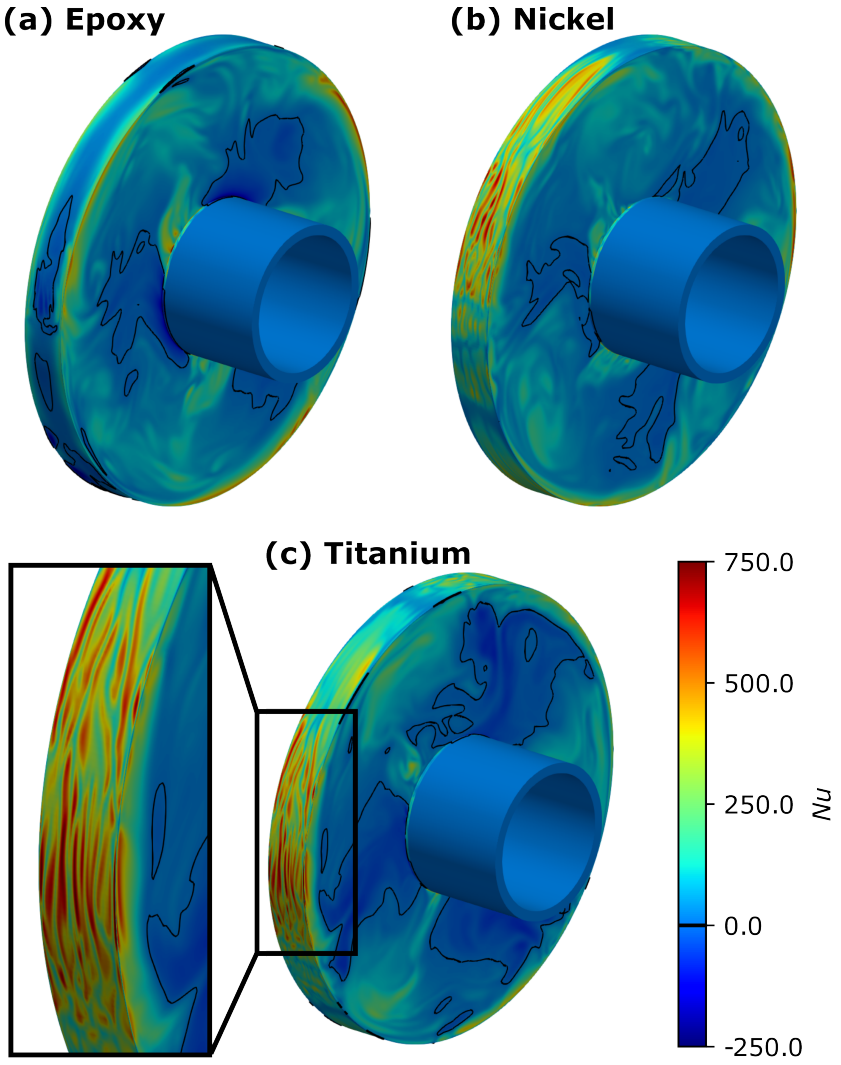

Figure 7.2. Instantaneous Nusselt numbers on the shroud and downstream disk.

The reason for the inception of the streaks is shown in the time- and circumferential-average temperature contours in the fluid domain in Fig. 7.3. Even though both the epoxy and titanium cavities appear to have similar axially averaged radial temperature distributions, the mixing of hot fluid from near the heated surfaces is quite different between the two cases.

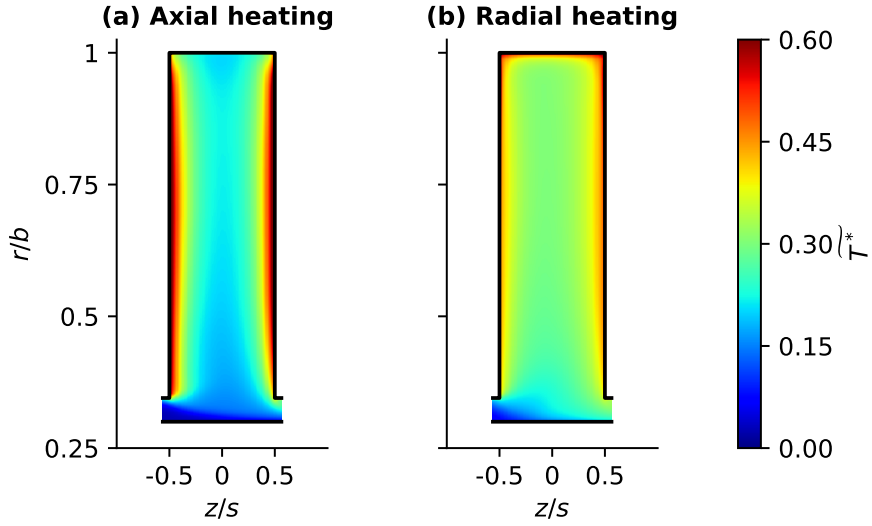

Figure 7.3. Average static temperature in the meridional plane for the epoxy and titanium cases.

Taking Fig. 7.3a together with the shroud temperature distributions in Fig. 7.1, it can be seen that the near shroud region for the axially heated case has a negligible radial temperature gradient, meaning that there is no buoyancy force driving the formation of the streaks as was observed in Chapter 3 and by Puttock-Brown and Rose (2018); Puttock-Brown et al. (2017). The shroud temperature is so low in this case due to the low thermal conductivity of the solid domain material - any shroud heat flux has to come via axial conduction from the outer radii of the disks, so even a small shroud heat flux causes a large temperature drop relative to the temperature at the top of the disks (Fig. 6.5).

In contrast, the radially heated disks have an unstable near-shroud radial density

gradient that causes the formation of the streaks (particularly in the cyclonic circulations) that enhance heat transfer by mixing the colder fluid in the bulk flow with the hotter fluid near the shroud in a manner consistent with Rayleigh-Bernard convection, as in Puttock-Brown and Rose (2018); Puttock-Brown et al. (2017).

The lower shroud Nusselt number in the nickel cavity (Fig. 7.1) can also be explained by examining the average temperature contours. Figure 7.4 shows the average temperature distributions for the nickel and titanium radially heated cavities. Due to the stronger disk heating in the nickel cavity, the bulk fluid is warmer. The warmer bulk fluid causes a smaller near-shroud radial density gradient, resulting in less frequent and less intense streaks as seen in Fig. 7.2.

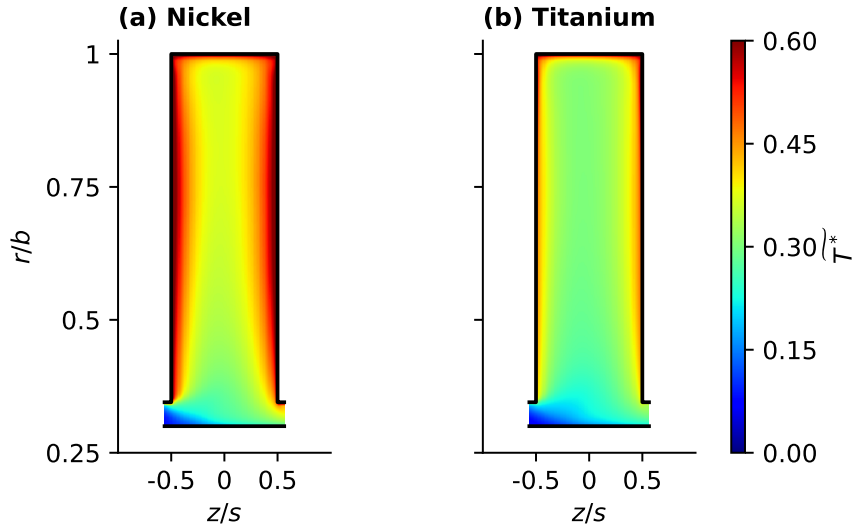

Figure 7.4. Average static temperature in the meridional plane.

The effect of the difference in shroud flow structure is not restricted to the near-shroud region of the flow. Heat transfer from the disks is much less efficient than heat transfer from the shroud at mixing fluid from the local heated surface with the bulk flow. This can be observed in Fig. 7.3a, where the high temperatures in the axially heated case are very much restricted to the near-disk region, leading to colder mid-cavity flow. In

contrast, the radially heated cases in Fig. 7.4 exhibits a significantly warmer bulk flow due to the more efficient mixing of the hot fluid from the heated shroud by the streaks. The effect of the shroud heat transfer on the bulk flow can also be observed in the instantaneous temperature contours in Figs. 6.6 to 6.8a. The less intense radial arms in the axially heated case (see Fig. 6.6b compared to the radially heated cases in Figs. 6.7 and 6.8b) can be attributed to the reduced buoyancy force caused by a smaller temperature differential between the cold axial throughflow and the warmer cavity fluid.

The relevance of these near-shroud flow structures to our research question is that their formation is dependent on the strength of the local heating at the shroud - a significant heat-flux is needed to create a sufficient radial density gradient to drive the formation of these streaks.

7.4 Disk Flow Structures

The difference in the disk Nusselt numbers between the three cases in Fig. 6.5 implies that it is also worth examining the near-disk flow field for differences in the local flow-structures.

The flow close to the disks is widely accepted as behaving as a laminar Ekman layer; this has been demonstrated earlier in this thesis and at conditions closer to engine relevance by Gao and Chew (2022). However, the near-disk flow that is outside of the Ekman layer (i.e. further than $\delta_{\mathrm{Ek}}/s = 0.0176$ from the disk) is rarely investigated, even though it is responsible for supplying forcing to the Ekman layer dynamics and effectively providing the "thermal boundary conditions" at the outer edge of the Ekman layer.

Figure 7.5 shows the axial turbulent heat flux, $\widetilde{V_z'T'}$: this is the effective heat flux caused by the axial velocity fluctuations when time averaging the flow. Near the upstream disk ($z/s = -0.5$), a positive value of $\widetilde{V_z'T'}$ is caused by axial velocity fluctuations away from the disk being associated with an increase in temperature and an axial velocity fluctuation towards the disk being associated with a decrease in temperature - this is consistent with unsteady flow structures enhancing transport from a hot disk to a cooler bulk flow. On the downstream disk ($z/s = 0.5$) negative values of $\widetilde{V_z'T'}$ are consistent with this same unsteady mixing of fluid between the disk and bulk flow. The extreme values in the region above $r/b \approx 0.95$ in Fig. 7.5 are caused by the interaction of the near-disk flow with the shroud, we restrict our discussion to the flow that is only affected by the disk and the bulk flow, i.e. $r/b < 0.95$.

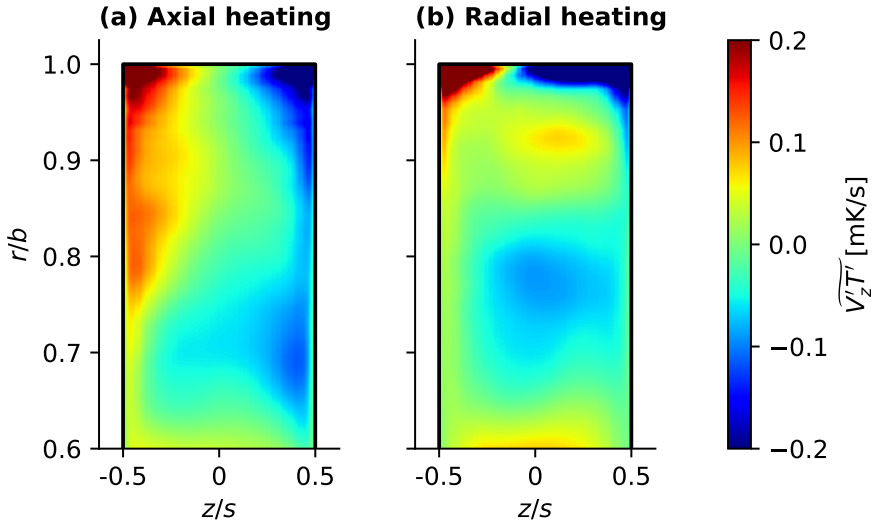

Figure 7.5. Axial turbulent heat flux distribution in the meridional plane for the epoxy and titanium cases.

For the axially heated case (Fig. 7.5a), there is a turbulent heat flux near both disks that is not present in the titanium radially heated case (Fig. 7.5b). While the difference in $\widetilde{V_z'T'}$ is likely due to an increase in local flow structures mixing near-disk and bulk flow, it is possible that it is due to the higher temperature contrast between the disks

and the bulk flow in the axially heated case increasing $\widetilde{V_z' T'}$ through an increase in the amplitude of T'.

To rule this out, the root-mean-square (RMS) velocity fluctuations were compared for the two cases by calculating a normalised difference as

$$\Delta V'_{z,\,\mathrm{RMS}} = \frac{\mathrm{RMS}\left(V'_{z,}\right)_{\mathrm{AH}} - \mathrm{RMS}\left(V'_z\right)_{\mathrm{RH}}}{\mathrm{RMS}\left(V'_z\right)_{\mathrm{RH}}}, \tag{7.1}$$

where AH and RH stand for the axially and radially heated cases respectively. The result of this comparison is shown in Fig. 7.6: the axial velocity fluctuations are significantly larger ($\sim$ 25%) near the disks in the axially heated case, indicating the formation of turbulence or instabilities in this region caused by the disk heat transfer. Due to asymmetries in the axially averaged flow (see Hickling and He (2021) and Fig. 7.5) this region is larger next to the downstream disk (Fig. 7.6).

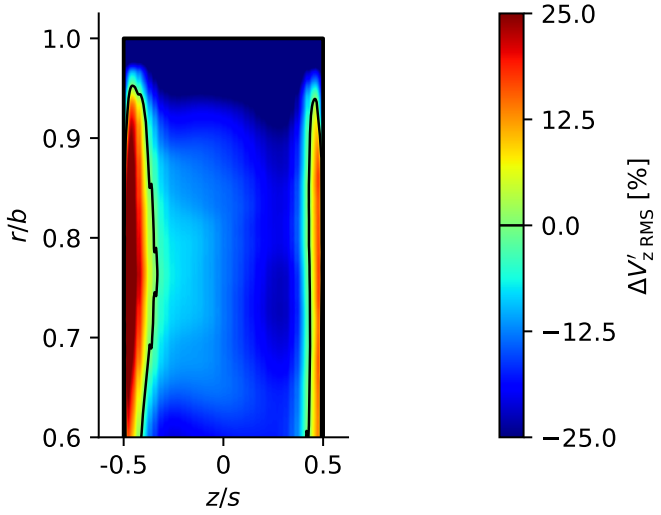

Figure 7.6. Difference in disk-normal velocity fluctuation levels between the axially heated cavity and the radially heated cavity.

To visualise the flow structures causing the extra disk-normal mass and energy transport, Fig. 7.7 plots the radial vorticity $2\delta_{\mathrm{Ek}}$ from the upstream disk for both cases

at the same time instant as Figs. 6.6 and 6.7. This axial location is outside of the Ekman layer thickness, but still near-enough the disk so that flow structures that form here could affect the dynamics of the Ekman layer.

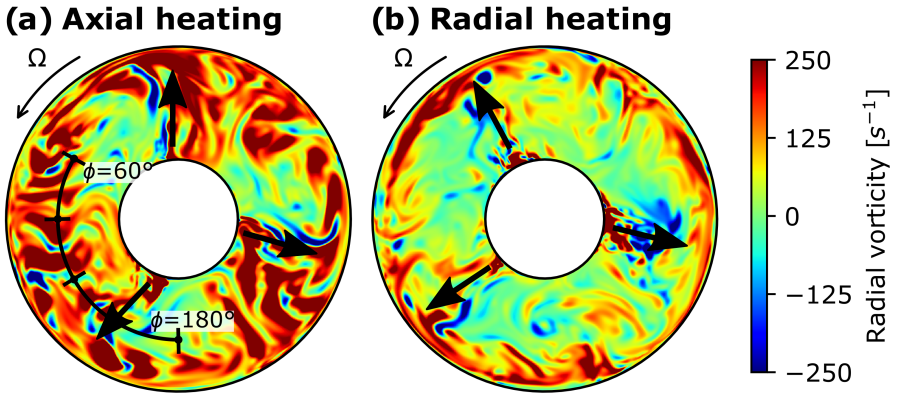

Figure 7.7. Radial vorticity on the plane $2\delta_{Ek}$ from the upstream disk ($z/s = -0.465$). Arrows indicate regions of radial outflow.

By comparing the values of the radial vorticity in Fig. 7.7a with those in Fig. 7.7b, the existence of radially aligned vortices forming in the anti-cyclonic circulation is clear in former, but not in the latter. Due to its higher thermal conductivity, the nickel case has hotter disks, with temperatures that are inline with the radially heated epoxy case (see Fig. 6.5). The same behaviour as in Fig. 7.7 is observed when comparing the nickel and titanium cases: Fig. 7.8 shows radially aligned vortices form in the nickel case with strong disk heating, but not in the titanium case with weak disk heating.

These results in Figs. 7.7 and 7.8 are indicative of the formation of some local large-scale turbulent or other coherent flow structures. The enhanced mixing of the near-disk and bulk flow through these flow structures may contribute to the higher Nusselt number observed in the axially heated case and the radially heated nickel case in Fig. 6.5. The contrast between Fig. 7.7a and Fig. 7.7b is quite stark, and to the best of our knowledge this heating induced destabilisation and formation of vortices in the near-disk flow is not something that has been observed before. The mechanism

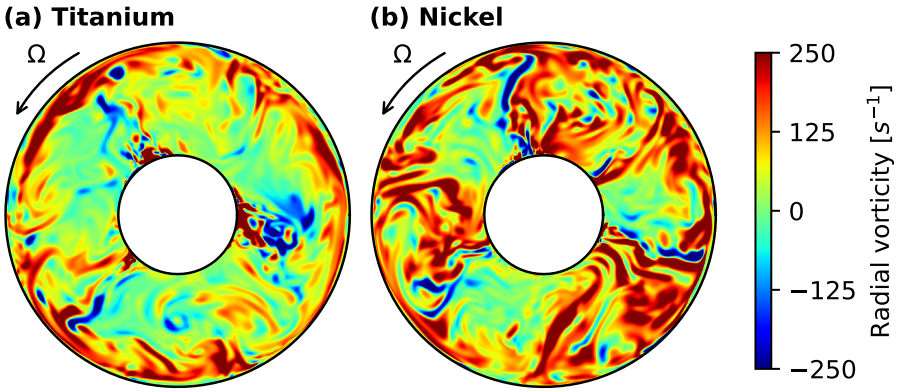

Figure 7.8. Radial vorticity from both radially heated cases on the plane $2\delta_{Ek}$ from the upstream disk ($z/s = -0.465$).

for this warrants further investigation and is examined in detail below.

7.5 Heating Induced Near-Disk Instability

7.5.1 Behaviour of the Near-Disk Vortices

The positive sign of the vorticity in the structures in Fig. 7.7a is consistent with the vortices rolling up in the near-disk shear layer caused by the tangential slip of the large-scale flow structure. It makes sense that these vortices only form in the case with strong disk heating because, in air, the increased temperature in the near-disk fluid acts to destabilise the near-disk flow through the combined effects of the temperature dependent density and dynamic viscosity (Özgen, 2004; Schäfer et al., 1995). However, this does not explain why the vortices seem to occur predominately in the cyclonic circulations.

The flow field for one circulation pair is shown on a radial isosurface of $r/b = 0.7$ in Fig. 7.9. The radial location for this plot is shown in Fig. 7.7a by a black line, with markers at 30° increments. The tangential coordinate ϕ is set to be zero at top dead-centre, and increases in the anti-clockwise direction. The distribution of radial vorticity in Fig. 7.9e shows that the vortical flow structures are confined to the near-disk region, and appear to form in the region of radial outflow ($\phi \approx 145°$ in Fig. 7.9b). Near the upstream disk, the vortices are rotating in the positive sense (consistent with Fig. 7.7b), and they rotate in the opposite direction near the downstream disk. Due to the globally negative (i.e. in the anti-cyclonic direction) circumferential velocity visible in Fig. 7.9c, the vortices are observed to be present throughout the anti-cyclonic circulation. The vortices are not present in the cyclonic circulation as can be seen for $\phi > 150°$ in Fig. 7.9e - this implies that they are destroyed in the radial inflow just as they are generated in the radial outflow.

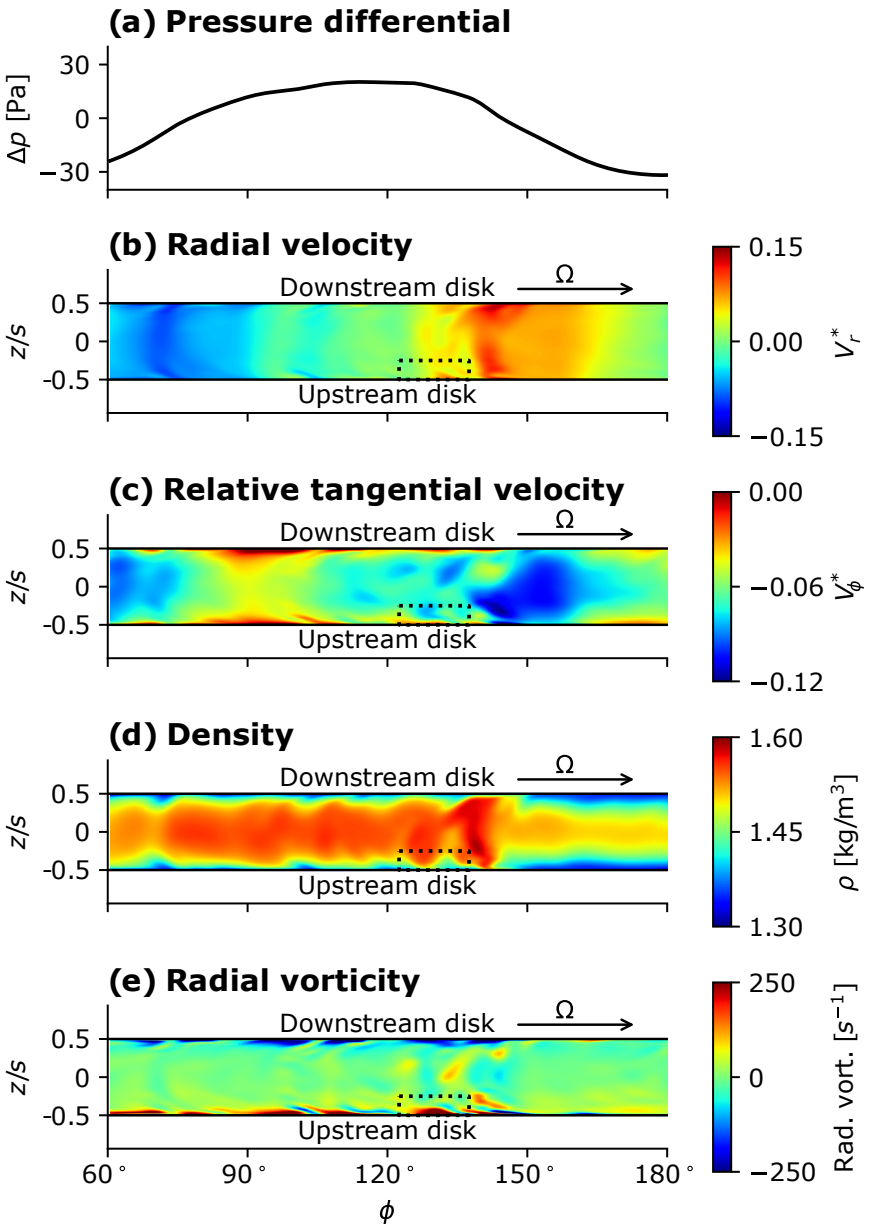

Figure 7.9. Flow field in the ϕz-plane at $r/b = 0.7$ for the axially heated case. Circumferential location indicated in Fig. 7.7a.

Figure 7.10 shows a zoomed in view of the region indicated with a dotted line in Fig. 7.9, with the distance from the wall (Δz) normalised by the theoretical laminar Ekman layer thickness, δ_{Ek}. The instability that causes these vortices originates at the wall within the Ekman layer. This can be seen in the circulation visible around $\phi \approx 130^\circ$ in Fig. 7.10a, which extends up to about 2 Ekman layer thicknesses from the wall. From the temperature contours in Fig. 7.10a it would appear that this flow structure is not responsible for much wall-normal energy transport, however this is not the case. The flow structure is better visualised by subtracting the "large-scale" velocity (calculated by circumferentially averaging the velocities over the plot area) from local relative velocities to calculate a velocity perturbation as shown in Fig. 7.10b. Here, we can clearly see a vortex that extends up to 10 Ekman layer thicknesses from the disk, ejecting hot fluid in to the bulk flow and injecting cold fluid into the near-disk region.

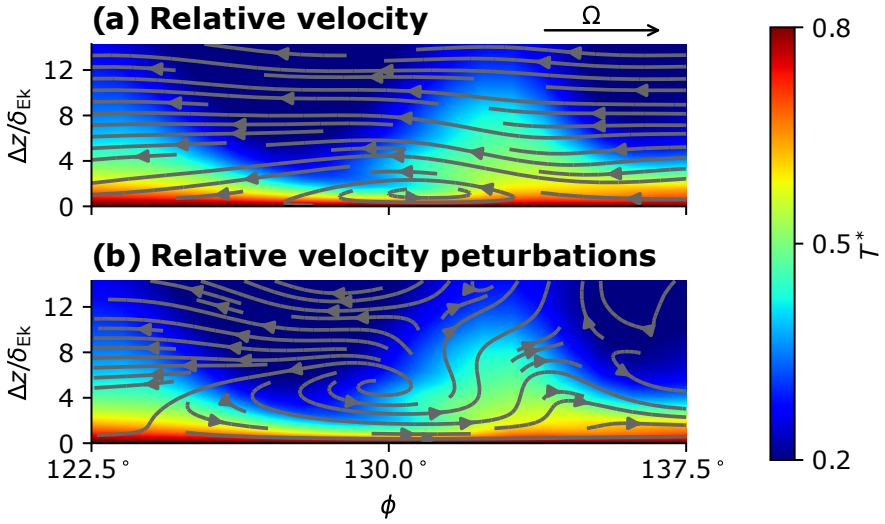

Figure 7.10. Near disk instantaneous streamtraces and temperature showing a heating induced vortex. The region corresponding to this figure is outlined with dots in Fig. 7.9.

7.5.2 Heating Induced Destabilisation Mechanism

Figure 7.11a summarises the observations made in Fig. 7.9 and Fig. 7.10. Vortices are generated in the regions of radial outflow, destabilising the near-disk flow downstream in the cyclonic circulation, before being destroyed in regions of radial inflow.

The mechanism for the generation of vortices in the radial outflow is explained in the diagram of a single vortex near the upstream disk (Fig. 7.11b): in the radial arm, there is an adverse pressure gradient (see Fig. 7.9a), leading to a pressure force acting in the cyclonic direction on a fluid parcel. In the bulk flow, this is balanced by the Coriolis force from the radial outflow acting in the anti-cyclonic direction due to the positive radial velocity. Near the disk, the local heating causes a reduction in density (as seen in Fig. 7.9d), and hence a reduction in the local Coriolis force (which is proportional to density). The reduced Coriolis force means that there is a net force acting in the cyclonic direction on the near-wall fluid, against the direction of the bulk flow. The net force acting against the direction of bulk flow drives the roll-up of a vortex with positive vorticity on the upstream disk, and a vortex with negative vorticity on the downstream disk - this is consistent with the flow field shown in Fig. 7.9e.

The same logic can be used to explain the destruction of vortices in the radial inflow. As shown in Fig. 7.11c, the pressure force acts in the anti-cyclonic direction, stabilising the flow, and the Coriolis force acts in the cyclonic direction. Again, in the bulk flow, these forces are balanced, but in the near-disk region the Coriolis force is reduced due to the lower density; giving a net force in the anti-cyclonic direction. This net force is in the same direction as the bulk flow and opposes the sense of rotation of the vortices that are entering the region of radial inflow from the anti-cyclonic circulation.

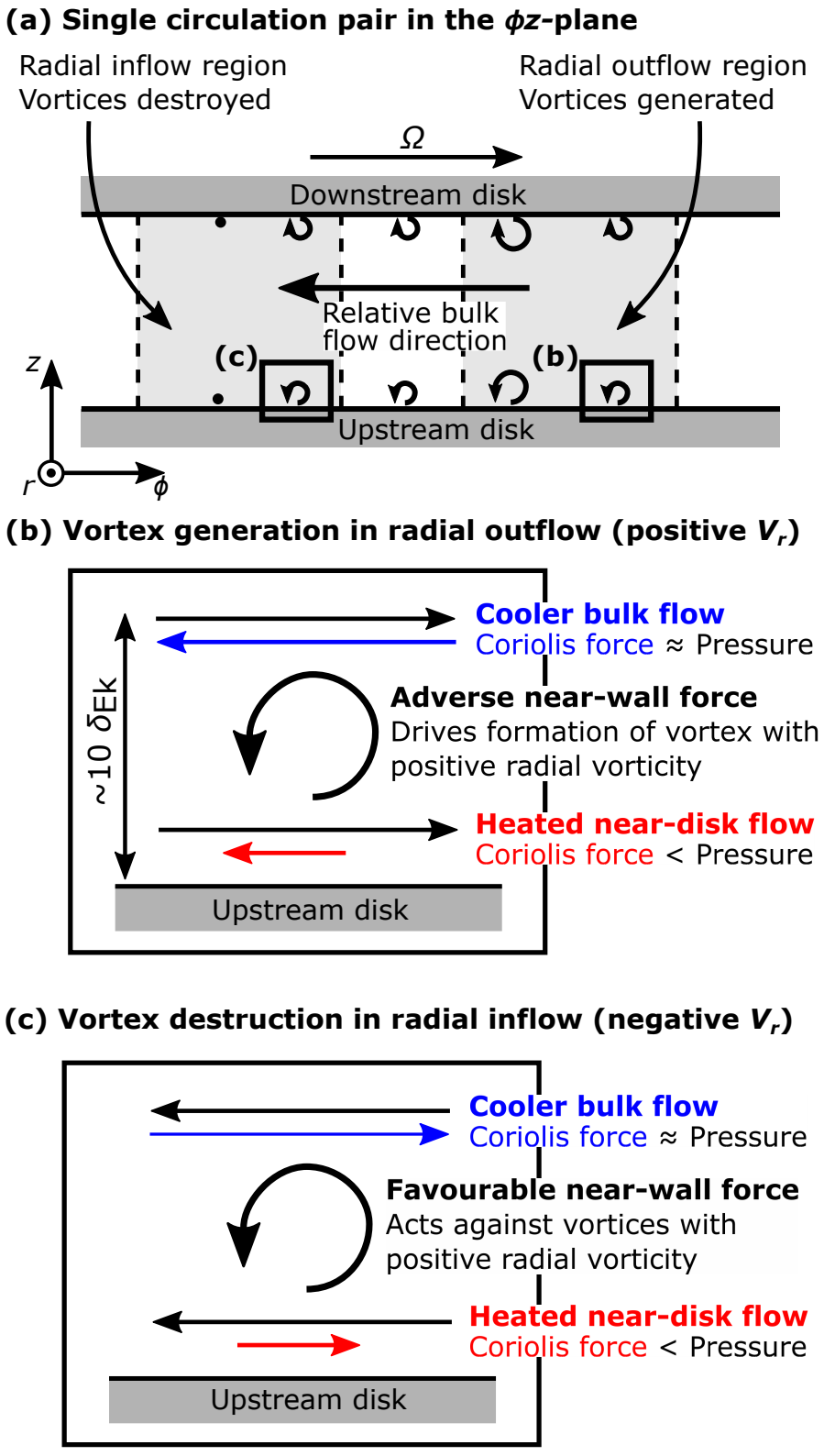

Figure 7.11. ϕz-plane view of the mechanism for the formation of heating induced vortical instabilities in the anti-cyclonic circulation.

7.6 Implications for Further Investigations

The formation of small-scale flow structures in key regions within the cavity is found to be strongly dependent on exactly how the cavity is heated and the thermal properties of the disks, even for the same bulk flow description. The stronger shroud heating in radially heated cases causes buoyancy driven streaks to form. In both cases with strong disk heating (the axially heated case and the high conductivity radially heated case), vortical structures responsible for mixing hot near-disk and cold bulk flow were observed to form in radial outflow. This is the first time that the latter flow structure has been observed. It is worth highlighting that the mechanism for this is a time-average heat transfer effect - so an unsteady solution of the solid domain should not be required to capture it. This is backed up by the observations in Fig. 6.17 - as long as the time-average disk temperate is well predicted, there is little difference caused by either neglecting wall temperature fluctuations or artificially exaggerating them (through the solid domain acceleration).

The heating induced destabilisation of the near-disk flow has implications for studies that consider the bulk conditions where an Ekman layer may transition to turbulence, such as Gao and Chew (2021). The result suggests two things: first, that the effect of wall heating may need to be taken in to account for Ekman layer transition considerations; and second, that these studies may need to be at a finer-grained than just considering bulk parameters to describe the flow - whether the Ekman layer will transition could be dependent on the local thermal boundary conditions.

The location of the vortices also shows that there are scenarios where the laminar Ekman layer modelling argument is an oversimplification when considering rotating cavity flows from a heat transfer perspective. A laminar Ekman layer would suggest

that there are no self-generated flow structures causing wall-normal transport. Although this may be the case within the Ekman layer thickness, flow structures have been observed outside of this that footprint on the flow within Ekman layer and disrupt its dynamics. Due to the slow slip of the large-scale flow structure, this means that there is no region of the near-disk flow that can be considered to persistently behave in a manner consistent with a laminar Ekman layer.

In Fig. 7.10, the Ekman layer thickness corresponds to a local normalised wall distance of $z^+ = 11$. In conventional turbulent boundary layers it is widely accepted that flow structures that significantly affect heat transfer can occur further out and on larger scales than this. We have shown that this is the case for rotating cavities too - the heating induced vortical structures extend past $z^+ = 100$ - and that proper consideration of the near-disk flow that occurs outside of the laminar Ekman layers is important - this is relevant to wall and SGS modelling strategies that will need to take care not to disrupt the formation of these instabilities by excessive damping from the eddy/SGS viscosity.

Chapter 8

Conclusion

8.1 Summary

The research in this thesis contributes towards a better understanding of both rotating cavity flows and unsteady conjugate heat transfer.

A lack of clarity in the pre-existing literature on what turbulence modelling fidelity is necessary to simulate rotating cavity flows is addressed in a systematic baseline modelling study. It is found that fully wall resolved LES is needed to accurately capture the multiple physical mechanisms that occur in different parts of the cavity. URANS approaches are found to be unsuitable for predicting the heat transfer. The elevated eddy viscosity prevents the formation of near-shroud heat transfer enhancing streaks, and does not enhance the modelled turbulent heat flux sufficiently to account for their effects. In addition, DES (or wall modelled LES) behaves inconsistently with its expected behaviour in all simulations. At low Reynolds and Grashof numbers (2×10^5 and 3.03×10^9 respectively), DES captures the formation of streaks, despite being in

URANS mode in the near-shroud region.

At a higher Reynolds and Grashof number (2×10^6 and 3.03×10^{11} , approaching engine-relevant conditions), DES suppresses the near-shroud streaks, leading to an underprediction of heat transfer in this region, while on the disks it double accounted for wall-normal velocity fluctuations, causing erroneously enhanced heat transfer. Quite remarkably, DES exhibits a concerning behaviour where modelled turbulence generated at the shroud is transported into the bulk flow, contaminating the entire solution with non-physical eddy viscosity. The radial inflow that causes this is a fundamental feature of rotating cavity flows and is relevant to many other internal flows, indicating that DES should only be used with caution going forwards. The presence of double accounting in the near-wall region also shows that there should be some care taken when using zonal hybrid approaches and wall-modelling, even though these approaches explicitly enforce zero effect from the wall model in the bulk flow.

y^+ and related wall mesh resolution metrics (generally derived from simulations of channel flows or similar) are found to be a poor predictor of sufficient resolution in rotating cavity simulations. In the low Grashof number case, the mesh was observed to be too coarse to properly capture the near-shroud streaks, despite having a mesh that was very well resolved by normalised wall spacing requirements. In the high Grashof number case, LES with a high aspect ratio near-wall mesh was observed to give better, more consistent, results than DES (which was may be expected to have been more suited to that grid).

The baseline modelling study also showed that using adiabatic instead of isothermal disks alters the local aerodynamics through buoyancy effects, ultimately changing the radial location of near-disk flow reversal. This feedback of the wall heat transfer to the aerodynamics suggested that it would be worth investing in CHT simulations to better

capture these interactions.

Meeting the requirement to use LES with CHT is challenging due to the significantly different timescales present in the fluid and solid domains. The longer solid domain timescale leads to an initial transient that is four orders of magnitude longer than would occur in a standalone fluid domain simulation. Many existing methods for time domain based unsteady CHT (e.g. Agostinelli et al. (2021); Kraus et al. (2018); Oh et al. (2021)) attempt to account for this by carry out an accelerated time domain solution in the solid domain until temporal convergence is reached. Then, they switch to a non-accelerated simulation that is assumed to be free from the effect of the initial transient. In a simplified 1D analysis based on a near-wall temperature signal from an LES solution, this is shown to be incorrect - even initialising the unsteady solid domain from a correct time-average state causes a long-lived error in the mean temperature within the solid domain if solved in teh time domain.

The only existing method where this is not the case is the closely coupled CHT method of He (2019). This method calculates the near-wall temperature fluctuations using a frequency domain wall transfer function approach based on an analytical solution of unsteady conduction in a 1D semi-infinite solid domain. Although this method is free from inconsistencies around the initial transient, this thesis highlights three key issues:

- Apart from some brief discussion in (He, 2019), there has not been any consideration of the validity of the 1D assumption.
- It is not able to capture low frequency temperature fluctuations that arise from large scale coherent structures such as radial arms in rotating cavities. The thermal penetration depth from these fluctuations can be larger than the solid domain thickness, violating the semi-infinite assumption and allowing non-local

interactions with geometry and external boundary conditions to occur.

- The frequency domain representation of the wall transfer function requires a large number of harmonics (50-100) to be stored at each coupled cell face. Choosing the frequency of these harmonics is difficult without prior knowledge of the flow, reducing the potential of the method for wider uptake.

The 1D assumption is demonstrated to be valid in the context on LES-CHT - an unsteady fluid temperature field extracted from an LES simulation is coupled to a 3D solid domain, and the resulting temperature fluctuations shown to be near identical to temperature fluctuations calculated using the wall transfer function.

A new multiscale framework for LES-CHT is developed to address the remaining two issues. To avoid the initial transient, a moving average in the fluid domain is coupled to a time-average solid domain using the closely coupled interface condition of (He, 2019). Low frequency temperature fluctuations are solved in the solid domain using a time-spectral representation of unsteady conduction that is coupled to a recursive DFT in the fluid domain using a closely coupled harmonic balance interface condition. High frequency temperature fluctuations are treated locally using a reformulated wall transfer function approach. To reduce the prior knowledge required of the user, the wall transfer function is reformulated using the ADE method of Dragna et al. (2015) to use recursive convolution. This approach does not require choosing frequencies for harmonics, and allows the entire range of timescales that may be relevant to the simulation to be covered economically. To the best of the author's knowledge, this framework is the only one existing that allows a consistent treatment of the solid domain initial transient and the effect of all frequencies of thermal unsteadiness on the wall temperature to be calculated accurately.

The novel framework is applied in first-of-their-kind LES-CHT simulations. These simulations are first examined to demonstrate the efficacy of the framework - in particular the interaction of the time-spectral solid domain temperature fluctuations with external boundary conditions is shown, and the ability of the recursive convolution based wall transfer function approach to capture broadband high frequency unsteadiness is illustrated. Solutions using the multiscale framework are also compared to solutions calculated with existing methods state-of-the-art methods for LES-CHT. It is shown that these methods either calculate a time-average initial state but do not allow the calculation of disk wall temperature fluctuations (Duchaine et al., 2009; Karalus et al., 2020; Scholl et al., 2016), or do not consistently deal with the fluid-solid timescale disparity (Agostinelli et al., 2021; Kraus et al., 2018; Oh et al., 2021), leading to a 9% difference in disk radial shear stress compared to the multiscale framework - over three times the difference of any other LES-CHT method tested. A useful implication of this for engineering studies of rotating cavities is that these results can provide a reasonable amount of confidence in using time-average CHT approaches (that neglect wall temperature fluctuations) for LES-CHT of rotating cavities.

The flow fields from the LES-CHT simulations are also used to investigate the dependence of the flow structures within the rotating cavity on the exact details of the local heating. Three cases are considered: axially heated disks made from a low thermal conductivity material; radially heated disks made from a medium thermal conductivity material; and radially heated disks made from a high thermal conductivity material. The axially heated and radially heated high thermal conductivity simulations are both found to predict significantly higher disk temperatures and Nusselt numbers than the low thermal conductivity radially heated simulation. This is observed to cause the formation of heat transfer enhancing radially aligned near-disk vortices in

anti-cyclonic circulations, a previously unobserved flow structure. The mechanism for the formation of these vortices is explained - the disk heating the lowers to near-disk density interrupting the near-wall balance of the pressure and Coriolis forces, causing a roll-up of vortices in regions of radial outflow, and destruction of vortices in regions of radial inflow. This mechanism is a result of the time-average heating of the disks, so the use of the multi-scale wall temperature fluctuation treatments developed in this thesis is not expected to be necessary to capture them. That said, the discovery of these flow structures indicates the potential of the methodology to provide further insights into flows relevant to gas turbines and the wider heat transfer community.

8.2 Further Work

First, for turbulence resolving simulations at engine-relevant conditions to be practical methods that reduce the near-wall mesh requirements of LES will be needed. This thesis has shown that using hybrid URANS/LES approaches (including zonal methods) can lead to errors due to the double accounting of the near-wall turbulent fluctuations. In general, the results in this thesis consistently show very little turbulence generation within the Ekman layers - it seems likely that the majority of the unsteadiness within this region is due to "foot-printing" of eddies in the bulk flow. This raises the interesting possibility that LES on hybrid URANS/LES grids may give as reliable results for the disk heat transfer as more complex hybrid methods in rotating cavities.

An alternative to hybrid methods is wall-modelled LES. However, the wall models are nearly universally based on the log-law - whether this is in any way an accurate representation of the near-wall physics of a laminar Ekman layer subject to external

disturbances from the large-scale flow structure and bulk turbulence needs to be critically assessed. It would be interesting to see if a useful wall-model could be developed based directly on the known physics of laminar Ekman layers.

It is clear that there are many avenues to explore for reducing the near-wall cost of turbulence resolving rotating cavity simulations, and that going forwards it will be necessary to develop a better knowledge of the error-cost trade-offs from using these approaches and establish engineering best practises for them.

To be most useful for rotating cavities, the existing CHT methodology needs to be integrated in a long-timescale transient CHT solver. This is because, as discussed in Section 1.1.1, the transient growth of the cavity during a flight cycle (particularly in response to events such as a full hot re-slam) is the governing factor in setting the engine cold-build clearances (Atkins, 2013). Fortunately, this is not expected to be challenging, as long-timescale multiscale LES-CHT modelling has been well-developed by Fadl and He (2017); He and Fadl (2017) for predicting temperature distributions during warm-up and cool-down for land-based gas turbines in flexible operations.

There also are many other areas where the newly developed multiscale framework for LES-CHT may enable impactful insights.

Within rotating cavities, a prime candidate for this would be rim seal flows and the rotor-stator cavity in gas turbine wheel spaces. There is a broad consensus that it is necessary to use LES to capture some of the fluid domain physics of these flows (see e.g. O'Mahoney and Chew (2012)), which can form inertial waves and large scale flow structures that are in some respects similar to the flow within rotating cavities (Cao et al., 2004; Gao et al., 2020). Despite the function of the cavity purge flow to keep

rotor and stator disk temperatures to acceptable levels by reducing ingestion of hot gases, many experimental and computational studies only consider isothermal conditions with main gas path and cooling flow at the same temperature, and ingestion measured using a tracer gas. (e.g. Sangan et al. (2012)) As far as the author is aware, the LES simulations that have been conducted (Hösgen et al., 2020; O'Mahoney and Chew, 2012; Pogorelov et al., 2019) have not included high fidelity thermal boundary conditions. As seen in Chapter 7, the interaction of the near-wall flow and disk heat transfer may affect the near-wall aerodynamics, potentially altering the thermal buffering effect (Cho et al., 2016) between the near-rotor cool purge flow and cavity bulk flow, and also the near-stator hot ingested gas and bulk flow. Even so, accurately capturing rim-seal ingestion is extremely challenging, and it is not currently clear what the necessary physics to capture is. It seems unlikely that application of LES-CHT to rim seals will solve this, but knowledge of the fluctuating wall temperatures inside the rim-seal cavity may be of use to designers for fatigue or setting upper limits on allowable ingestion levels.

It would also be interesting to investigate rotating cavities with radial inflow - here hot fluid enters the cavity at the shroud and attaches to the disks (Onori et al., 2016, 2019; Sun et al., 2015). This heats the cavity disks more quickly, reducing the time lag between the compressor drum and casing, thus allowing for smaller cold tip clearances (Atkins, 2013). This thesis has shown that the disk heating can affect the thermal mixing between Ekman layers and the bulk flow; whether this is enhanced or not in cavities with radial inflow may have an effect on the predicted disk heating and ultimately on the allowable cold tip clearances.

Other areas where the LES-CHT framework may be used to contribute to local insights are novel unsteady conjugate based cooling schemes based on pulsating

flows (Zhang et al., 2022), and flows where the fluid domain physics are strongly dependent on the temperature, such as multiphase flows and also combustor flows that include flame-wall interaction. It is of note that many of the LES-CHT papers cited in Chapters 4 and 6 focus on combustion - this thesis has shown that there are flaws in the methodology used in some of these papers, and it could be the case that the new multiscale framework enables improved predictions in these flows by consistently removing the solid domain initial transient, and accurately accounting for the unsteady wall heat storage/release dynamics that can affect the flame behaviour.

8.3 Thesis Key Contributions

- The lack of clarity in the literature on the suitable modelling fidelity for rotating cavity flows is addressed. The need to use LES with CHT to simulate rotating cavities is demonstrated, and the necessity of excercising caution when applying DES to heat transfer in internal flows is shown.
- Most existing state-of-the-art methods for LES-CHT are found to either be fundamentally incapable of calculating accurate wall temperature fluctuations, or inconsistent in dealing with the fluid-solid timescale disparity, leading to errors in the time-average state.
- A new multiscale framework for LES-CHT is presented. It is the only methodology that is able to calculate accurate wall temperature fluctuations caused by all frequencies of fluid domain thermal unsteadiness without contamination from the solid domain initial transient.
- A new kind of heating induced near-disk instability is found for the first time to form in cavities with strongly heated disks. The driving aerothermal physical balancing mechanisms for the inception and development of the new flow structures has been explained, and their wider implications articulated - thus demonstrating the utility of the multiscale framework.

References

Agostinelli, P., Laera, D., Chterev, I., Boxx, I., Gicquel, L., and Poinsot, T. (2022). On the impact of H2-enrichment on flame structure and combustion dynamics of a lean partially-premixed turbulent swirling flame. *Combustion and Flame*, 241:112120.

Agostinelli, P. W., Laera, D., Boxx, I., Gicquel, L., and Poinsot, T. (2021). Impact of wall heat transfer in large eddy simulation of flame dynamics in a swirled combustion chamber. *Combustion and Flame*, 234:111728.

Amirante, D., Adami, P., and Hills, N. J. (2021). A multifidelity aero-thermal design approach for secondary air systems. *Journal of Engineering for Gas Turbines and Power*, 143.

Atkins, N. R. (2013). Investigation of a radial-inflow bleed as a potential for compressor clearance control. *Proceedings of the ASME Turbo Expo*, (GT2013-95768).

Atkins, N. R. and Kanjirakkad, V. (2014). Flow in a rotating cavity with axial throughflow at engine representative conditions. *Proceedings of the ASME Turbo Expo*, (GT2014-27174).

Berger, S., Duchaine, F., and Gicquel, L. Y. (2018). Bluff-body thermal property and initial state effects on a laminar premixed flame anchoring pattern. *Flow, Turbulence and Combustion*, 100:561–591.

Bohn, D., Deuker, E., Emunds, R., and Gorzelitz, V. (1995). Experimental and theoretical investigations of heat transfer in closed gas-filled rotating annuli. *Journal of Turbomachinery*, 117:175–183.

Bohn, D., Deutsch, G. N., Simon, B., and Burkhardt, C. (2000). Flow visualisation in a rotating cavity with axial throughflow. *Proceedings of the ASME Turbo Expo*, (2000-GT-0280).

Bohn, D., Krewinkel, R., and Wolff, A. (2013). Numerical analysis of heat transfer and flow stability in an open rotating cavity using the maximum entropy production principle. *Journal of Turbomachinery*, 135:041023.

Bohn, D. and Ren, J. (2009). How far have we been? Summary of investigations on rotating cavity at IDG, RWTH Aachen University. *Frontiers of Energy and Power Engineering in China*, 3:489–497.

Bohn, D., Ren, J., and Tuemmers, C. (2006). Investigation of the unstable flow structure in a rotating cavity. *Proceedings of the ASME Turbo Expo*, (GT2006-90494).

Campanaro, D. and He, L. (2022). Impact of Wall Temperature on Aerothermal Characteristics of an Array of Surface Microstructures. *Journal of Fluids Engineering*, 145(2). 021203.

Cao, C., Chew, J. W., Millington, P. R., and Hogg, S. I. (2004). Interaction of rim seal and annulus flows in an axial flow turbine. *Journal of Engineering for Gas Turbines and Power*, 126:786–793.

Chew, J. and Hills, N. J. (2007). Computational fluid dynamics for turbomachinery internal air systems. *Philosophical Transactions of the Royal Society A: Mathematical, Physical and Engineering Sciences*, 365:2587–2611.

Childs, P. R. N. (2011). *Rotating Flow: Fundamentals*. Elsevier.

Cho, G., Sangan, C. M., Owen, J. M., and Lock, G. D. (2016). Effect of ingress on turbine disks. *Journal of Engineering for Gas Turbines and Power*, 138.

Choi, H. and Moin, P. (2012). Grid-point requirements for large eddy simulation: Chapman's estimates revisited. *Physics of Fluids*, 24(1):011702.

Davidson, L. (2009). Large eddy simulations: How to evaluate resolution. *International Journal of Heat and Fluid Flow*, 30:1016–1025. The grid can be so coarse that the non-linear processof generating turbulnce cannot be maintained.

Denton, J. D. (1993). The 1993 IGTI scholar lecture: Loss mechanisms in turbomachines. *Journal of Turbomachinery*, 115(4):621–656.

Dorfman, A. (2017). *Applications of Mathematical Heat Transfer and Fluid Flow Models in Engineering and Medicine*. Wiley-ASME Press Series. Wiley.

Dragna, D., Pineau, P., and Blanc-Benon, P. (2015). A generalized recursive convolution method for time-domain propagation in porous media. *The Journal of the Acoustical Society of America*, 138:1030–1042.

Duchaine, F., Corpron, A., Pons, L., Moureau, V., Nicoud, F., and Poinsot, T. (2009). Development and assessment of a coupled strategy for conjugate heat transfer with large eddy simulation: Application to a cooled turbine blade. *International Journal of Heat and Fluid Flow*, 30:1129–1141.

Dweik, Z., Briley, R., Swafford, T., and Hunt, B. (2009). Computational study of the heat transfer of the buoyancy-driven rotating cavity with axial throughflow of cooling air. *Proceedings of the ASME Turbo Expo*, (GT2009-59978).

Errera, M.-P. and Chemin, S. (2013). Optimal solutions of numerical interface conditions in fluid–structure thermal analysis. *Journal of Computational Physics*, 245:431–455.

Errera, M.-P. and Duchaine, F. (2016). Comparative study of coupling coefficients in dirichlet–robin procedure for fluid–structure aerothermal simulations. *Journal of Computational Physics*, 312:218–234.

Fadl, M. and He, L. (2017). On large eddy simulation based conjugate heat transfer procedure for transient natural convection. *Journal of Turbomachinery*, 139.

Farthing, P. R., Long, C. A., Owen, J. M., and Pincombe, J. R. (1992). Rotating cavity with axial throughflow of cooling air: Heat transfer. *Journal of Turbomachinery*, 114:229–236.

Flageul, C., Benhamadouche, S., Lamballais, E., and Laurence, D. (2015). Dns of turbulent channel flow with conjugate heat transfer: Effect of thermal boundary conditions on the second moments and budgets. *International Journal of Heat and Fluid Flow*, 55:34–44.

Fung, K.-Y. and Ju, H. (2001). Broadband time-domain impedance models. *AIAA Journal*, 39.

Ganine, V., Hills, N. J., and Lapworth, B. L. (2013). Nonlinear acceleration of coupled fluid-structure transient thermal problems by anderson mixing. *International Journal for Numerical Methods in Fluids*, 71:939–959.

Gao, F. and Chew, J. W. (2021). Ekman layer scrubbing and shroud heat transfer in centrifugal buoyancy-driven convection. *Journal of Engineering for Gas Turbines and Power*, 143.

Gao, F. and Chew, J. W. (2022). Flow and heat transfer mechanisms in a rotating compressor cavity under centrifugal buoyancy-driven convection. *Journal of Engineering for Gas Turbines and Power*, 144(5). 051010.

Gao, F., Chew, J. W., and Marxen, O. (2020). Inertial waves in turbine rim seal flows. *Physical Review Fluids*, 5:024802.

Giles, M. B. (1997). Stability analysis of numerical interface conditions in fluid-structure thermal analysis. *International Journal for Numerical Methods in Fluids*, 25:421–436.

Gritskevich, M. S., Garbaruk, A. V., Schütze, J., and Menter, F. R. (2012). Development of ddes and iddes formulations for the k-w shear stress transport model. *Flow, Turbulence and Combustion*, 88:431–449.

Gustavsen, B. and Semlyen, A. (1999). Rational approximation of frequency domain responses by vector fitting. *IEEE Transactions on Power Delivery*, 14:1052–1059.

He, L. (1992). Method of simulating unsteady turbomachinery flows with multiple perturbations. *AIAA Journal*, 30:2730–2735.

He, L. (2011). Efficient computational model for nonaxisymmetric flow and heat transfer in rotating cavity. *Journal of Turbomachinery*, 133:021018.

He, L. (2013). Fourier spectral modelling for multi-scale aero-thermal analysis. *International Journal of Computational Fluid Dynamics*, 27:118–129.

He, L. (2019). Closely coupled fluid-solid interface method with moving-average for LES based conjugate heat transfer solution. *International Journal of Heat and Fluid Flow*, 79:108440.

He, L. and Fadl, M. (2017). Multi-scale time integration for transient conjugate heat transfer. *International Journal for Numerical Methods in Fluids*, 83:887–904.

He, L. and Oldfield, M. L. G. (2011). Unsteady conjugate heat transfer modeling. *Journal of Turbomachinery*, 133:031022.

He, L. and Yi, J. (2017). Two-scale methodology for URANS/large eddy simulation solutions of unsteady turbomachinery flows. *Journal of Turbomachinery*, 139:101012.

Hickling, T. and He, L. (2021). Some observations on the computational sensitivity of rotating cavity flows. *Journal of Engineering for Gas Turbines and Power*, 143.

Hickling, T. and He, L. (2023). LES-CHT for a rotating cavity with axial throughflow. *Journal of Turbomachinery*, 145:1–38.

Hösgen, T., Meinke, M., and Schröder, W. (2020). Large-eddy simulations of rim seal flow in a one-stage axial turbine. *Journal of the Global Power and Propulsion Society*, 4:309–321.

Incropera, F., Bergman, T., DeWitt, D., and Lavine, A. (2013). *Fundamentals of Heat and Mass Transfer*. Wiley, 7 edition.

Jaure, S., Duchaine, F., Staffelbach, G., and Gicquel, L. (2013). Massively parallel conjugate heat transfer methods relying on large eddy simulation applied to an aeronautical combustor. *Computational Science and Discovery*, 6:15008.

Karalus, M., Brandt, D., Brown, A., and Lister, V. (2020). A multi-timescale approach for the prediction of temperatures in a gas turbine combustion liner. *Proceedings of the ASME Turbo Expo*, (GT2020-14719).

Kilfoil, A. S. and Chew, J. W. (2009). Modelling of buoyancy-affected flow in co-rotating disc cavities. volume 3, pages 1113–1122. ASME.

Koren, C., Vicquelin, R., and Gicquel, O. (2017a). An acceleration method for numerical studies of conjugate heat transfer with a self-adaptive coupling time step method: Application to a wall-impinging flame. *Proceedings of the ASME Turbo Expo*, (GT2017-64224).

Koren, C., Vicquelin, R., and Gicquel, O. (2017b). Self-adaptive coupling frequency for unsteady coupled conjugate heat transfer simulations. *International Journal of Thermal Sciences*, 118:340–354.

Koren, C., Vicquelin, R., and Gicquel, O. (2018). Multiphysics simulation combining large-eddy simulation, wall heat conduction and radiative energy transfer to predict wall temperature induced by a confined premixed swirling flame. *Flow, Turbulence and Combustion*, 101:77–102.

Kouwa, J., Iso, Y., Polidoro, F., and Gautier, S. (2018). Very-large eddy simulations of disk heat transfer in a rotating cavity using lattice-boltzmann method. *Proceedings of the ASME Turbo Expo*, (GT2018-76832).

Kraus, C., Selle, L., and Poinsot, T. (2018). Coupling heat transfer and large eddy simulation for combustion instability prediction in a swirl burner. *Combustion and Flame*, 191:239–251.

Lee, D., Fahey, D., Skowron, A., et al. (2021). The contribution of global aviation to anthropogenic climate forcing for 2000 to 2018. *Atmospheric Environment*, 244:117834.

Lingwood, R. J. (1997). Absolute instability of the ekman layer and related rotating flows. *Journal of Fluid Mechanics*, 331:405–428.

Long, C. A. (1994). Disk heat transfer in a rotating cavity with an axial throughflow of cooling air. *International Journal of Heat and Fluid Flow*, 15:307–316.

Long, C. A. and Tucker, P. G. (1994a). Numerical computation of laminar flow in a heated rotating cavity with an axial throughflow of air. *International Journal of Numerical Methods for Heat and Fluid Flow*, 4:347–365.

Long, C. A. and Tucker, P. G. (1994b). Shroud heat transfer measurements from a rotating cavity with an axial throughflow of air. *Journal of Turbomachinery*, 116:525.

Maffulli, R. and He, L. (2014). Wall temperature effects on heat transfer coefficient for high-pressure turbines. *Journal of Propulsion and Power*, 30:1080–1090.

Maffulli, R. and He, L. (2017). Impact of wall temperature on heat transfer coefficient and aerodynamics for three-dimensional turbine blade passage. *Journal of Thermal Science and Engineering Applications*, 9.

Margolin, L. G. and Rider, W. J. (2002). A rationale for implicit turbulence modelling. *International Journal for Numerical Methods in Fluids*, 39:821–841.

Mari, R., Cuenot, B., Rocchi, J. P., Selle, L., and Duchaine, F. (2016). Effect of pressure on hydrogen/oxygen coupled flame–wall interaction. *Combustion and Flame*, 168:409–419.

Mathie, R. and Markides, C. N. (2013). Heat transfer augmentation in unsteady conjugate thermal systems – Part I: semi-analytical 1-D framework. *International Journal of Heat and Mass Transfer*, 56:802–818.

Mehdizadeh, O. Z., Vilmin, S., Tartinville, B., and Hirsch, C. (2017). Nonlinear harmonic method applied to turbine conjugate heat transfer analysis for efficient simulation of hot streak clocking and unsteady heat transfer. *Proceedings of the ASME Turbo Expo*, (GT2017-63622).

Menter, F. (1994). Two-equation eddy-viscosity turbulence models for engineering applications. *AIAA Journal*, 32:1598–1605.

Menter, F. (2018). Stress-blended eddy simulation (SBES) — a new paradigm in hybrid RANS-LES modeling. *Notes on Numerical Fluid Mechanics and Multidisciplinary Design*, 137:27–37.

Moffat, R. J. (1998). What's new in convective heat transfer? *International Journal of Heat and Fluid Flow*, 19(2):90–101.

Nicoud, F. and Ducros, F. (1999). Subgrid-scale stress modelling based on the square of the velocity gradient tensor. *Flow, Turbulence and Combustion*, 62:183–200.

Oh, T.-K., Tafti, D. K., and Krishnamurthy, N. (2021). Fully coupled large eddy simulation-conjugate heat transfer analysis of a ribbed cooling passage using the immersed boundary method. *Journal of Turbomachinery*, 143:1–38.

O'Mahoney, T. and Chew, J. (2012). Sensitivity of LES results from turbine rim seals to changes in grid resolution and sector size. *Progress in Aerospace Sciences*, 52:48–55.

Onori, M., Amirante, D., Hills, N. J., and Chew, J. W. (2016). LES validation for a rotating cylindrical cavity with radial inflow. *Proceedings of the ASME Turbo Expo*, pages GT2016–56393.

Onori, M., Amirante, D., Hills, N. J., and Chew, J. W. (2019). Heat transfer prediction from large eddy simulation of a rotating cavity with radial inflow. *Journal of Engineering for Gas Turbines and Power*, 141:121002.

Owen, J. M. (2010). Thermodynamic analysis of buoyancy-induced flow in rotating cavities. *Journal of Turbomachinery*, 132:031006.

Owen, J. M., Abrahamsson, H., and Lindblad, K. (2007). Buoyancy-induced flow in open rotating cavities. *Journal of Engineering for Gas Turbines and Power*, 129:893–900.

Owen, J. M. and Long, C. A. (2015). Review of buoyancy-induced flow in rotating cavities. *Journal of Turbomachinery*, 137:111001.

Owen, J. M. and Pincombe, J. R. (1980). Velocity measurements inside a rotating cylindrical cavity with a radial outflow of fluid. *Journal of Fluid Mechanics*, 99:111–127.

Owen, J. M. and Powell, J. (2006). Buoyancy-induced flow in a heated rotating cavity. *Journal of Engineering for Gas Turbines and Power*, 128:128–134.

Owen, J. M. and Tang, H. (2015). Theoretical model of buoyancy-induced flow in rotating cavities. *Journal of Turbomachinery*, 137:111005.

Özgen, S. (2004). Effect of heat transfer on stability and transition characteristics of boundary-layers. *International Journal of Heat and Mass Transfer*, 47:4697–4712.

Palkin, E., Mullyadzhanov, R., Hadziabdic, M., and Hanjalic, K. (2016). Scrutinizing URANS in shedding flows: The case of cylinder in cross-flow in the subcritical regime. *Flow, Turbulence and Combustion*, 97:1017–1046.

Pitz, D. B., Chew, J., and Marxen, O. (2019a). Large-eddy simulation of buoyancy-induced flow in a sealed rotating cavity. *Journal of Engineering for Gas Turbines and Power*, 141:021020.

Pitz, D. B., Chew, J. W., and Marxen, O. (2019b). Effect of an axial throughflow on buoyancy-induced flow in a rotating cavity. *International Journal of Heat and Fluid Flow*, 80.

Pogorelov, A., Meinke, M., and Schröder, W. (2019). Large-eddy simulation of the unsteady full 3D rim seal flow in a one-stage axial-flow turbine. *Flow, Turbulence and Combustion*, 102:189–220.

Pope, S. B. (2004). Ten questions concerning the large-eddy simulation of turbulent flows. *New Journal of Physics*, 6:35.

Puttock-Brown, M. R. and Rose, M. G. (2018). Formation and evolution of Rayleigh-Bénard streaks in rotating cavities. *Proceedings of the ASME Turbo Expo*, (GT2018-75497).

Puttock-Brown, M. R., Rose, M. G., and Long, C. A. (2017). Experimental and computational investigation of Rayleigh-Bénard flow in the rotating cavities of a core compressor. *Proceedings of the ASME Turbo Expo*, (GT2017-64884).

Reynolds, W. C. and Hussain, A. K. (1972). The mechanics of an organized wave in turbulent shear flow. Part 3. Theoretical models and comparisons with experiments. *Journal of Fluid Mechanics*, 54:263–288.

Sagaut, P. (2006). *Large Eddy Simulation for Incompressible Flows*. Springer-Verlag.

Saini, D. and Sandberg, R. D. (2021). Large-eddy simulations of high Rossby number flow in the high-pressure compressor inter-disk cavity. *Journal of Turbomachinery*, 143.

Sangan, C. M., Pountney, O. J., Zhou, K., Owen, J. M., Wilson, M., and Lock, G. D. (2012). Experimental measurements of ingestion through turbine rim seals - Part II: Rotationally induced ingress. *Journal of Turbomachinery*, 135.

Schäfer, P., Severin, J., and Herwig, H. (1995). The effect of heat transfer on the stability of laminar boundary layers. *International Journal of Heat and Mass Transfer*, 38:1855–1863.

Scholl, S., Verstraete, T., Duchaine, F., and Gicquel, L. (2016). Conjugate heat transfer of a rib-roughened internal turbine blade cooling channel using large eddy simulation. *International Journal of Heat and Fluid Flow*, 61:650–664.

Schultz, D. L. and Jones, T. V. (1973). Heat-transfer measurements in short-duration hypersonic facilities. *AGARD*, AG165.

Shahi, M., Kok, J. B., Casado, J. C. R., and Pozarlik, A. K. (2015). Transient heat transfer between a turbulent lean partially premixed flame in limit cycle oscillation and the walls of a can type combustor. *Applied Thermal Engineering*, 81:128–139.

Shur, M., Strelets, M., Travin, A., Suzuki, T., and Spalart, P. (2021). Unsteady simulations of sound propagation in turbulent flow inside a lined duct. *AIAA Journal*, pages 1–17.

Slotnick, J., Khodadoust, A., Alonso, J., Darmofal, D., Gropp, W., Lurie, E., and Mavriplis, D. (2014). CFD Vision 2030 study: A path to revolutionary computational aerosciences.

Soares, C. (2008). *Gas turbines : a handbook of air, land, and sea applications*. Butterworth-Heinemann.

Sun, Z., Amirante, D., Chew, J., and Hills, N. J. (2015). Coupled aerothermal modeling of a rotating cavity with radial inflow. *Journal of Engineering for Gas Turbines and Power*, 138:032505.

Sun, Z., Chew, J. W., Hills, N. J., Volkov, K. N., and Barnes, C. J. (2010). Efficient finite element analysis/computational fluid dynamics thermal coupling for engineering applications. *Journal of Turbomachinery*, 132.

Sun, Z., Gao, F., Chew, J. W., and Amirante, D. (2022). LES investigation of low Rossby number buoyant flow in rotating cavities. *Journal of Engineering for Gas Turbines and Power*.

Sun, Z., Lindblad, K., Chew, J., and Young, C. (2007). LES and RANS investigations into buoyancy-affected convection in a rotating cavity with a central axial throughflow. *Journal of Engineering for Gas Turbines and Power*, 129:318–325.

Tan, Q., Ren, J., and Jiang, H. (2009). Prediction of flow features in rotating cavities with axial throughflow by rans and les. *Proceedings of the ASME Turbo Expo*, (GT2009-59428).

Tan, Q., Ren, J., and Jiang, H. (2014). Prediction of 3D unsteady flow and heat transfer in rotating cavity by discontinuous Galerkin method and transition model. *Proceedings of the ASME Turbo Expo*, (GT2014-26584).

Tang, H. and Owen, J. M. (2017). Effect of buoyancy-induced rotating flow on temperatures of compressor disks. *Journal of Engineering for Gas Turbines and Power*, 139:062506.

Tang, H. and Owen, J. M. (2021). Effect of radiation on heat transfer inside aeroengine compressor rotors. *Journal of Turbomachinery*, 143.

Tang, H. and Owen, J. M. (2022). Plume Model for Buoyancy-Induced Flow and Heat Transfer in Closed Rotating Cavities. *Journal of Turbomachinery*, 145(1). 011005.

Tang, H., Shardlow, T., and Owen, J. M. (2015). Use of fin equation to calculate nusselt numbers for rotating disks. *Journal of Turbomachinery*, 137.

Tateishi, A., Watanabe, T., and Himeno, T. (2018). Unsteady flow simulation of buoyancy-driven flows in high-pressure compressor disk cavities. *Proceedings of the ASME Turbo Expo*, (GT2018-76327).

Tian, S. and Zhu, Y. (2012). Disk heat transfer analysis in a heated rotating cavity with an axial throughflow. *Proceedings of the ASME Turbo Expo*, (GT2012-69185).

Timperi, A. (2014). Conjugate heat transfer LES of thermal mixing in a T-junction. *Nuclear Engineering and Design*, 273:483–496.

Tucker, P. G. (2011). Computation of unsteady turbomachinery flows: Part 2-LES and hybrids. *Progress in Aerospace Sciences*, 47:546–569.

Tucker, P. G. (2013). Trends in turbomachinery turbulence treatments. *Progress in Aerospace Sciences*, 63:1–32.

Tucker, P. G. (2016). *Advanced Computational Fluid and Aerodynamics*. Cambridge Aerospace Series. Cambridge University Press.

Tyacke, J. and Tucker, P. G. (2015). Future use of large eddy simulation in aero-engines. *Journal of Turbomachinery*, 137:081005.

Tyacke, J., Vadlamani, N. R., Trojak, W., Watson, R., Ma, Y., and Tucker, P. G. (2019). Turbomachinery simulation challenges and the future. *Progress in Aerospace Sciences*, 110:100554.

Van Doormaal, J. P. and Raithby, G. D. (1984). Enhancements of the simple method for predicting incompressible fluid flows. *Numerical Heat Transfer*, 7(2):147–163.

Voigt, S., Noll, B., and Aigner, M. (2019). Development of a model for unsteady conjugate heat transfer simulations. *Progress in Computational Fluid Dynamics*, 19:69–79.

Yao, M. and He, L. (2020). Implicit discontinuous Galerkin solution on unstructured mesh for turbine blade secondary flow. *Journal of Turbomachinery*, 142.

Zhang, Z., Li, Q., Bruecker, C., and Zhang, Q. (2022). Enhanced thermal performance with high-amplitude intermittent impingement cooling. *International Journal of Heat and Mass Transfer*, 185:122359.

Zhong, B. and Tucker, P. G. (2004). k-l based hybrid LES/RANS approach and its application to heat transfer simulation. *International Journal for Numerical Methods in Fluids*, 46:983–1005.

Appendix A

Material Properties

Table A.1. Solid domain material properties used in this thesis.

Material	ρ **[**kg/m3**]**	$\boldsymbol{c}$ **[**J/kgK**]**	$\boldsymbol{k}$ **[**W/mK**]**
Nickel	8000	450	80.0
Titanium (Ti-6Al-4V)	4500	570	7.3
Epoxy	1200	1000	0.2